Boron in Palladium: Interaction, Phase Formation and Phase Transformation

Von der Fakultät für Chemie der Universität Stuttgart
zur Erlangung der Würde eines Doktors der Naturwissenschaften (Dr. rer. nat.)
genehmigte Abhandlung

vorgelegt von

MARKUS BECK

aus Reutlingen

Hauptberichter: Prof. Dr. Ir. E. J. Mittemeijer
Mitberichter: Prof. Dr. M. Rühle
Tag der mündlichen Prüfung: 19.09.2001

INSTITUT FÜR METALLKUNDE DER UNIVERSITÄT STUTTGART
MAX-PLANCK-INSTITUT FÜR METALLFORSCHUNG STUTTGART
2001

Table of Contents

Introduction **VIII**

1. The formation of interstitial solid solutions based on solvents showing the fcc structure; elastic versus chemical interaction **1**

1.1. Introduction; criteria for formation of interstitial solid solutions 3
1.2. Experimental 4
1.3. Results 6
1.4. Discussion 12
1.5. Conclusions 17

2. The structure of the palladium-rich boride Pd_5B ($Pd_{16}B_3$) **19**

2.1. Introduction 21
2.2. Experimental 21
2.3. Results 22
2.4. Discussion 24
2.5. Conclusions 26

3. Powder diffraction data for borides Pd_3B and Pd_5B_2 and the formation of an amorphous boride Pd_2B **27**

3.1. Introduction 29
3.2. Experimental 29
3.3. Results 30
3.4. Discussion 35

4. Decomposition of the interstitial solid solution Pd(B) 37
4.1. Introduction . . . 39
4.2. Model for calculation of the X-ray diffraction-line profiles . . . 39
4.3. Experimental . . . 42
4.4. Observations . . . 44
4.5. Fitting of X-ray diffraction-line profiles . . . 45
4.6. Phase composition and amount . . . 48
4.7. Microstrain . . . 50
4.8. Conclusions . . . 52

5. Simultaneous determination of specimen temperature and specimen displacement in high temperature X-ray diffractometry applying Bragg-Brentano geometry 53
5.1. Introduction . . . 55
5.2. The principle of the method . . . 56
5.3. Application of the method . . . 57
5.4. Conclusions . . . 63

6. Kurzfassung der Dissertation in deutscher Sprache 65
6.1. Einleitung . . . 67
6.2. Experimentelles . . . 68
6.3. Bildung von intersititellen Mischkristallen auf Basis von kfz Übergangsmetallen; elastische und chemische Wechselwirkung . . . 69
6.4. Die Struktur des palladiumreichen Borids Pd_5B ($Pd_{16}B_3$) . . . 72
6.5. Röntgenbeugungsdaten der Boride Pd_3B und Pd_5B_2 und die Bildung des amorphen Borids Pd_2B . . . 75
6.6. Zerfall des interstitiellen Mischkristalles Pd(B) . . . 76
6.7. Eine neue Methode zur simultanen Bestimmung von Probenhöhenfehler und Probentemperatur bei der Hochtemperaturdiffraktometrie unter Verwendung der Bragg-Brentano-Geometrie . . . 81

A. Phasediagrams of the Pd-B system 85

References 89

Cirriculum Vitae 97

Introduction

There has been outstanding progress in the development and understanding of interstitial alloys during the twentieth century. Interstitial alloys, especially those between transition metals and the small atoms of carbon, nitrogen, boron, oxygen and hydrogen, either taken singly or together, constitute a significant section of the field of metallurgy. Many of these advances took place empirically or in specific technological contexts.

Interstitial solid solutions based on the transition metals are the most common important materials with attractive mechanical properties. Knowledge on crystallography of phases that can occur and phase transformations is a prerequisite to arrive at optimal properties at low and high temperatures to use this materials at optimal conditions.

One of the earliest works that dealt with criteria of formation of interstitial solid solutions are the works of Hägg [1, 2]. These investigations suggest a (”Hägg’s”) critical atomic radius ratio involving an interstitial solid solution based on a transition metal and a metalloid (like B, C, N and O) is formed only, if the atomic radius ratio of the two components r_i/r_m is less then 0.59.

Another criterion of formation of extensive interstitial solid solution is given by King [3]. He suggested that the formation only occurs if a so-called volume size factor Ωsf (cf. chapter 1.1) will not exceed a given value ($\Omega sf < 30 \times 10^6$). The solubility of boron in transition metals is suggested to be small [4]. This suggestion is caused by the large stability of the *p*-orbitals of boron as well as the large atomic radius, which restrict the solubility.

All these criteria are based on geometrical relationships of the solvent (transition metal) and the solute (metalloid). Following the geometrical restrictions of these rules the only element isotypical with Cu would be Pb which satisfy Hägg’s criterion; just this heavy metal does not form any solid solution with interstitial elements. The principles are not satisfied for the solute boron and carbon and the late transition metal (A^9 elements: Co, Rh, Ir and A^{10} elements: Ni,

Pd, Pt) as solvent. All these metal possess the *fcc* structure.

In the first part of this work (chapter 1) the nature of the solid solution of these late transition metals with boron and partly with carbon is clarified (interstitial *vs.* substitutional). It is shown that in contrast to the old and new rules (see above) boron forms interstitial solid solutions with Co, Rh, Ir, Ni, Pd and Pt and carbon with Pd.

The Pd-B system plays an extraordinary role. It posses the largest solubility of boron of all transition metals. Furthermore, the solid solution is a high temperature phase, which can be retained at room temperature by quenching. Using accurate unit cell parameter measurements and density measurements the number of atoms and the volume of the unit cell is determined precisely (cf. chapter 1). As a result of this, it is shown that the hard spheres model characterizing the ideal solid solution, is inconsistent with the observed volume-interstitial content relationship for the solid solution Pd(B), where a significant, negative deviation (volume contraction) from the hard sphere model prediction occurs. Furthermore, it is shown that the solubility of the interstitial elements (H, B, C and N) is qualitatively inversely proportional with the potential valency. Additionally, the chemical (electronical) interaction appears to govern the interstitial solid solution formation rather than the elastic interaction as characterized by the geometrical criteria (see above).

The palladium rich part of the binary system Pd-B is discussed controversially in literature [5–9]. The phase diagram Pd-B as proposed by Rogl [9] shows the *fcc* solid solution Pd(B) with a large range of homogeneity up to the mole fraction x_B = 0.18 [10], the low-temperature borides $Pd_{\sim 6}B$, $Pd_{\sim 5}B$ and the high-temperature boride $Pd_{\sim 4}B$. The structures of these borides are unknown, whereas the structures of the borides Pd_3B (*oP*16, *Pnma*, Fe_3C type [11]), Pd_5B_2 (*mC*28, $C2/c$, Mn_5C_2 type [11]) and Pd_2B (*oP*6, *Pnnm*, anti-FeS_2 type [12]) have been determined.

In contrast to the phase diagram suggested by Rogl [9], the palladium rich part of the phase diagram Pd-B ($0 < x_B < 0.18$) as proposed by Alqasmi *et al.* [7] on the basis of X-ray diffraction analysis shows at temperatures below 670 K only one boride - $Pd_{16}B_3$ (= γ phase) - which has been reported to be a superstructure of the Cu type structure.

To clarify this, structural investigations are subject of chapter 2 and 3. The structure of the low temperature phase Pd_5B ($Pd_{16}B_3$) is clarified, which represents the palladium-richest boride of this binary system. It forms congruently from the cubic solid solution Pd(B) (high temperature phase) upon heating below 658 K. Pd_5B shows a tetragonal distortion of the solid solution unit cell, where B occupies the distorted octahedral interstices formed by the Pd sublattice in a random way (the crystal structure data are given in chapter 2). This is in contrast with the pendant structure in the Pd-H system, $PdH_{1.33}$, that is characterized by vacancies on the Pd sublattice.

Powder diffraction data and exact accurate cell parameter of the palladium-rich phases Pd_3B

and Pd_5B_2 were missing in literature of this complex palladium-rich portion of this binary system Pd-B. The data are determined using X-ray analysis (cf. chapter 3). The literature data (single crystal data) are confirmed applying the Rietveld method. Further an amorphous alloy Pd_2B is observed. The position of the principal scattering peak of Pd_2B fulfils the Nagel-Tauc criterion. This criterion describes a model of metallic glass formation based on nearly-free-electron approximation.

A miscibility gap in the binary system Pd-B exists in the range of $0.02 < x_B < 0.10$ between 585 K and 683 K [5–9]. This decomposition of the Pd(B) solid solution is analyzed by use of X-ray diffraction in chapter 4. A structure model is used to simulate the X-ray diffraction-line profiles. The decomposition can be described as the precipitation of a boron-poor *fcc* phase in the parent *fcc* phase gradually enriching in boron. The experimentally determined width of the miscibility gap is different from the previous experimental results [13], but agrees with theoretical data obtained on the basis of the quasi-chemical approximation [13]. Furthermore, the microstrain in the decomposed state is investigated by use of the Williamson-Hall analysis [14] and is compared with the microstrain of the initial, quenched supersaturated solid solution.

A very useful for investigation of the behaviour of (crystalline) materials at non-ambient temperatures is *in situ* high temperature X-ray powder diffraction. To arrive at correct values of the unit cell parameters, the positions of the Bragg reflections, characterized by the corresponding diffraction angles have to be determined accurately. High temperature X-ray diffractometry is coupled with inaccuracies in temperature and changing specimen alignment during the measurement on the diffractometer. In chapter 5 a new method is presented which enables the simultaneous determination of the specimen temperature and misalignment to achieve exact values of the X-ray experiment at elevated temperatures. An experimental example applying the method to a specific material is given, which shows that the method provides correct data from *in situ* high temperature X-ray powder diffraction measurements.

Chapter 1

The formation of interstitial solid solutions based on solvents showing the fcc structure; elastic versus chemical interaction

M. Beck, M. Ellner and E.J. Mittemeijer

Abstract: Unit cell parameters and densities were measured for the terminal solid solutions of the late transition metals showing the *fcc* structure (α-Co, Rh, Ir, Ni, Pd, Pt) with boron and partly with carbon. Especially the solid solutions Pd(B) and Pd(C) were investigated because of the large homogeneity range up to the atomic fractions $x_B = 0.186$ and $x_C \simeq 0.05$, respectively. The unit cell parameter increases and the density decreases with increasing boron and carbon content. Comparison of the calculated and measured number of atoms in the Pd(B) and Pd(C) unit cells confirms the interstitial nature of both solid solutions. The difference between the measured dependence of the Pd-B shortest interatomic distances on the solute content and those calculated according the hard sphere model indicates a distinct negative deviation from additivity of the pure form volumes. The chemical (electronic) interaction plays a more important role than the elastic interaction (characterized by a size factor) in the formation of solid solutions of metals with the interstitially dissolved metalloids H, B, C, N and O.

1.1. Introduction; criteria for formation of interstitial solid solutions

The structure of interstitial solid solutions has been subject of research since at least about 1930 [1–3]. The first two investigations [1, 2] suggest a ("Hägg's") critical atomic radius ratio involving that an interstitial solid solution based on a transition metal and a metalloid (like B, C, N and O) is formed only if the atomic radius ratio r_i/r_m is less then 0.59 (r_i = atomic radius of the solute (interstitial element); r_m = atomic radius of the solvent). This criterion for the ratio r_i/r_m is not satisfied for boron and carbon as solute and the A^9- (Co, Rh, Ir) and A^{10}-elements (Ni, Pd, Pt) as solvent; see Table 1.1. All these metals (solvents) possess the Cu (*fcc*) structure (Pearson code $cF4$, space group $Fm\bar{3}m$). Originally, in Refs. [1] and [2], for the calculation of the atomic radii ratio Goldschmidt's atomic radius data were used [15, 16].

Table 1.1.: Atomic radius ratio r_i/r_m, where r_i is the atomic radius of the interstitial solute (hydrogen, boron, carbon and nitrogen) and r_m is the atomic radius of the solvent (late transition metal). Values for r_i/r_m were calculated using the atomic radii reported in [17]. The atomic radii of of hydrogen, boron, carbon and nitrogen are $r_H = 0.0779$ nm, $r_B = 0.0920$ nm, $r_C = 0.0876$ nm and $r_N = 0.0825$ nm [17].

	Co	Rh	Ir	Ni	Pd	Pt
r_m (nm)	0.1252	0.1345	0.1357	0.1246	0.1376	0.1387
r_H/r_m	0.622	0.579	0.574	0.625	0.566	0.562
r_B/r_m	0.735	0.684	0.678	0.738	0.669	0.663
r_C/r_m	0.700	0.651	0.646	0.703	0.637	0.632
r_N/r_m	0.659	0.613	0.608	0.662	0.600	0.595

Comparing the atomic radii as given for the coordination number 12 (corresponding to the *fcc* structure) in Refs. [15–18], it follows that small differences occur for atomic radii of the late transition metals (< 1 %). On the other hand relatively large differences occur for the atomic radii of the metalloids boron and carbon: 0.0920 nm [17] $< r_B <$ 0.098 nm [18] and 0.071 nm [16] $< r_C <$ 0.0914 nm [18], respectively. These differences are due to different methods used for the determination of atomic radii. A value for the atomic radius of boron has been derived in Ref. [15] from unit cell parameter data of the boride Fe_2B ($r_B = 0.097$ nm). In Ref. [18] the values for the atomic radii of boron and carbon were deduced from unit cell parameter data for hexaborides and carbon boride ($r_B = 0.098$ nm; $r_C = 0.0914$ nm). Further, values for the atomic radii of B and C were calculated from allotropic modifications of the pure elements as well as from the B-B and C-C distances in some compounds of simple

structure ($r_B = 0.0920$ nm; $r_C = 0.0876$ nm) [17]. In any case, whichever of these values is used, following Hägg's rule no A^9 and A^{10} element should form an interstitial solid solution with boron.

Another criterion for the formation of extensive interstitial solid solutions was given in Ref. [3]: it was suggested that formation of extensive interstitial solid solutions only occurs if the volume size factor* for the solid solution, Ωsf, is less then $30 \cdot 10^6$.

A small solubility of boron in transition metals has also been suggested in Ref. [4]. This should be caused by the large stability of the *p*-orbitals of boron as well as the large atomic radius of boron which restrict the interstitial solubility.

These criteria discussed above imply that geometrical factors would govern the stability of the interstitial solid solution.

With regard to the above criteria the Pd-B system plays an extraordinary role among the systems investigated here: the criteria mentioned make dissolution of B as interstitial the least likely (as compared to C, N; for Hägg's criterion, see Table 1.1; for the volume size factor, see section 1.4). Yet, boron can be dissolved in palladium up to the atomic fraction $x_B = 0.186$ [10, 22], which is by far the largest solubility of boron known in the transition metals. The solid solution Pd(B) is a high-temperature phase, which can be retained at room temperature by quenching. At temperatures below 683 K a miscibility gap exists over the composition range $0.021 < x_B < 0.102$ and, moreover, a palladium-rich boride $Pd_{16}B_3$ ($0.152 < x_B < 0.165$) was reported for temperatures below 670 K [7].

1.2. Experimental

The alloys investigated (cf. Tables 1.3 - 1.6) were prepared from the elements by arc melting under argon (550 hPa, 99.999 %; Messer Griesheim; for purity of the materials used, see Table 1.2). The weight of the samples was measured before and after alloying; no significant differences were observed. The homogeneity of the bulk alloys was checked by means of X-ray diffraction and by metallographic analysis. The boron containing alloys with A^9 elements and nickel as solvent show a small solubility of boron (Table 1.2). Consequently the corresponding alloys are not single phase: they are composed of two phases. In these cases, determination of the amount of dissolved solute in either phase was not possible by chemical analysis. In case of binary systems with large solubility for the terminal solid solution (Pd(B), Pd(C), Pt(B)) the alloys are single phase. The boron and carbon contents of these solid solutions were determi-

*The volume size factor is defined by $\Omega sf = \frac{1}{V_a}(\frac{\partial V_c}{\partial x_i})$, where V_a denotes the atomic volume of the solvent and $\frac{\partial V_c}{\partial x_i}$ is the initial slope of the volume-atomic fraction plot with V_c as the unit cell volume and x_i as the atomic fraction solute.

Table 1.2.: Purity of the metal solvents; the purity of boron and the carbon fibers used was 99.5 wt. % (Ventron). Temperature and time of annealing of the filings.

	Co(B)	Rh(B)	Ir(B)	Ni(B)	Pd(B)	Pt(B)	Pd(C)
Purity (wt. %)	99.9	99.9	99.9	99.98	99.9	99.9	99.9
supplier	Johnson Matthey	Heraeus	Heraeus	Goodfellow	Heraeus	Heraeus	Heraeus
Annealing temperature (K)	1073	1073	1273	1273	1323	873	1073
Annealing time (s)	30	30	60	120	300	120	30
Maximum solubility (at. %) at T (K)	≈ 0.2 1273 [19]	very small this work	very small 1473 [20]	≈ 0.3 1358 [21]	19.5 1411 [7]	3.6 1200 [22]	≥ 4.67 as cast alloy this work

nated using inductive coupled plasma optical emission spectrometry for boron and by burning the sample with additional Fe and W in an oxygen flow and infrared absorption measurements of CO_2 as burning product for carbon.

The bulk alloys were filed for the unit cell parameter measurements by means of X-ray diffraction analysis. The filings were put in quartz capsules, which were flushed with argon, then evacuated and annealed to remove internal stress, and subsequently water quenched to avoid decomposition phenomena. Before annealing of the Pd(C) alloys the pressure of argon in the quartz capsule was 500 hPa. The temperatures and times of annealing have also been specified in Table 1.2.

Powder diffraction patterns were recorded at room temperature in a Guinier transmission camera (Enraf-Nonius FR552) using Mo$K\alpha_1$ radiation (λ = 0.070930 nm). Germanium (99.9999 wt. %; Johnson Matthey, unit cell parameter a = 0.56574 nm [23]) was used as an internal standard. Single coated CEA Reflex 15 film was used for the Guinier patterns. The positions of the diffraction lines in the Guinier patterns were determinated using a Line-Scanner LS 20 (KEJ Instruments). Unit cell parameters were refined by least squares fitting of Bragg's equation to the positions of the diffraction lines in the range $12^\circ < 2\theta < 56^\circ$ (2θ = diffraction angle). In the case of the two-phase samples (see above), only the diffraction lines of the solid solution were analysed.

The density of the as cast bulk alloys of Pd(B) and Pd(C) was measured by means of the buoyancy method with CCl_4 as standard liquid at 289 K.

1.3. Results

1.3.1. Binary systems with small solubility of boron

The unit cell parameter, a, of the boron-containing solid solution of the A^9-elements (α-Co, Rh, Ir) and Ni is generally larger than that of the pure metal (Table 1.3). The change of the unit cell parameter of the Pt(B) solid solution (one-phase alloy) as function of the atomic ratio, x_B^r ($= x_B/(1-x_B) = x_B/x_{Pt}$: atomic ratio = number of solute atoms *per* solvent atom), is shown in Fig. 1.1 (see also Table 1.4).

A marked increase of the Pt(B) unit cell parameter with boron content is observable, which contradicts earlier work where a reverse trend was reported [22].

1.3.2. Solid solutions of palladium with boron or carbon

The results of the unit cell parameter and density measurements for the solid solutions Pd(B) and Pd(C) are shown in Figs. 1.2 and 1.3 (see also Tables 1.6 and 1.5).

Table 1.3.: Unit cell parameters of the late transition metals and of the corresponding solid solutions with boron at maximum solubility as indicated in Table 1.2 (two phase alloys; cf. section 1.2).

	Co	Co(B)	Rh	Rh(B)	Ir	Ir(B)	Ni	Ni(B)
Atomic fraction, x_B		< 0.02		< 0.02		< 0.02		< 0.01
Unit cell parameter (nm)	0.35444(2)	0.35452(1)	0.38025(2)	0.38043(2)	0.38389(3)	0.38402(1)	0.35256(3)	0.35311(1)

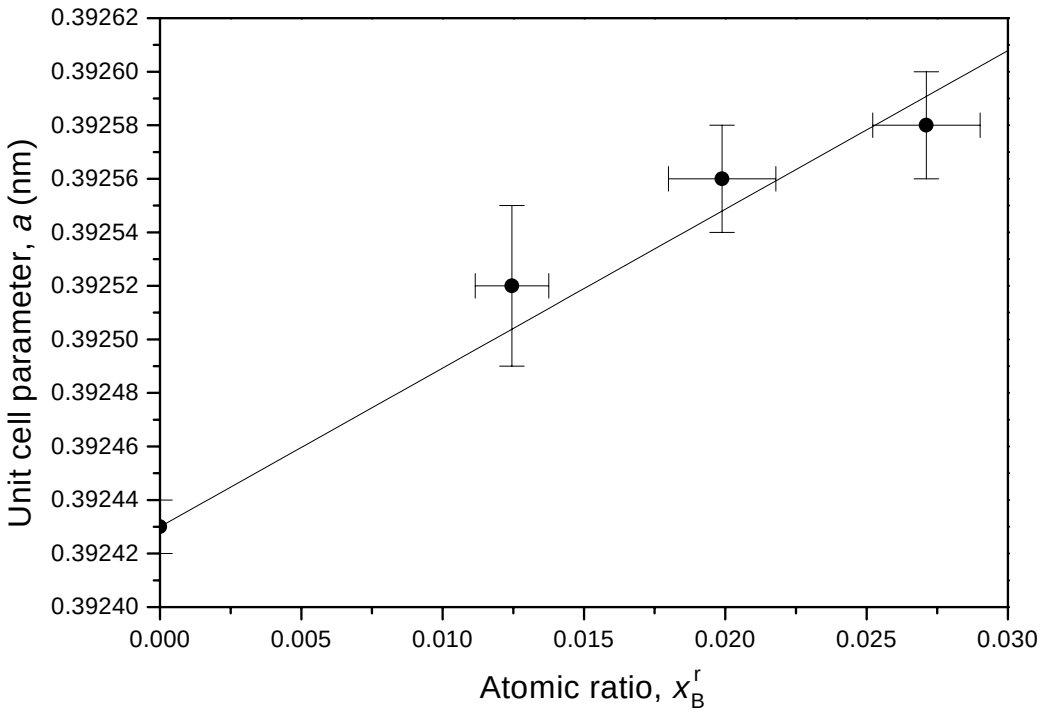

Figure 1.1.: Unit cell parameter, *a*, of the solid solution Pt(B) as function of the atomic ratio, x_B^r; error ranges have been indicated as well.

Table 1.4.: Unit cell parameter, *a*, for various compositions of the solid solution Pt(B).

Atomic fraction, x_B	Atomic ratio, x_B^r	Unit cell parameter, *a* (nm)
0	0	0.39243(1)
0.0123(13)	0.0125(13)	0.39252(3)
0.0195(18)	0.0199(19)	0.39256(2)
0.0264(18)	0.0271(19)	0.39258(2)

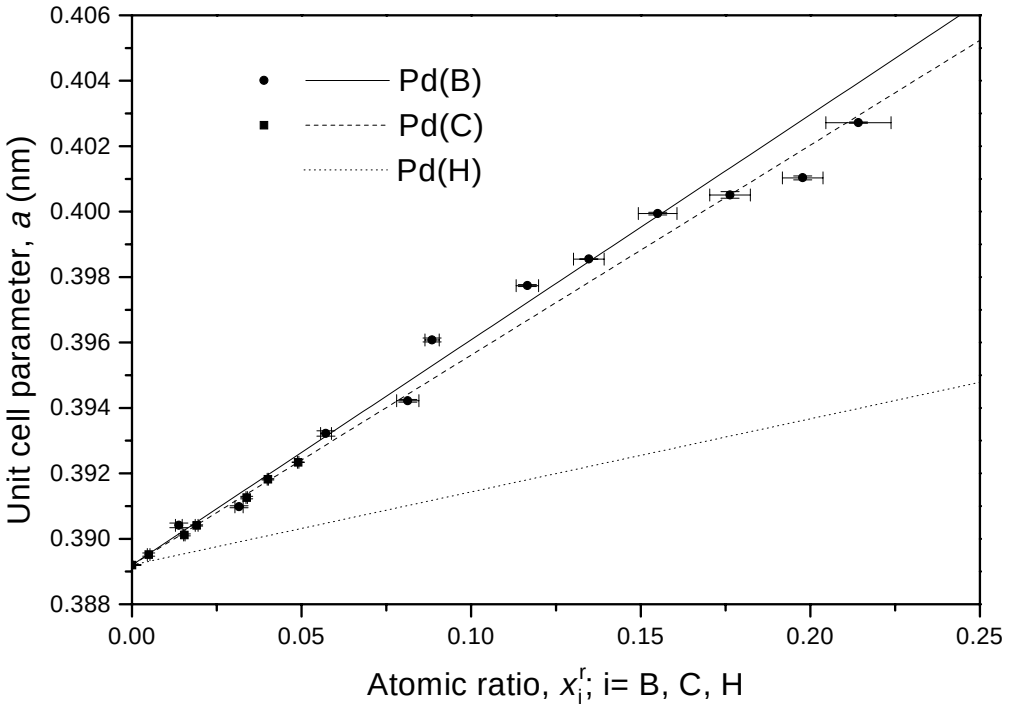

Figure 1.2.: Unit cell parameter, *a*, of the solid solutions Pd(B) (•) and Pd(C) (■) as function of the atomic ratio, x_i^r (i = B, C); error ranges have been indicated as well. The straight lines (dashed: Pd(C), full: Pd(B)) have been fitted (least squares analysis) to the experimental data. The dependence of the unit cell parameter on the atomic ratio, x_H^r, of the solid solution Pd(H) has also been indicated (dotted line) [24].

Metallographic investigation indicated that the as-cast palladium based alloy with the highest carbon content, $x_C = 0.047$, is a single phase. This implies that a higher solubility of carbon in palladium has been found in this work than in Ref. [25] where the maximum solubility value was $x_C = 0.029$ at 1473 K.

The occurrence of a linear dependence of the unit cell parameter on the solute atomic fraction, here x_B and x_C, or on the atomic ratio, here x_B^r and x_C^r (see above), for substitutional and interstitial solid solutions, respectively, has been discussed elsewhere [26]. For small solute solubilities experimentally significant differences do not occur between these two correlations. For interstitial solid solutions the relationship between the unit cell parameter and the atomic fraction is more usual than the one between the unit cell parameters and the atomic ratio, whereas the second one represents the more fundamental relationship [26]. Therefore the dependence of the unit cell parameter on the content of interstitial atoms will be presented in both ways.

The *increase* of the unit cell parameter with interstitial element content is larger for Pd(B)

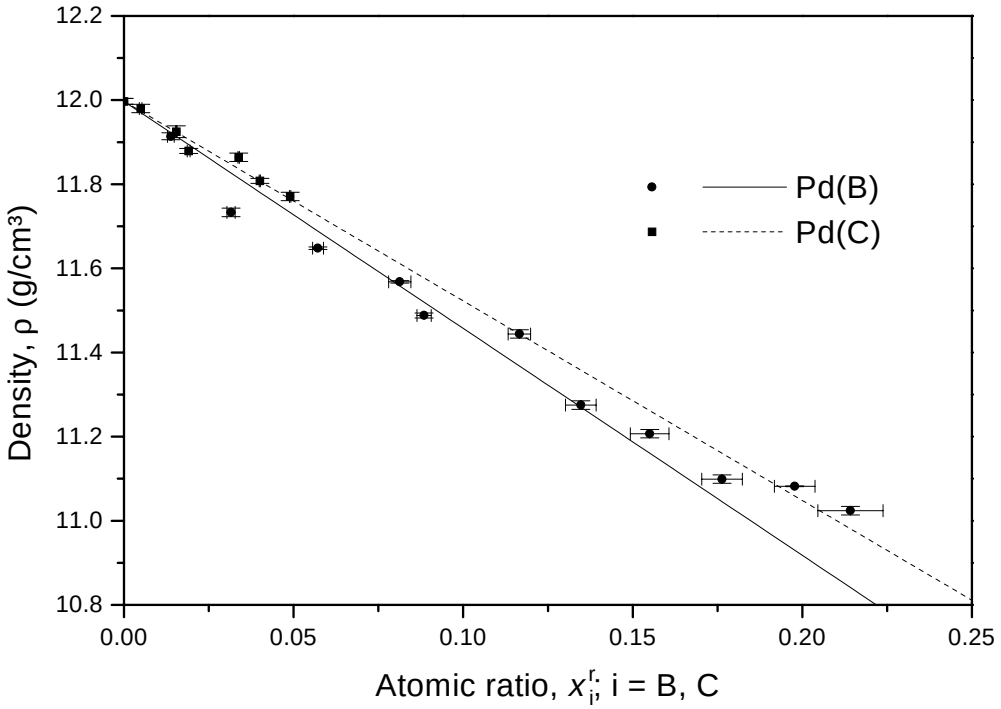

Figure 1.3.: Density, ρ, of the solid solutions Pd(B) (•) and Pd(C) (■) as function of the atomic ratio, x_i^r; error ranges have been indicated as well. The straight lines (dashed: Pd(C), full: Pd(B)) have been fitted (least squares analysis) to the experimental data.

Table 1.5.: Unit cell parameter, *a*, density, ρ, and number of atoms in the unit cell, *n*, for various compositions of Pd(C).

Atomic fraction, x_C	Atomic ratio, x_C^r	Unit cell parameter, *a* (nm)	Density, ρ (g/cm^3)	Numbers of atoms in the unit cell, *n*
0	0	0.38920(1)	11.997(7)	4.001(2)
0.0049(4)	0.0049(4)	0.38952(5)	11.980(10)	4.024(3)
0.0152(2)	0.0154(2)	0.39012(3)	11.925(14)	4.061(5)
0.0187(4)	0.0191(4)	0.39041(2)	11.879(6)	4.067(3)
0.0327(2)	0.0338(2)	0.39126(4)	11.864(10)	4.141(4)
0.0385(2)	0.0400(2)	0.39182(2)	11.808(6)	4.161(2)
0.0467(2)	0.0490(2)	0.39234(1)	11.771(10)	4.197(4)

than for Pd(C): least squares fitting of straight lines to the experimental data with the constraint a = 0.38920 nm for x_i = 0 in Fig. 1.2 yielded

$$\mathrm{Pd(B)}: a(x_\mathrm{B}) = 0.38920 + 0.07697(44)x_\mathrm{B}\ (\mathrm{nm});\ a(x_\mathrm{B}^r) = 0.38920 + 0.06882(44)x_\mathrm{B}^r\ (\mathrm{nm})$$

$$\mathrm{Pd(C)}: a(x_\mathrm{C}) = 0.38920 + 0.06701(9)x_\mathrm{C}\ (\mathrm{nm});\ a(x_\mathrm{C}^r) = 0.38920 + 0.06415(7)x_\mathrm{C}^r\ (\mathrm{nm}).$$

The *decrease* of the density with interstitial element content is also larger for Pd(B) than for Pd(C): least squares fitting of straight lines to the experimental data with the constraint ρ = 11.997 g/cm^3 for x_i^f = 0 in Fig. 1.3 yielded

$$\mathrm{Pd(B)}: \rho(x_\mathrm{B}) = 11.997 - 5.986(36)x_\mathrm{B}\ (\mathrm{g/cm^3});\ \rho(x_\mathrm{B}^r) = 11.997 - 5.396(46)x_\mathrm{B}^r(\mathrm{g/cm^3})$$

$$\mathrm{Pd(C)}: \rho(x_\mathrm{C}) = 11.997 - 4.928(35)x_\mathrm{C}\ (\mathrm{g/cm^3});\ \rho(x_\mathrm{C}^r) = 11.997 - 4.744(34)x_\mathrm{C}^r(\mathrm{g/cm^3}).$$

In the least square fitting errors in both the boron/carbon content and the unit cell parameter/density have been taken into account [27]. Because the uncertainty in the boron/carbon content increases with the boron/carbon content, the data points of relatively low interstitial element content in Figs. 1.2 and 1.3 get relatively large weight in the fittings.

Table 1.6.: Unit cell parameter, a, density, ρ, and number of atoms in the unit cell, n, for various compositions of Pd(B).

Atomic fraction, x_B	Atomic ratio, x_B^r	Unit cell parameter, a (nm)	Density, ρ (g/cm^3)	Numbers of atoms in the unit cell, n
0	0	0.38920(1)	11.997(7)	4.001(2)
0.0136(10)	0.0138(10)	0.39041(7)	11.914(8)	4.061(5)
0.0306(11)	0.0316(12)	0.39098(3)	11.733(10)	4.080(5)
0.0541(14)	0.0572(16)	0.39322(8)	11.648(3)	4.212(6)
0.0752(28)	0.0813(33)	0.39422(4)	11.568(3)	4.301(12)
0.0813(18)	0.0885(21)	0.39608(6)	11.488(6)	4.358(8)
0.1044(27)	0.1166(33)	0.39774(3)	11.444(10)	4.496(13)
0.1187(35)	0.1347(45)	0.39855(1)	11.275(10)	4.521(16)
0.1342(43)	0.1550(57)	0.39994(4)	11.207(10)	4.613(21)
0.1499(43)	0.1763(60)	0.40051(1)	11.099(10)	4.663(21)
0.1651(42)	0.1978(60)	0.40103(6)	11.082(1)	4.749(21)
0.1764(65)	0.2142(96)	0.40272(2)	11.024(10)	4.842(34)

1.4. Discussion

In the *fcc* (Cu type) structure, the octahedral interstices can be occupied, without inducing displacements of matrix atoms, by an interstitial atom with an atomic radius $r_i = (\sqrt{2}-1)r_m \approx 0.41\ r_m$, if one conceives the solvent atoms (with atomic radius r_m) as spheres in contact with each other. Thus, according to Hägg's criterion, $r_i = 0.59 \cdot r_m$, a linear misfit of 44 % between size of the interstitial atom and the available interstitial site is acceptable. Obviously, if such an interstitial atom is introduced into the lattice, distinct local lattice dilatation is induced: adopting the hard spheres model for the solvent atoms, the solvent atoms surrounding the interstitial atom are no longer in contact with each other. Hence, from the point of view of topology, it can be well understood that for all solid solutions investigated here, α-Co(B), Rh(B), Ir(B), Ni(B), Pd(B), Pt(B) and Pd(C), an increase of the unit cell volume with increase of the amount of solute has been observed. This observation supports the notion of the interstitial nature of the solid solutions concerned.

Using the experimentally determined unit cell parameter and density values for the solid solutions, the number of atoms in the unit cell, n, can be calculated applying the relation $n = V_c \cdot \rho \cdot N_{Av}/A$, where $V_c = a^3$ = volume of the unit cell; N_{Av} = Avogadro's number and A = average atomic mass. For the solid solutions Pd(B) and Pd(C), the results are shown in Fig. 1.4 (cf. also Tables 1.6 and 1.5).

Values of the number of atoms in the unit cell > 4 (Fig. 1.4) demonstrate quantitatively that boron and carbon dissolve in palladium interstitially. For a binary interstitial solid solution with a solvent exhibiting the fcc structure, the theoretical number of atoms in the unit cell is $n = 4m + \alpha i$ (m = solvent atom, i = interstitial atom). As the atomic fraction of the interstitial element is $x_i = \alpha/(4+\alpha)$, it follows straightforwardly $n = 4/(1-x_i)$. Consequently, the relationship between the number of atoms in the unit cell and the atomic fraction solute is a non-linear (hyperbolic) function. A linear relation occurs for the dependence of the number of atoms in the interstitial solid solution on the atomic ratio: $n = 4 + 4x_i^r$ ($x_i^r = x_i/x_m$; see above). Comparison of the experimentally determined n values for the solid solutions Pd(B) and Pd(C) with the predicted ones shows very good agreement (Fig. 1.4).

In first order approximation one may assume that the unit cell parameter is linearly dependent on the number of solute atoms in the unit cell [28], independent of the nature of the solid solution (substitutional/intersitital). For a substitutional solid solution the number of atoms in the unit cell does not change upon dissolving the solute. Therefore, on the basis indicated, the unit cell parameter depends linearly on the *atomic fraction* solute. The unit cell parameter may increase or decrease with increasing atomic fraction solute dependent on (i) the atomic size and (ii) the charge transfer between the components. In contrast with substitutional solid solutions, the number of atoms in the unit cell for an interstitial solid solution increases upon dissolving

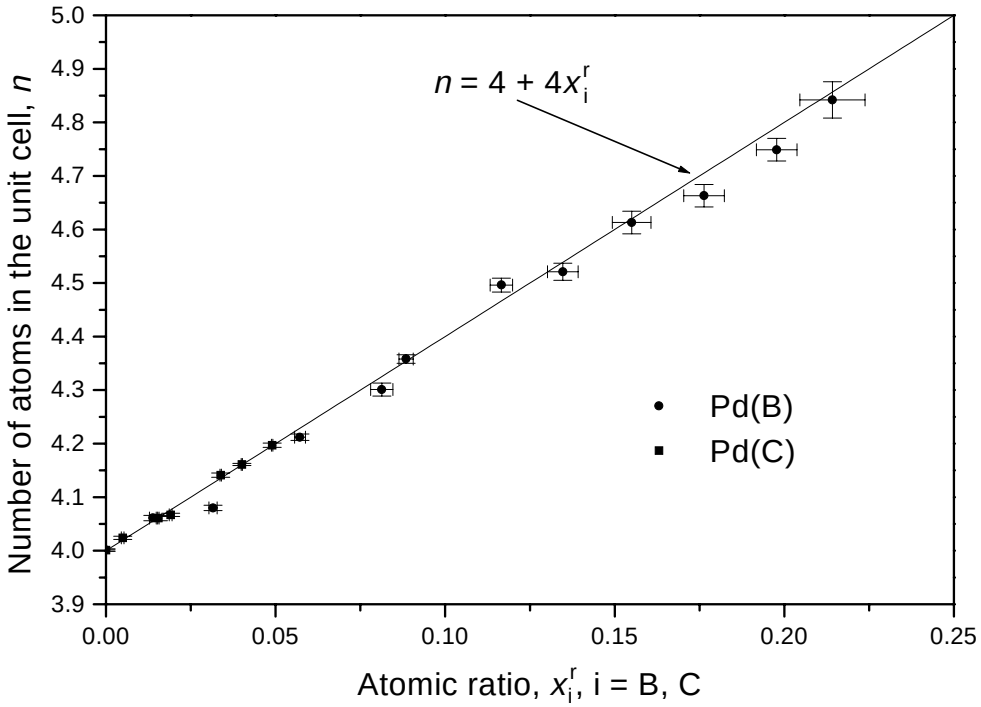

Figure 1.4.: Number of atoms in the unit cell, n, as a function of the atomic ratio, x_i^r (i = B (•), C (■)). Error ranges for the experimental data have been indicated. The full line represents the theoretical relationship $n = 4 + 4x_i^r$.

the solute. Then, on the above basis, the unit cell parameter increases linearly with the *atomic ratio* (Table 1.6 and 1.5 and Fig. 1.2).

Using the determined dependences of the unit cell parameters for the Pd(B) and Pd(C) solid solutions on atomic fraction of the interstitial element (cf. section 1.3.2), the volume size factor Ωsf can be calculated now (cf. section 1.1). It is obtained: for Pd(B) $\Omega sf = 60.86 \cdot 10^6$ and for Pd(C) $\Omega sf = 52.39 \cdot 10^6$. These values are distinctly larger than the critical value $30 \cdot 10^6$ [3] and hence an extensive interstitial solid solubility of carbon and especially for boron in Pd should not be expected concerning to the volume size factor (as also not according to Hägg's criterion; cf. Table 1.1).

In this context it is remarked that from the B^{11} - B^{14} metallic elements isotypical with Cu (Cu, Ag, Au, Al and Pb) only Pb satisfies Hägg's criterion ($r_B/r_{Pb} = 0.526$). However, lead and boron are mutually insoluble and also no boride has been observed in this binary system [29, 30]. Further, the other elements which may be dissolved interstitially, H, C, N and O, show a negligible solubility in lead as well [31], although in all these last cases Hägg's criterion is satisfied ($r_H/r_{Pb} = 0.445,\ r_C/r_{Pb} = 0.501,\ r_N/r_{Pb} = 0.471,\ r_O/r_{Pb} = 0.513$).

Compared with the late transition metals, lead shows a relatively high compressibility [32]. Obviously, even this 'soft-host metal' behaviour does not favour the formation of lead-based interstitial solid solutions. A similar observation has been reported for the W type structure representatives of the alkali and alkaline earth metals which - despite their very high compressibility - do not show solubility for interstitial elements [3].

For the interstitials hydrogen and nitrogen, Hägg's criterion is satisfied for Ag, Au and Al as solvents ($r_H/r_{Ag} = 0.539,\ r_H/r_{Au} = 0.540,\ r_H/r_{Al} = 0.544$ and $r_N/r_{Ag} = 0.571,\ r_N/r_{Au} = 0.572,\ r_N/r_{Al} = 0.576$). Yet, the solubility of both hydrogen and nitrogen in silver, gold and aluminium is insignificant.

On the other hand, the palladium based solid solutions investigated here, with palladium as a relatively small atom as compared to lead, silver and gold, show large solubility not only of hydrogen but also of boron and carbon, although both boron and carbon do not satisfy the Hägg and volume size factor criteria (see above; Table 1.1). It should also be recognized that, if the size of the interstitial atom would play a crucial role in solid solution formation, then the solubility of carbon in palladium is expected to be larger than that of boron in palladium; clearly this does not occur (cf. Table 1.2).

In contrast to *substitutional* solid solutions, the structure of *interstitial* solid solutions is not isopointal with that of the solvent, because of the occupation of additional atomic positions (interstitial sites) by the solute. The unit cell of palladium ($Fm\bar{3}m$, 4 Pd (a)) contains the fourfold octahedral interstitial position (b) $\frac{1}{2},\frac{1}{2},\frac{1}{2}$ and the eightfold tetrahedral interstitial position (c) $\frac{1}{4},\frac{1}{4},\frac{1}{4}$ [33]. EXAFS studies of Pd(B) and diffusion measurements of H in the solid solution Pd(B) with different boron contents [34, 35] indicated occupation of the octahedral position (b) by boron in the palladium unit cell, just as hydrogen does in Pd(H) [36]. It is presumed that carbon occupies also the octahedral atomic position in the host metal lattice [37].

In the solid solution Pd(B), the octahedral atomic position is only partially (statistically) filled; *e.g.* for the composition x_B = 0.176 (Table 1.6; nearly the maximum solubility) the following structure can be proposed: 4 Pd (a), 0.21 × 4 B (b). Thus the solid solutions Pd(B) can be described as a defect (partially filled) NaCl type structure (Pearson-Parthé symbol [38] $cF(8-x)$, $Fm\bar{3}m$).

The average value of the nearest neighbour distance between palladium (atomic position (a)) and the atomic position (b) partially occupied by boron ($d_{Pd-(b)} = d_{002} = a/2$) can be calculated as a function of the boron content from the experimental data gathered in Table 1.6. The results are shown in Fig. 1.5. A straight line has been fitted (least squares analysis) to the experimental data (dashed line in Fig. 1.5). An extrapolation to the stoichiometry "PdB", *i.e.* a hypothetical structure in the system Pd-B showing the NaCl structure with full occupation of the octahedral atomic position (b) by boron, yields the nearest neighbour distance $d_{Pd-B} = 0.2287$ nm.

A theoretical value for d_{Pd-B} can be obtained adopting hard sphere atoms and additivity of

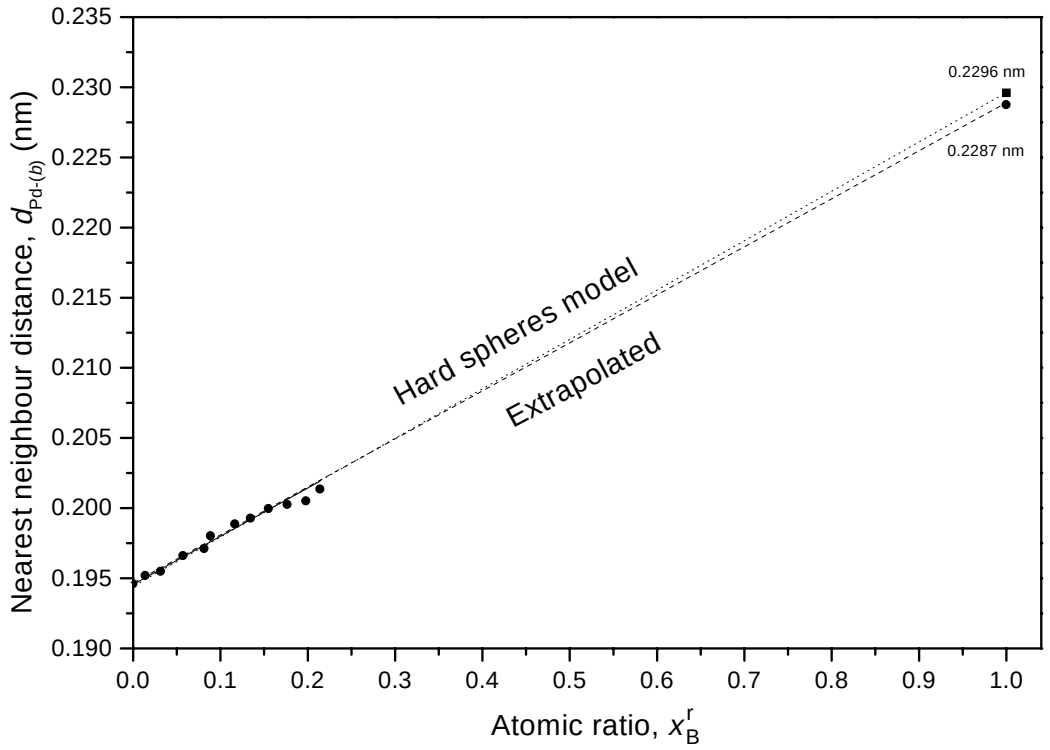

Figure 1.5.: Nearest neighbour distance between Pd lattice site (*a*) and interstitial site (*b*), $d_{\text{Pd}-(b)}$, for the occupation of the octahedral atomic position (*b*) by boron as a function of the atomic ratio x_B^r. The dashed line represents extrapolation of the experimental data for the Pd-B atomic distances in the NaCl structure type; the dotted line indicates corresponding values according to the hard spheres model.

atomic radii. It thus follows $d_{\text{Pd}-\text{B}} = 0.2296$ nm, as obtained from the sum of the atomic radii of palladium and boron (dotted line in Fig. 1.5; data from Ref. [17]). The Pd-B atomic distance as extrapolated from the measured data (dashed line in Fig. 1.5) is clearly smaller than that predicted by the hard sphere model: the difference is $\Delta d_{\text{Pd}-\text{B}} = 0.0009$ nm. This corresponds to a volume difference between the predicted (hard sphere) unit cell volume ($V_c' = 0.09683$ nm^3) and the experimental (extrapolated) unit cell volume ($V_c = 0.09088$ nm^3) of 6.2 %.

Deviation from additivity of ”hard spheres atoms” upon formation of *substitutional* solid solutions was observed previously: the actual volume was smaller then the predicted one [39, 40]. For the palladium-rich substitutional solid solutions with the quasihomological B^{11} - B^{14} elements (Cu, Zn, Ga and Ge) as solutes, only the binary solid solution Pd(Cu) obeys additivity of the pure form volumes (*i.e.* the hard spheres model holds) [41]. The other palladium-rich solid solutions show a large negative deviation from additivity of the pure form volumes: Pd(Zn) $\approx$ 11.9 %, Pd(Ga) $\approx$ 30.6 % and Pd(Ge) $\approx$ 8.4 % [41–43]. Apparently an analogous ”volume

contraction" occurs also upon formation of the *interstitial* solid solution Pd(B).

Interestingly, the largest "volume contractions", as discussed above, are exhibited by the substitutional solid solutions Pd(Al) ($\approx$ 21.7 %), Pd(Ga) ($\approx$ 30.2 %), Pd(In) ($\approx$ 30.2 %) and Pd(Tl) ($\approx$ 26.6 %) [42], as well as the interstitial solid solution Pd(B): *i.e.* the palladium-rich alloys with elements of electron configuration ns^2np^1 as solutes. Thus it may be suggested that these volume contractions observed can be due to pronounced solvent-solute charge transfer upon alloying.

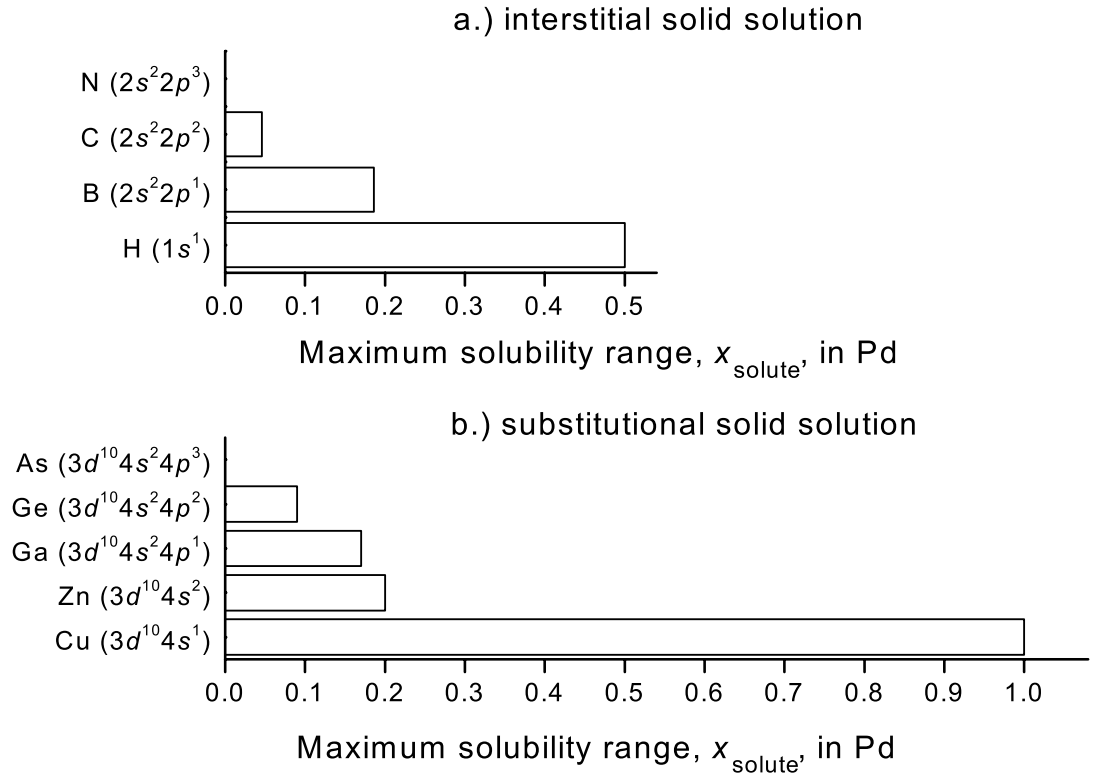

Figure 1.6.: a.) Maximal solubility range and electron configuration of the interstitial elements in palladium (B, C and N are quasihomologous). Data for the interstitial solid solution Pd(H) and the binary system Pd(N) have been taken from [31]; for the interstitial solid solutions Pd(B) and for Pd(C): see Table 1.2. b.) Maximal solubility range and electron configuration of some quasihomologous elements as substitutional solute in palladium. Data for the substitutional solid solutions Pd(Cu), Pd(Zn) and the binary system Pd-As have been taken from Ref. [31]; data for the substitutional solid solutions Pd(Ga) and Pd(Ge) have been taken from Refs. [42, 43].

It is well known that the solubility of various substitutionally dissolved components is controlled by the valence electron concentration (c_{ve}). For solvents isotypical with copper, the value of the valence electron concentration is limited by the contact between the Fermi surface and the

$\{111\}$ Brillouin-zone faces ($c_{ve} \approx 1.36$) [44]. The experimentally observed maximal solubility range for the palladium-based substitutional solid solutions with the quasihomologous elements Cu, Zn, Ga, Ge and As as solutes is shown in Fig. 1.6 (data from Ref. [31]). For these 3*d* solutes, the maximal solubility range is inversely proportional to their potential valency (determinated by the sum of *s* and *p* electrons). Copper (electron configuration $3d^{10}4s^1$) is completely soluble in palladium above 871 K; the solubility of arsenic ($3d^{10}4s^24p^3$) in palladium is negligible [31].

A similar consideration can be given now for the palladium-based interstitial solid solutions. For the interstitial elements H, B, C and N the maximal solubility range in palladium is shown in Fig. 1.6. Three of these interstitial elements (B: $2s^22p^1$, C: $2s^22p^2$ and N: $2s^22p^3$) are quasihomologous and therefore correspond to the analogous sequence of the 3*d* elements Ga ($3d^{10}4s^24p^1$), Ge ($3d^{10}4s^24p^2$) and As ($3d^{10}4s^24p^3$). The maximum solubility of these elements in palladium is also inversely proportional with the potential valency. Apparently, the presumption that the *p*-orbitals of boron are very stable and are therefore associated with the introduction of large strain energies upon dissolving boron in the palladium host lattice (which would consequently severely limit the interstitial solubility of boron in palladium) [4] is not valid.

In contrast to this, the insolubility of the nitrogen in palladium (even at 1673 K [31]) is well explainable from the viewpoint of the valence electron concentration as the limiting factor for interstitial solubility.

Hence, the chemical (electronic) interstitial - matrix interactions govern the formation of the discussed interstitial solid solutions much more than the elastic interstitial - matrix interactions as assessed by the Hägg atomic radius ratio and by the volume-size factor.

1.5. Conclusions

- In contrast with the predictions by old and new rules as the Hägg and volume size factor criteria, boron forms interstitial solid solutions with the *fcc* transition metals Co, Rh, Ir, Ni, Pd and Pt as solvents. In particular palladium exhibits a very large interstitial solid solubility of boron.

- Dissolution of boron in platinum leads to increase of the unit cell parameter in contrast with data reported previously.

- The unit cell parameters, *a*, for Pd(B) and Pd(C) solids solutions have been determinated as a linear function of solute content as

$$\mathrm{Pd(B)} : a(x^r_{\mathrm{B}}) = 0.38920 + 0.06882(44)x^r_{\mathrm{B}}\ (\mathrm{nm})$$

$$\mathrm{Pd(C)} : a(x_{\mathrm{C}}^r) = 0.38920 + 0.06415(7)x_{\mathrm{C}}^r \ (\mathrm{nm})$$

where x_i^r (i = B, C) is the atomic ratio (= x_i/x_{Pd}, with x_i and x_{Pd} as the atomic fractions interstitial element and palladium, respectively).

- The hard sphere model is inconsistent with the observed volume-interstitial content relationship for the interstitial solid solution Pd(B): a significant, negative deviation from the hard sphere model prediction (volume contraction) occurs.
- The solubility of the interstitial elements in Pd is qualitatively inversely proportional with the potential valency.
- The chemical (electronic) interaction appears to govern the interstitial solid solution formation rather than the elastic interaction as characterized by the Hägg atomic radius ratio or the volume size factor.

Chapter 2

The structure of the palladium-rich boride Pd_5B ($Pd_{16}B_3$)

M. Beck, M. Ellner and E.J. Mittemeijer

Abstract: The low-temperature boride Pd_5B ($Pd_{16}B_3$) forms congruently from the corresponding interstitial solid solution Pd(B) (Pearson-Parthé symbol $cF(8-x)$, space group $Fm\bar{3}m$) at 658 K. The structure of Pd_5B has been investigated by X-ray powder diffraction yielding the following structural data: $I4/mmm$, $tI2.38$; unit cell parameters a = 0.28490(4) nm, c = 0.40038(9) nm, $c/a = 1.405 < \sqrt{2}$, with the occupation 2Pd (a) and $0.19 \times$ 2B (b). The crystal chemical data of Pd_5B and some other homeotypic interstitial compounds of transition metals have been compared.

2.1. Introduction

The phase diagram Pd-B as proposed by Rogl [9] shows the *fcc* interstitial solid solution Pd(B) with a large range of homogeneity up to the mole fraction x_B = 0.18 [10], the low-temperature borides $Pd_{\sim 6}B$, $Pd_{\sim 5}B$ and the high-temperature boride $Pd_{\sim 4}B$. The structures of these borides are unknown, whereas the structures of the borides Pd_3B (*oP*16, *Pnma*, Fe_3C type [11]), Pd_5B_2 (*C*2/*c*, Mn_5C_2 type [11]) and Pd_2B (*oP*6, *Pnnm*, anti-FeS_2 type [12]) have been determined.

In contrast to the phase diagram suggested by Rogl [9], the palladium rich part of the phase diagram Pd-B ($0 < x_B < 0.18$) as proposed by Alqasmi *et al.* [7] on the basis of X-ray diffraction analysis shows only one boride - $Pd_{16}B_3$ (= γ phase) (cf. [8]).

The palladium-rich boride $Pd_{16}B_3$ forms congruently from the corresponding Pd(B) solid solution at 673 K and has the homogeneity range $0.151 < x_B < 0.168$ at 638 K; its crystal structure has been reported to be an interstitial superstructure of the Cu type structure (*cF*38, $a = 0.801$ nm $\approx 2a_{Pd(B)}$ [7]). Despite numerous perowskite-like borides and carbides are known [45,46], neither interstitial superstructures based on the Cu type structure nor on other structures corresponding to the Pearson symbol-class *cF*38 have been reported until now [38,47–49]. This study has been made as a part of an investigation on the structure of alloys formed by interstitial elements and transition metals [50].

2.2. Experimental

The alloys were prepared from palladium (99.9 wt.%; Heraeus) and boron (99.5 wt.%; Johnson Matthey) by arc melting under argon (550 hPa, 99.999 vol.%; Messer Griesheim).

The homogeneity of the bulk alloys was checked by means of X-ray diffraction and by metallographic analysis. The boron contents of the alloys were determinated using inductive coupled plasma optical emission spectrometry.

For the X-ray diffraction measurement, the bulk alloys were filed and sieved (mesh size < 50 μm). Before X-ray diffraction analysis was performed the filings were annealed to remove the deformation. To this end the filings were put in quartz capillaries, which were flushed with argon (99.999 vol. %; Messer-Griesheim), evacuated and annealed at selected temperatures in the range from 635 K to 1375 K for times ranging from 5 minutes to seven weeks. To avoid any possible reaction between the samples and the quartz capillaries some samples of the filings were put also in tantalum tubes within the quartz capillaries, thus preventing direct contact of the sample with quartz. It was found that the results obtained with tantalum tubes were identical to those obtained without tantalum tubes. After annealing the samples were water quenched.

Powder diffraction patterns were recorded at room temperature in a Guinier transmission camera (Enraf-Nonius FR552) using Cu$K\alpha_1$ radiation ($\lambda = 0.154056$ nm) and Mo$K\alpha_1$ radiation

($\lambda = 0.070930$ nm). Silicon (99.9999999 wt. %; Ventron, unit cell parameter $a = 0.543094$ nm) was used as internal standard. Single coated CEA Reflex 15 film was used for the Guinier patterns. The positions of the diffraction lines in the Guinier patterns were determined using a Line-Scanner LS 20 (KEJ Instruments). The unit cell parameters were refined by least squares fitting of Bragg's equation to the position of the diffraction lines.

Part of the heat-treated powder was subjected to differential scanning calorimetric (DSC) analysis using a Pyris 1 instrument (Perkin Elmer) at heating rates 20, 30 and 40 K/min. in the temperature range 310 K to 700 K.

2.3. Results

Guinier patterns of the filed, annealed (at 1375 K for 5 min.) and water quenched alloys in the composition range $0 < x_B < 0.18$ showed sharp diffraction lines of the solid solution Pd(B). The interstitial nature of the solid solution Pd(B) (cF(8-x), $Fm\bar{3}m$) has been proved by experimental determination of the unit cell parameter and the macroscopic density: for the composition $Pd_{83.5}B_{16.5}$ the number of atoms in the Pd(B)-unit cell amounts: 4.75 [50]. After the low temperature heat-treatment (for seven weeks) at 735 K of alloys in the composition range from $Pd_{85}B_{15}$ to $Pd_{83.5}B_{16.5}$ only the solid solution Pd(B) was observed as well.

In contrast with the above results, Guinier patterns of alloy-filings in the composition range $0.15 < x_B < 0.17$ revealed a tetragonal distortion of the unit cell of the interstitial solid solution Pd(B) after annealing at 635 K for seven weeks and subsequent water quenching. This indicates the formation of a low temperature phase Pd_5B. Contrary to an earlier report, no diffraction lines based on a Cu type superstructure ($cF38$, a = 0.801 nm $\approx 2a_{Pd(B)}$ [7]; cf. also Powder Diffraction File 47-1043 [51]) were observed in the current investigation of the palladium-rich portion of the binary system Pd-B.

A following heat-treatment at 873 K for 30 minutes of the tetragonally distorted alloy yielded (again) the cubic solid solution Pd(B): apparently the phase transformation Pd(B)$\rightarrow Pd_5B$ is reversible. The corresponding transformation temperature was determined to be 653(1) K by heating of the heat-treated and quenched alloy $Pd_{85}B_{15}$ in a DSC apparatus at constant heating rate.

The phase transformation of the high-temperature cubic solid solution Pd(B) into the low-temperature tetragonal distorted boride Pd_5B follows the fundamental symmetry relationship: for the space group $Fm\bar{3}m$, the maximal non-isomorphic subgroup is the space group $I4/mmm$ [33]. The metrical relationship between the unit cells of the tetragonal low-temperature boride Pd_5B (l) and that of the cubic high-temperature solid solution (h) is as follows: $a_l = b_l \approx a_h/\sqrt{2}$; $c_l \approx c_h$, where the subscripts l and h refer to the low temperature phase and the high temperature phase, respectively.

Table 2.1.: Powder XRD data of Pd_5B ($Pd_{83.5}B_{16.5}$, $I4/mmm$, $tI2.38$, powder heated at 635 K for 7 weeks, subsequently water quenched, Mo$K\alpha_1$ radiation). For calculation of the theoretical powder diffraction intensities, I_{calc}, the program *LAZY PULVERIX* [52] was used.

hkl	d_{calc} (nm)	d_{obs} (nm)	$2\theta_{obs}$	I_{obs}	I_{calc}
101	0.23213	0.23215	17.575	100	100
110	0.20145	0.20150	20.274	43	34
002	0.20019	0.20031	20.396	20	17
200	0.14245	0.14247	28.829	16	10
112	0.14200	0.14206	28.914	37	20
211	0.12141	0.12145	33.957	24	20
103	0.12086	0.12081	34.142	14	10
202	0.11607	0.11608	35.579	9	9
220	0.10073	0.10073	41.229	2	2
004	0.10010	0.10002	41.535	2	1
301	0.09240	0.09235	45.165	2	3
213	0.09216	0.09219	45.247	7	6
310	0.09009	0.09009	46.365	4	3
222	0.08998	0.08995	46.440	2	3
114	0.08964	0.08966	46.601	5	3
312	0.08216	0.08221	51.115	3	4
204	0.08190	0.08189	51.326	1	2
321	0.07752	0.07749	54.475	3	3
303	0.07738	0.07741	54.536	2	1

The splitting of the cubic diffraction line 002, characteristic for the tetragonal distortion, observed in the Guinier patterns recorded with Cu$K\alpha_1$ radiation, as well as the splitting of the 004 and 006 diffraction lines, observed in the Guinier patterns recorded with Mo$K\alpha_1$ radiation, showed that the component of the largest intensity of the 00l-doublet occurs at a larger d-value than observed for the component of smallest intensity. With respect to the multiplicity factors for the tetragonal $\{h00\}$ and $\{00l\}$ planes (4 and 2, respectively), this kind of the tetragonal distortion corresponds to values of the axial ratio $c/a < \sqrt{2}$.

The diffraction lines of the palladium-rich boride Pd_5B were indexed in accordance with the tI(4-x) unit cell, which possess the unit cell parameters a = 0.28490(4) nm, c = 0.40038(9) nm. The figure of merit according to [53] was found to be F_{19} = 75(0.013,19). The experimentally determined number of atoms in the unit cell of the Pd(B) solid solution of composition $Pd_{83.5}B_{16.5}$ equals 4.75 (see above, [50]). Thus, the following structure can be proposed for the

low temperature tetragonal phase Pd_5B in the space group $I4/mmm$: 2 Pd (*a*); 0.19×2 B (*b*). The powder diffraction data obtained for Pd_5B have been presented in Table 2.1.

2.4. Discussion

At high temperatures palladium shows large interstitial solubility for boron [7, 9, 10] and an extensive substitutional solubility for the homologous elements aluminium and gallium [42]. As result of the palladium substitution by aluminium and gallium (i) the valence electron concentration and the configurational entropy increase and (ii) a large negative enthalpy of formation is observed [42]. Then, because an interstitially dissolved element as B is relatively valence electron rich, it may be expected that alloying of palladium with boron would be possible while maintaining the Cu type structure of the solvent Pd lattice.

At low temperatures substitution of palladium by aluminium and gallium cannot occur on the basis of the Pd *fcc* structure and, consequently, different crystal structures have been observed: Pd_5Al (*oP*24, *Pnma*; [54]) and $Pd_{13}Ga_5$ (*mC*36, $C2/m$; [55]). Therefore, destabilisation of the interstitial *fcc* solid solution at relatively low temperatures may also be expected for the binary system Pd-B. In this case tetragonal lattice distortion of the high-temperature phase has been reported here (section 2.3). The first-order phase transformation Pd(B)$\rightarrow$$Pd_5B$ shows the characteristic space group-relationship $Fm\bar{3}m \xrightarrow{t3} I4/mmm$ [56].

An interesting similarity to the palladium-rich portion of the phase diagram for the system Pd-B occurs in the hydrogen-rich part of the phase diagram for the system Pd-H. The interstitial element hydrogen dissolves at high temperatures while the cubic structure of palladium is maintained, whereas at low temperatures and higher hydrogen contents the solid solution Pd(H) becomes unstable [57]. Thus the low-temperature hydride $PdH_{1.33}$ has been observed (*i.e.* the γ phase, T $<$ 873 K; *tI*(4-*x*), *a* = 0.2896 nm, *c* = 0.3333 nm; $c/a = 1.151 < \sqrt{2}$) [58] (cf. Powder Diffraction File 73-0004 [51]). The palladium sublattice is not fully occupied in this hydride (the number of palladium atoms in the unit cell is $\approx$ 1.5, whereas the number of Pd sites is 2); the small unit cell volume of $PdH_{1.33}$ ($V_c = 0.02795$ nm$^3 < 2V_{Pd} = 0.02948$ nm^3; where V_{Pd} = atomic volume of palladium) is indeed compatible with the presence of vacancies on the palladium sublattice.

The palladium-rich boride Pd_5B ($0.15 < x_B < 0.17$) occurs nearly at the same valence electron concentration as the hydride $PdH_{1.33}$ ($0.54 < x_H < 0.57$ [58]) if the valence electron contribution of palladium is taken equal to zero; the valences of B and H are 3 and 1, respectively. The differences between the boride Pd_5B and the hydride $PdH_{1.33}$ involve (i) complete occupation of the palladium sublattice in Pd_5B (cf. the relatively large unit cell volume of Pd_5B as compared to $PdH_{1.33}$: $V_c = 0.03250$ nm$^3 > 2V_{Pd} = 0.02948$ nm^3; cf. above) and (ii) the occurrence of vacancies on the sublattice of the octahedral interstices formed

by the Pd sublattice, *i.e.* vacancies at the atomic positions (*b*) of the space group $I4/mmm$.

The distortions of the tetragonal body centered (tI(4-x)) unit cell as compared to the cubic body centered unit cell, are shown in Fig. 2.1, as function of the number of atoms in the unit cell, n, for phases composed of a transition metal as solvent and an interstitial element as solute. The small slope, $\Delta(c/a)/\Delta n$, between Pd (for the number of atoms in the 'tetragonal' unit cell $n = 2$ and $c/a = \sqrt{2}$) and Pd_5B (for $2.0 < n < 2.38$) corresponds to a large change of the valence electron concentration ($0 < c_{ve} < 0.5$). The large change of the slope, $\Delta(c/a)/\Delta n$, between Pd_5B and $PdH_{1.33}$ is related to the introduction of vacancies on the palladium sublattice for $PdH_{1.33}$ (note, that Pd_5B and $PdH_{1.33}$ are not isotypical but only homeotypical structures). The c_{ve} does not change distinctly in this n-range (Pd_5B: $c_{ve} \approx 0.5$; $PdH_{1.33}$: $c_{ve} = 0.57$).

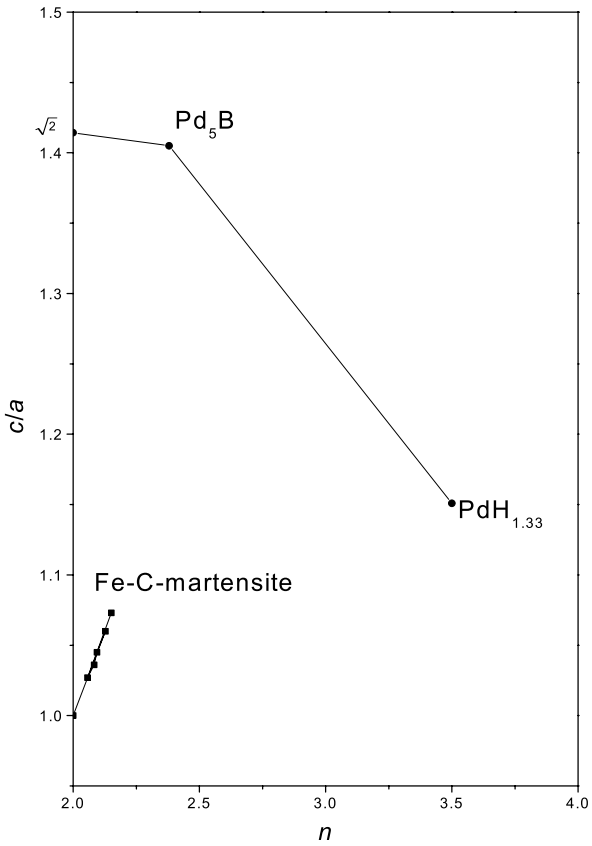

Figure 2.1.: Axial ratio, c/a, of the tetragonal body centered (tI(4-x)) unit cell as a function of the numbers of atoms in the $tI(4-x)$ unit cell, n, for phases composed of a transition metal as solvent and an interstitial element as solute ([26, 58], this work).

In contrast with the palladium-based interstitial compounds, the axial ratio c/a of the metastable Fe-C-martensite increases strongly upon filling of the (*b*)-type distorted octahedral interstices ($I4/mmm$) with carbon. Consequently, the unit cell volume increases with the number of carbon atoms in the Fe-C-martensite unit cell ($0.02355\ \text{nm}^3 < V_c < 0.02477\ \text{nm}^3$ for $2 < n < 2.08$) [26]. The martensite Fe(C) is a derivative of the *bcc* (W type) structure [49], whereas the palladium-containing phases Pd_5B and $PdH_{1.33}$ are derivates of the *fcc* (Cu type) structure.

2.5. Conclusions

- The low-temperature boride Pd_5B forms congruently from the cubic intersitial solid solution Pd(B) ($cF(8-x),\ Fm\bar{3}m,\ a = 0.40103(6)$ nm) upon annealing below 653(1) K.
- Pd_5B shows a tetragonal distortion of the Pd(B) unit cell. The B atoms occupy the distorted octahedral interstices formed by the Pd sublattice in a random way; the Pd sublattice is fully occupied. This is in contrast with the pendant structure in the Pd-H system, $PdH_{1.33}$, that is characterized by vacancies on the Pd sublattice.
- The crystal structure data for Pd_5B are: $I4/mmm$; $a = 0.28490(4)$ nm, $c = 0.40038(9)$ nm; 2Pd (*a*), 0.19 $\times$ 2B (*b*).

Chapter 3

Powder diffraction data for borides Pd_3B and Pd_5B_2 and the formation of an amorphous boride Pd_2B

M. Beck, M. Ellner and E.J. Mittemeijer

Abstract: Powder diffraction data and refined unit cell parameters of two palladium borides were determined. For Pd_3B (space group *Pnma*; Fe_3C type) it was found that *a*=0.54602(3) nm, *b*=0.75596(4) nm, *c*=0.48417(4) nm and for Pd_5B_2 (space group $C2/c$; Mn_5C_2 type) *a*=1.27759(12) nm, *b*=0.49497(5) nm, *c*=0.54704(4) nm, β=97.049(7)°. Further it was shown that the position of the principal scattering peak of the amorphous Pd_2B fulfils the Nagel-Tauc criterion about glass forming ability.

3.1. Introduction

The binary phase diagram Pd-B (for the most recent evaluation, see [9]) shows a large homogeneity range for the terminal interstitial solid solution Pd(B) up to the mole fraction x_B = 0.186 [10], the low-temperature borides $Pd_{\sim 6}B$, $Pd_{\sim 5}B$ and the high-temperature boride $Pd_{\sim 4}B$. The exact stoichiometry of the palladium-richest boride $Pd_{\sim 6}B$ is unknown; according to Ipser and Rogl [6], the composition would correspond to $x_B = 0.14$. Alqasmi *et al*. proposed for the composition range $0 < x_B < 0.186$ only the solid solution Pd(B) and the palladium-rich boride $Pd_{16}B_3$ (a = 0.8010 nm) [7].

The structure of the borides Pd_3B (Pearson symbol *oP*16, space group *Pnma*, Fe_3C type; [11]), Pd_5B_2 (*mC*28, *C*/2*c*, Mn_5C_2 type; [11]) and Pd_2B (*oP*6, *Pnnm*, anti-FeS_2 type; [12]) has been determined by single crystal X-ray diffraction investigations.

The borides Pd_3B and Pd_5B_2 melt congruently at 1398 K and 1350 K, respectively, as indicated by Rogl [9]. In contrast, a peritectoid formation from the solid solution Pd(B) and Pd_5B_2 at 1163 K was suggested for Pd_3B by Alqasmi *et al*. [7]. A deep eutectic occurs at $x_B \approx 0.365$ and T = 1237 K in the binary system Pd-B [9]. It is common knowledge that in the neighbourhood of a deep eutetic glass formation is often found [59]. Indeed, amorphous Pd-B alloys were prepared by means of the melt-spinning technique in the composition range $0.24 < x_B < 0.30$ [60].

No powder diffraction data have been given for the borides Pd_3B and Pd_5B_2 (cf. [51]). This article primarily reports such powder diffraction data to facilitate phase identification in the very complex palladium-rich portion of the phase diagram of the binary system Pd-B.

3.2. Experimental

The Pd-B alloys were prepared from palladium (99.9 wt. %; Heraeus) and boron (99.5 wt. %; Johnson Matthey) by arc melting under argon (550 hPa, 99.999 vol. %; Messer Griesheim). Amorphous alloys were prepared from the as-cast Pd-B alloys by melting and liquid quenching in a rotating-propeller apparatus [61]. The homogeneity of the crystalline bulk alloys as well as the amorphous nature of the liquid-quenched alloys were checked by means of Guinier diffraction patterns taken with an Enraf-Nonius FR552 camera using Cu$K\alpha_1$ radiation and by metallographic investigations.

The bulk alloy of composition Pd_5B_2 was heated in an evacuated silica capillary at 1213 K for 38 hours in order to ensure homogenization and then water quenched. For the unit cell parameter measurements the bulk alloys were filed. The filings were put in quartz capillaries, which were flushed with argon (99.999 vol. %; Messer-Griesheim), evacuated and annealed at

Table 3.1.: Experimental conditions used for recording Pd_3B powder XRD pattern.

Radiation type, source	X-ray, Cu$K\alpha_1$
Generator settings	45kV, 40mA
Wavelength	0.154056 nm
Primary monochromator	germanium (111)
Divergenz slits	0.25 °
Receiving slit	0.1 mm
Range in 2θ	21.5°–125.9°
Scan technique	continuous: step size 0.01° 2θ
Counting time per step	9 s
Detector	proportional counter
Specimen motion	rotation

973 K for 30 minutes (Pd_3B) or 1213 K (Pd_5B_2) for 20 minutes, respectively, to remove internal stress and then water quenched.

Powder diffraction patterns were recorded at room temperature in a Guinier transmission camera (see above) using Cu$K\alpha_1$ (λ = 0.154056 nm) and Fe$K\alpha_1$ radiation ($\lambda = 0.193604$ nm). Silicon (99.9999999 wt. %; Ventron, a = 0.543094 nm) was used as an internal standard. Single coated CEA Reflex 15 film was used for the Guinier patterns. Unit cell parameters were refined by least squares fitting of Bragg's equation to the positions of the diffraction lines in the range $23^o < 2\theta < 77^o$ for Pd_3B and $39^o < 2\theta < 69^o$ for Pd_5B_2. Powder diffraction intensities observed in the Guinier patterns of Pd_5B_2 were determined densitometrically on a Line-Scanner LS 20 (KEJ Instruments). The intensities of the Pd_3B reflections were determined using a Philips X'Pert diffractometer with Bragg-Brentano geometry and Cu$K\alpha_1$ radiation and employing Philips ProFit software. Further details of the data collection procedure have been given in Table 3.1. For calculation of powder diffraction intensities the program *LAZY PULVERIX* was used [52].

3.3. Results

The X-ray diffraction patterns of the alloy Pd_3B (powder heated at 973 K for 30 min. and subsequently water quenched) showed diffraction lines of the structure type Fe_3C (cementite). A Rietveld refinement (using the GSAS package [62]) of powder diffraction data recorded with the diffractometer (cf. Section 3.2) confirmed the atomic positions in the unit cell as given by Stenberg [11] (refined profile parameters: 3; refined background parameter: 3; refined

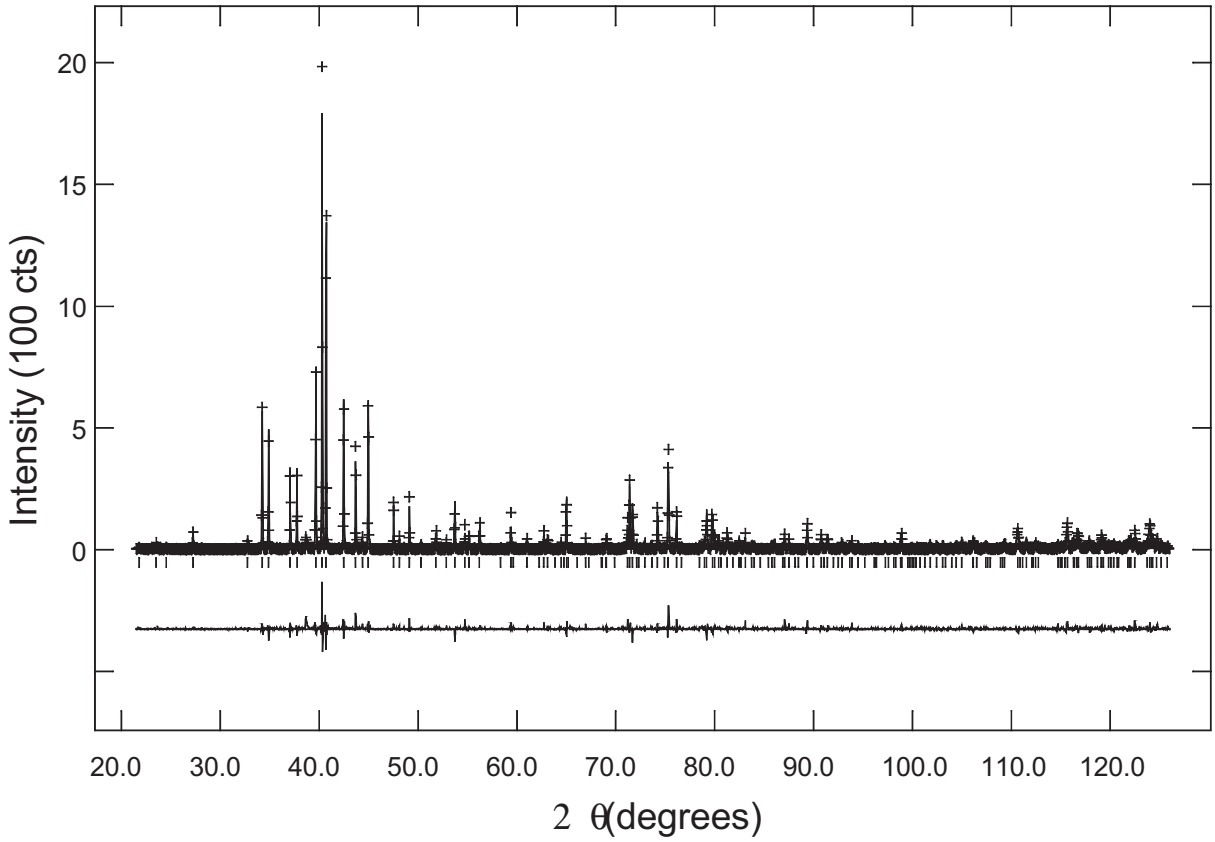

Figure 3.1.: Experimental (+), calculated (continuous line) and difference (below) plots for Pd_3B.

overall thermal parameter: 1; wR_p: 0.32; $R(F^2)(F^2 \geq \sigma(F^2))$: 0.13; atomic position *x*, *y*, *z* (this work/ [11]): Pd 8(*d*) 0.1800(2)/0.1798, 0.0695(2)/0.0700, 0.3284(3)/0.3276; Pd 4(*c*) 0.0384(3)/0.0372, $\frac{1}{4}$, 0.8456(4)/0.8446; B (not refined) 0.884, $\frac{1}{4}$, 0.433). The result is presented in Fig. 3.1.

For alloy Pd_5B_2 (powder heated at 1213 K for 20 min. and subsequently water quenched) diffraction lines of the structure type Mn_5C_2 were observed in the Guinier patterns.

For calculation of X-ray powder diffraction intensities, the atomic positions of Pd_3B and Pd_5B_2 determined by Stenberg [11] were used. The experimental and calculated powder diffraction data have been gathered in Tables 3.2 and 3.4. For Pd_3B the figure of merit according to de Wolff [63] (1968) is $M_{20} = 100$ and that according to Smith and Snyder [53] is $F_{44} = 83(0.009, 61)$. For Pd_5B_2 the figure of merit according to de Wolff [63] is $M_{20} = 74$ and that according to Smith and Snyder [53] is $F_{25} = 76(0.010, 35)$.

The liquid quenched alloys of compositions $Pd_{67}B_{33}$ and $Pd_{66}B_{34}$ were completely amorphous with the principal scattering maximum in the range of 4.17 $nm^{-1} < 2\sin\theta/\lambda < 4.76$ nm^{-1}.

Table 3.2.: Powder XRD data of Pd_3B (powder heated at 973 K min. and subsequently water quenched; Cu$K\alpha_1$ radiation; I_{obs}: diffractometer data, d_{obs}: Guinier camera data): space groupe *Pnma*, Pearson symbol *oP*16, refined unit cell parameter data: $a = 0.54602(3)$ nm, $b = 0.75596(4)$ nm, $c = 0.48417(4)$ nm.

hkl	d_{calc} (nm)	d_{obs} (nm)	$2\theta_{obs}$	I_{obs}	I_{calc}
011	0.40772				< 1
020	0.37798	0.37779	23.529	2	1
101	0.36226	0.36216	24.560	< 1	< 1
111	0.32669	0.32676	27.270	3	3
200	0.27301	0.27299	32.779	2	2
121	0.26154	0.26161	34.248	31	29
210	0.25678	0.25681	34.908	25	26
002	0.24209	0.24210	37.104	21	21
201	0.23781	0.23783	37.796	17	18
211	0.22685	0.22689	39.692	47	49
031	0.22353	0.22361	40.300	100	100
220	0.22132	} 0.22135	40.730	89	{ 45
102	0.22131				43
112	0.21239	0.21241	42.525	45	41
131	0.20686	0.20692	43.711	29	24
022	0.20386	0.20388	44.397	2	2
221	0.20129	0.20132	44.991	42	36
122	0.19098	0.19100	47.567	13	11
040	0.18899	0.18907	48.085	3	2
230	0.18517	0.18520	49.153	12	10
202	0.18113	0.18110	50.343	1	1
212	0.17615	0.17614	51.864	5	5
231	0.17295	0.17300	52.880	2	2
301	0.17037	0.17037	53.759	13	11
141	0.16756	0.16761	54.720	6	4
132	0.16628				< 1
311	0.16620	0.16624	55.209	5	3
222	0.16334	0.16336	56.266	8	6
013	0.15783	0.15780	58.435	< 1	< 1
240	0.15539	0.15542	59.420	8	6
321	0.15532				< 1

continued on next page

continued form previous page

hkl	d_{calc} (nm)	d_{obs} (nm)	$2\theta_{obs}$	I_{obs}	I_{calc}
103	0.15477				< 1
113	0.15163	0.15166	61.050	3	2
042	0.14897				< 1
241	0.14796	0.14799	62.733	4	3
232	0.14708	0.14707	63.170	3	3
302	0.14548				< 1
051	0.14432	0.14429	64.533	2	1
142	0.14372				< 1
123	0.14323	0.14323	65.065	17	14
312	0.14286				< 1
331	0.14114				< 1
151	0.13953	0.13952	67.021	2	2
203	0.13893				< 1
213	0.13664				< 1
400	0.13594				< 1
033	0.13591				< 1
322	0.13577	0.13577	69.132	4	3
410	0.13433				< 1
250	0.13226	0.13227	71.230	9	6
133	0.13188	0.13189	71.471	22	17
401	0.13138	0.13137	71.796	14	13
242	0.13077				< 1
223	0.13040				< 1
411	0.12944	0.12942	73.053	2	2
420	0.12839	0.12840	73.728	2	1
251	0.12759	0.12761	74.262	16	11
341	0.12654				< 1
060	} 0.12599	0.12598	75.387	34	{ 7
332					19
152	0.12484	0.12480	76.228	12	8

Table 3.4.: Powder XRD data of Pd_5B_2 (powder heated at 1213 K for 20 min. and subsequently water quenched; Fe$K\alpha_1$ radiation; I_{obs} and d_{obs}: Guinier camera data): space group $C2/c$, Pearson symbol $mC28$, refined unit cell parameter data: $a = 1.27759(12)$ nm, $b = 0.49497(5)$ nm, $c = 0.54704(4)$ nm, $\beta = 97.049(7)^\circ$.

hkl	d_{calc}	d_{obs}	$2\theta_{obs}$	I_{obs}	I_{calc}
200	0.63397				<1
110	0.46108				<1
$11\bar{1}$	0.35944				<1
111	0.34395				1
310	0.32141				<1
400	0.31698				2
$31\bar{1}$	0.28864	0.28867	39.187	17	13
002	0.27146	0.27143	41.787	11	7
311	0.26591	0.26591	42.697	16	13
$20\bar{2}$	0.26142	0.24141	43.469	10	9
020	0.24749	0.24739	46.069	14	23
202	0.23915	0.23910	47.764	41	26
$11\bar{2}$	0.23863	0.23859	47.873	53	38
220	0.23054				<1
112	0.22949	0.22949	49.899	11	13
510	0.22570	0.22567	50.803	100	100
021	0.22519	0.22530	50.892	51	55
$40\bar{2}$	0.21995	0.21993	52.228	29	19
$31\bar{2}$	0.21762	0.21761	52.826	50	32
$51\bar{1}$	0.21697	0.21698	52.992	17	16
$22\bar{1}$	0.21569	0.21561	53.354	26	15
600	0.21132	0.21133	54.523	31	4
221	0.20887	0.20886	55.224	19	20
511	0.20077	0.20075	57.657	13	14
312	0.19846	0.19848	58.383	23	21
420	0.19507				3
402	0.19471	0.19469	59.630	19	15
$42\bar{1}$	0.18816	0.18816	61.925	9	10
$51\bar{2}$	0.18369	0.18370	63.598	8	7
022	0.18289	0.18287	63.924	6	4
$22\bar{2}$	0.17972				2
421	0.17932				<1
$60\bar{2}$	0.17765	0.17766	66.033	12	10
222	0.17197	0.17202	68.492	4	5
$11\bar{3}$	0.17107	0.17108	68.921	25	16

3.4. Discussion

The binary system Pd-B shows a certain similarity to the metastable system Fe-C concerning the occurrence of isotypical pair-phases: the borides Pd_3B-Pd_5B_2 and the carbides Fe_3C-Fe_5C_2. The cementite structure type (Fe_3C) can be interpreted as a twinned hcp structure of the metal atoms with occupation of the trigonal-prismatic voids by interstitial atoms [49, 64]. This structure type has many representatives among the transition metal elements with interstitial elements as boron and carbon, but not nitrogen and oxygen [47, 48]. The structure type Pd_5B_2 (Mn_5C_2) can be derived from the cementite structure type by a 'structural-block changing' [64, 65]. Only three interstitial element-containing representatives of this structure type - Mn_5C_2, Fe_5C_2 and Pd_5B_2 - have been observed [48].

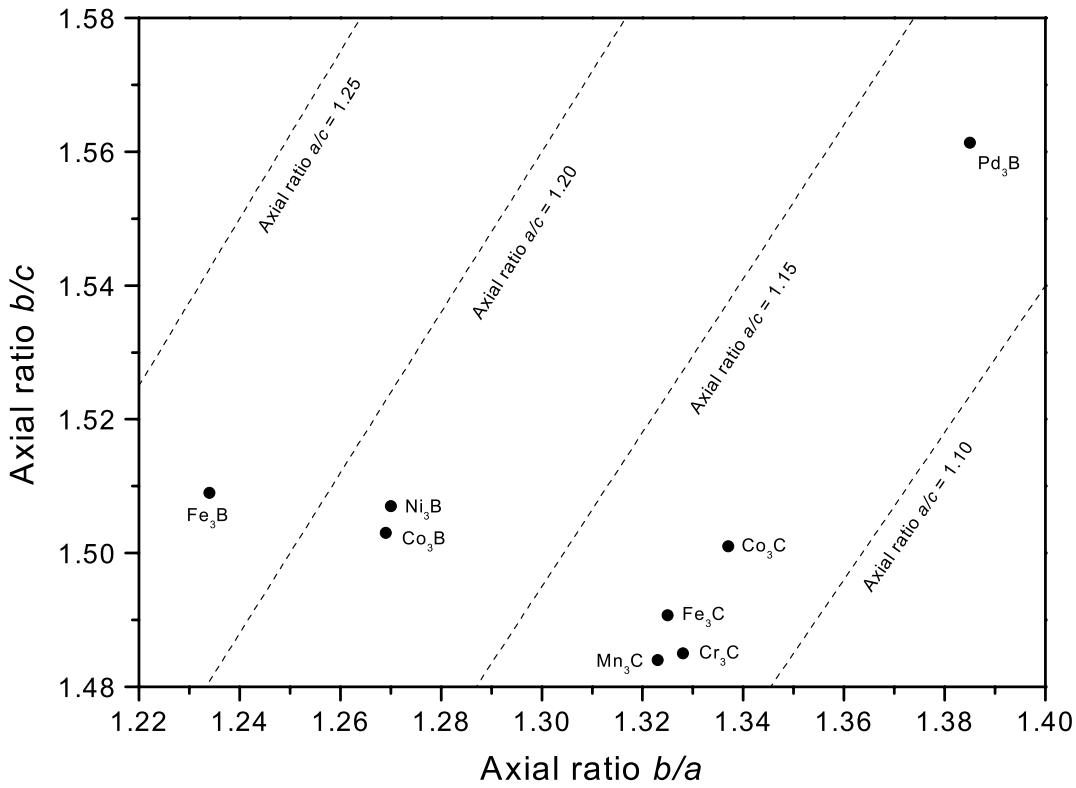

Figure 3.2.: Axial ratios b/c and b/a for the transition metal-containing borides and carbides of the cementite structure type ([48]; this work).

The axial ratios b/c and b/a are shown for the transition metal-containing borides and carbides with the cementite structure type in Fig. 3.2. Pd_3B shows the largest axial ratios b/a and

b/c and therefore also the largest elongation of the unit cell, upon introduction of the interstitial atom, among all phases isotypical with Fe_3C. On the other hand, Pd_3B as well as the quasihomological $3d$ transition metal-containing carbides Cr_3C ...Co_3C exhibit the smallest values of the axial ratio a/c. This can be interpreted as a tendency to adopt the tetragonal unit cell of the U_3Si_2 structure type which is structurally related to the cementite structure type [66].

The Nagel-Tauc criterion describes a model of metallic glass formation based on nearly-free-electron approximation [67]. This criterion requires $2K_F \backsimeq K_p$ in order for an amorphous phase transformation to be possible, where K_F = Fermi sphere diameter and K_p = wave number of the first peak. In the present case, the wave number, K_p, was determined from the Bragg's equation applied to the principal scattering maximum of the amorphous alloys $Pd_{67}B_{33}$ and $Pd_{66}B_{34}$: $K_p = 4\pi\sin\theta/\lambda = 28.0$ nm^{-1} using the data given in section 3.3. The value of the diameter of the Fermi sphere was calculated from the relationship $K_F = \sqrt[3]{3\pi c_{ve}\rho N_{Av}/\sum_i x_i m_i} =$ 14.4 nm^{-1} [68] (where c_{ve} = valence electron concentration; ρ = density; N_{Av} = Avogadro's number; m_i = atomic mass of the i-component; with the approximations valency of palladium = 0 and valency of boron = 3 for T= 0 K): $2K_F = 28.8$ nm^{-1} $\approx K_p$. This shows that the occurrence of amorphous alloys with compositions $Pd_{67}B_{33}$ and $Pd_{66}B_{34}$ produced by liquid quenching corresponds well with the prediction according to Nagel-Tauc criterion.

Chapter 4

Decomposition of the interstitial solid solution Pd(B)

M. Beck and E.J. Mittemeijer

Abstract: The decomposition at 628 K of the Pd(B) solid solution containing 6 at. % boron was analyzed by use of, primarily, X-ray diffraction. A structure model was used to simulate the X-ray diffraction-line profiles. The decomposition was described as the precipitation of a boron-poor *fcc* phase in the parent *fcc* phase gradually enriching in boron. The experimentally determined width of the miscibility gap is different from previous experimental results, but agrees with theoretical data obtained on the basis of the quasi-chemical approximation. Further, the microstrain in the decomposed state was measured and compared with that of the initial, quenched supersaturated solid solution; good agreement was observed between results obtained from X-ray diffractometry and transmission electron microscopy.

4.1. Introduction

Palladium exhibits a very large interstitial solubility of boron up to a mole fraction $x_B = 0.18$ [10]. The solid solution Pd(B) is a high temperature phase (*fcc* Pd lattice with boron in the octahedral interstices; space group: $Fm\bar{3}m$, Pearson-Parthé symbol $cF(8-x)$) which can be retained at room temperature by quenching. The solid solution decomposes in the range of $0.02 < x_B < 0.10$ between 585 K and 683 K in two *fcc* interstitial solid solutions [7, 13, 69]. Below 585 K and in the composition range $0.02 < x_B < 0.15$ a two-phase region has been reported, where the *fcc* interstitial solid solution decomposes in an *fcc* Pd(B) solid solution and the tetragonal γ-phase (Pd_5B, $I4/mmm$, $tI2.38$ [70]). This miscibility gap and the two phase region were exhibited by X-ray diffraction analysis using samples heat treated in a temperature range of 553 K to 723 K for 3 to 7 days [13].

A miscibility gap is a rare phenomenon for a binary interstitial solid solution based on the *fcc* structure. Such a miscibility gap has only been reported for three systems: Th-C, Pd-H and Pd-B [31]. The miscibility gap of the binary system Pd-H has been investigated extensively (*e.g.* [71]), whereas the demixing of the solid solutions of Th(C) and Pd(B) has been the subject of only a few works [7, 13, 69, 72–74].

All reported structural investigations of the miscibility gaps of these *fcc* interstitial solid solution, known to us, were confined to the start and final states of the decomposition. The reaction path and the kinetics of this type of decomposition have not been investigated in detail until now. The final state of the decomposition consists of two phases isotypical with the parent *fcc* homogeneous solid solution. The two product phases contain different contents of the interstitial element and, therefore, these phases have different unit cell parameters, different from that of the parent phase. Hence, X-ray diffraction analysis is a useful method for studying the decomposition process.

In this paper results are reported of a project devoted to the formation of the miscibility gap in the Pd-B system primarily using X-ray diffractometry. The observed X-ray diffraction-line profiles have been simulated on the basis of a simple structural model for the decomposed state as a function of the degree of decomposition.

4.2. Model for calculation of the X-ray diffraction-line profiles

In the Pd(B) solid solution considered decomposition process *via* a redistribution of boron, while maintaining the same *fcc* parent Pd sublattice, leading to a boron-rich and a boron-poor Pd(B) phase, which to our present knowledge, both exhibit a random distribution of boron, as

holds for the parent Pd(B) phase. The unit cell parameter of Pd(B) depends strongly on the boron content [50]. It follows that decomposition of the Pd(B) solid solution leads to spatial fluctuations in the unit cell parameter. In an X-ray diffraction experiment lattice-spacing variation can be measured in a direction along the diffraction vector. Thus, to model an X-ray diffraction *hkl* line profile recorded from a (partly) decomposed Pd(B) solid solution, it can be proposed that a one-dimensional variation of the lattice spacing is considered.

It may be suggested that decomposition of Pd(B) is diffusion controlled. Then, the nature of the evolving concentration profile may be described, for a start, with $c(x,t) = A + B \cdot \mathrm{erf}(\frac{x}{2\sqrt{Dt}})$ [75], where $x =$ position (in the crystal), $D =$ diffusion coefficient, $t =$ time and A and B are constants. Further, recognizing that the unit cell parameter depends linearly on boron content [50], at a certain, intermediate stage of decomposition the unit cell parameter profile may be subdivided into three zones, as follows.

The first zone of constant unit cell parameter represents the boron-poor product phase; the third zone of constant unit cell parameter represents the boron-rich product phase; the second zone in between represents the decomposing matrix (see Fig. 4.1):

$$a(x) = \begin{cases} a_1 & \text{for } 0 < x < S_1\text{; zone 1} \\ \frac{a_1+a_2}{2} + \frac{a_1-a_2}{2} \cdot \mathrm{erf}\left(\frac{2x-(S_2+S_1)}{S_2-S_1}\right) & \text{for } S_1 < x < S_2\text{; zone 2} \\ a_2 & \text{for } S_2 < x < S_{\max}\text{; zone 3,} \end{cases} \tag{4.1}$$

where a denotes the unit cell parameter, x represents position, S_1 and S_2 designate the interfaces between the zones and $S_{\max}$ is the largest considered x-value.

As a result, the evolution of the unit cell parameter, and thus of the boron content, is given in Fig. 4.1 as a function of the position in the structure in a direction parallel to the diffraction vector.

For the calculation of the *hkl* diffraction-line profile the crystal is conceived as a set of (*hkl*) lattice planes perpendicular to the diffraction vector with a distance between the lattice planes given by $d(x) = a(x)/\sqrt{h^2+k^2+l^2}$. The X-ray diffracted *hkl* intensity, I, depends on the diffraction angle 2θ according to [76]:

$$I(\theta) = \left| \sum_k \left(f \cdot \mathrm{e}^{i \cdot \frac{4\pi}{\lambda} \sin(\theta) \cdot x_k} \right) \right|^2, \tag{4.2}$$

where f is the atomic scattering factor, λ the wavelength of the X-ray radiation used and x_k is the position of the k^{th} diffracting plane ($x_k = \sum_{j=1}^{k} d_j$), where d_j is the lattice spacing assigned to lattice plane j. Because of the very small atomic scattering factor of boron, the influence of the boron atoms on the diffracted intensity can be neglected. The boron content is primarily reflected through its effect on the lattice spacing.

The line profile as described by Eq. 4.2 represents the true, so-called structural line profile. In a real diffraction experiment line broadening occurs also due to the wavelength distribution and instrumental aberrations, which effects are combined in the so-called intrumental broadening function. The observed line profile is then given by the convolution of the structural line profile and the instrumental line profile [76]. It should be noted that a source of structural line broadening, other than the compositional lattice-spacing variation considered in the model, as due to the presence of microstrains, will show up as an additional contribution to the 'instrumental' line broadening as determined by the fitting to be discussed (see section 4.7).

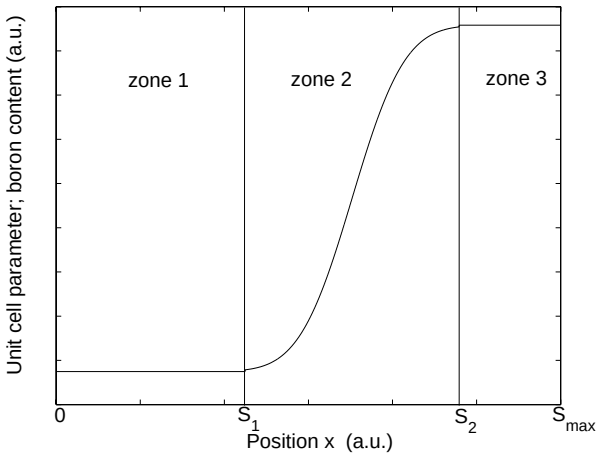

Figure 4.1.: Variation of the unit cell parameter, and therefore of the boron content, of a partly decomposed Pd(B) solid solution as a function of the position in the crystal (see text and Eq. 4.1).

To take into account the instrumental broadening of the diffractometer in the experiment, the calculated intensity (cf. Eq. 4.2) is convoluted with a symmetric pseudo-Voigt function,* $PV(2\theta)$. Recognizing the presence of the $K\alpha$ doublet in the X-ray radiation used in the experiments (cf. section 4.3), an α_2 component is added to the calculated α_1 component with a fixed intensity ratio $I(K\alpha_2)/I(K\alpha_1) = 0.5$. The positions S_1 and S_2 of the interfaces between the transition zone (zone 2 in Fig. 4.1) and the boron-poor phase (zone 1) and the boron-rich phase (zone 3), respectively, have to be determined by fitting, but obey $\mathrm{erf}(\frac{2x-(S_2+S_1)}{S_2-S_1}) = -0.99$ for S_1 and $\mathrm{erf}(\frac{2x-(S_2+S_1)}{S_2-S_1}) = +0.99$ for S_2, thus confining the entire unit cell parameter variation to zone 2. $S_{\max}$ has been set somewhat arbitrarily to 3000, to avoid a contribution of size broadening (larger values of $S_{\max}$ give not significantly different results). Finally a linear background is added to the calculated doublet. The thus synthesized profile is fitted to the experimentally observed one.

The fit parameters in principle are: the two constant unit cell parameters a_1 and a_2, the FWHM (=full width at half maximum = $2w_L = 2w_G$) and the mixing parameter η of the pseudo-Voigt function*, the interface positions S_1 and S_2 and the two background parameters (intercept of the ordinate and slope). Fitting was realized by minimalization of $\sum_i (I_{\mathrm{obs}} - I_{\mathrm{calc}})^2$, where I_{obs}

* $PV(2\theta) = I_0[L(2\theta) + G(2\theta)]$ with Lorentzian component $L(2\theta) = \eta \frac{1}{1+C_L(2\theta-2\theta_0)^2}$, where $C_L = \frac{1}{w_L^2}$, and with Gaussian component $G(2\theta) = (1-\eta)\exp[-C_G(2\theta-2\theta_0)^2]$, where $C_G = \frac{\ln 2}{w_G^2}$ (w_L, w_G = FWHM of $L(2\theta)$ and $G(2\theta)$ respectively and η = mixing parameter) and with I_0 as a constant.

Table 4.1.: The unit cell parameter, *a*, of the sample determined using the Guinier technique. The boron content has been calculated using the dependence of *a* on boron content as given in Ref. [50].

	start	remixed
unit cell parameter, *a* (nm)	0.39346(7)	0.39332(2)
mole fraction, x_B	0.055	0.054

and I_{calc} are the observed and the calculated intensities, respectively, by using the Levenberg-Marquardt method [77].

Three possibilities are distinguished to simulate the experimentally determined X-ray diffraction-line profiles:

1. The boron-rich and boron-poor product phases diffract coherently with the matrix, *i.e.* the intensity in Eq. 4.2 is calculated by performing the summation over k according to the range $1 \leq k \leq S_{max}$ (cf. Fig. 4.1) and then convoluting with the instrumental broadening function $PV(2\theta)$:
$$I_{exp}(2\theta) = I(2\theta, 1 \leq k \leq S_{max}) \otimes PV(2\theta). \tag{4.3}$$

2. The boron-rich and boron-poor product phases and the matrix diffract incoherently, *i.e.* (cf. Fig. 4.1):
$$\begin{aligned} I_{exp}(2\theta) = \quad & I(2\theta, 1 \leq k \leq S_1) \otimes PV(2\theta) + I(2\theta, (S_1+1) \leq k \leq S_2) \otimes PV(2\theta) \\ & + I(2\theta, (S_2+1) \leq k \leq S_{max}) \otimes PV(2\theta) \end{aligned} \tag{4.4}$$

3. Either the boron-rich phase precipitates out of the matrix which impoverishes (ultimately becoming the boron-poor phase) or the boron-poor phase precipitates out of the matrix which enriches (ultimately becoming the boron-rich phase). In this case the precipitating phase could be considered as diffracting incoherently with the remaining enriched or impoverished matrix, *i.e.* (assuming that the boron-poor phase precipitates):
$$I_{exp}(2\theta) = I(2\theta, 1 \leq k \leq S_1) \otimes PV(2\theta) + I(2\theta, (S_1+1) \leq k \leq S_{max}) \otimes PV(2\theta) \tag{4.5}$$

4.3. Experimental

The Pd-B alloys were prepared from palladium (99.9 wt.%; Heraeus) and boron (99.5 wt.%; Johnson Matthey) by arc melting under argon (550 hPa, 99.999 vol. %; Messer Griesheim). The weight of the samples was measured before and after alloying; no significant differences

were observed. The homogeneity of the as cast bulk alloys was checked by means of X-ray diffraction.

The boron content of the alloy was determined using the dependence of the unit cell parameter on the boron content [50]. For the unit cell parameter measurements by means of X-ray diffraction analysis the bulk alloys were filed. The filings were put in quartz capsules, which were flushed with argon, then evacuated and annealed at 1073 K for 1 min. to remove internal stress due to the filing procedure, and subsequently water quenched to avoid decomposition phenomena. Powder diffraction patterns were recorded at room temperature in a Guinier transmission camera (Enraf-Nonius FR552) using Mo$K\alpha_1$ radiation (λ = 0.070930 nm). Germanium (99.9999 wt. %; Johnson Matthey, unit cell parameter a = 0.56574 nm [23]) was used as an internal standard. Single coated CEA Reflex 15 film was used for the Guinier patterns. The positions of the diffraction lines in the Guinier patterns were determinated using a Line-Scanner LS 20 (KEJ Instruments). Unit cell parameters were refined by least squares fitting of Bragg's equation to the positions of the diffraction lines in the range $17^\circ < 2\theta < 56^\circ$.

The filings for the long time heating were prepared in the same way. The samples were heat treated at 628 K for 3.5 days to nearly 48 days and then subsequently water quenched. For the transmission electron microscopy (TEM) investigations bulk material was prepared in the same way as the powder (filing) and heat treated for nearly 70 days.

For decomposition reversion (redissolution), the filings in fully decomposed state (after annealing for 33.6 days at 628 K) were annealed for 1 hour at 923 K and then quenched into water.

The unit cell parameters and thus the boron contents were determined using the Guinier technique for the initial solid solution and after redissolution have been given in Table 4.1. Note that the value for the boron content after redissolution does not differ significantly from the initial value.

The X-ray diffraction analysis of the long time heated samples was performed with a Philips X'Pert diffractometer equipped with a Cu tube and a graphite monochromator in the diffracted beam to select Cu$K\alpha$ radiation and applying Bragg-Brentano geometry. The diffracted intensity was recorded in the range of 38° to 110° 2θ with a step size of 0.01° 2θ and a counting time per step in the range of 20 to 110 seconds. The divergence slit width was 0.25° and the receiving slit width was 0.1 mm. To measure the line broadening due to the wavelength distribution and the instrumental aberrations a LaB_6 standard specimen (NIST reference standard material 660a) was used.

For TEM investigations the sample (bulk) was thinned using conventional Ar^+ ion-milling to obtain an electron transparent foil. To avoid sample heating during the milling the sample was cooled using liquid nitrogen. For the TEM investigations a JEM 2000 FX electron microscope operating at an acceleration voltage of 200 kV was used.

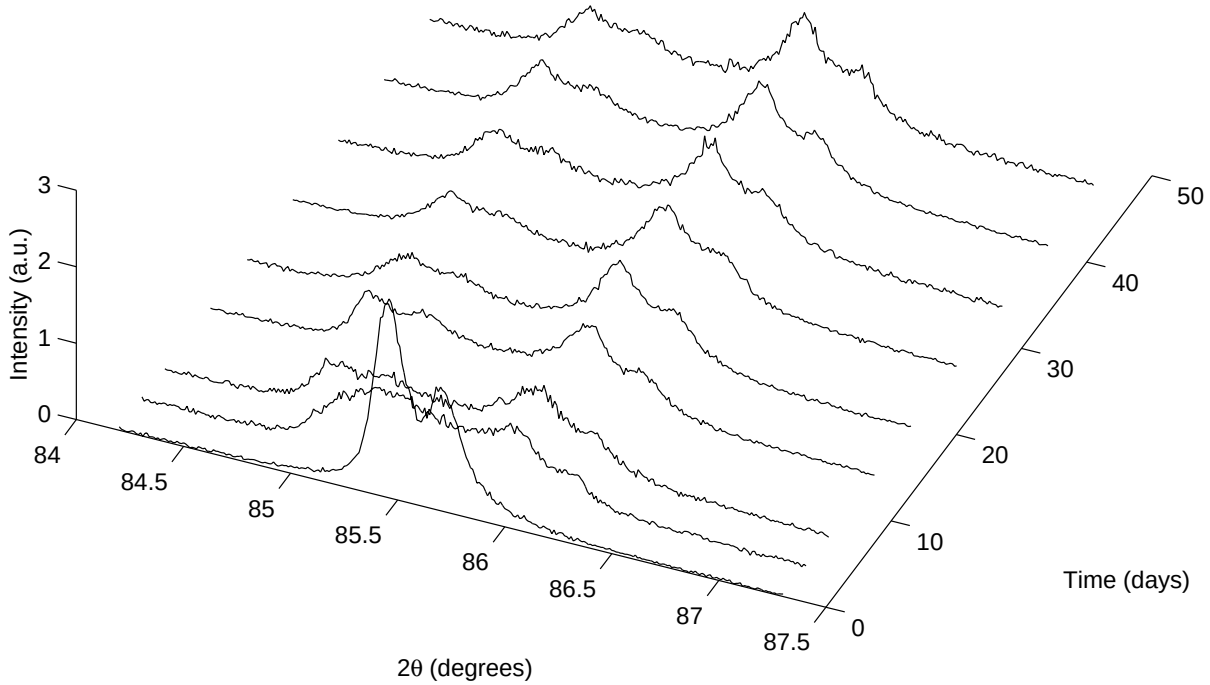

Figure 4.2.: Diffraction profiles of the 222 peak of $Pd_{94}B_6$ as a function of annealing time. The first profile ($t = 0$) is the diffraction peak of the homogeneous interstitial solid solution (sample annealed at 1073 K for 1 minute); various stage of decomposition are shown for annealing at 628 K for the different times.

4.4. Observations

The decomposition of the $Pd_{94}B_6$ solid solution upon annealing was exhibited by X-ray diffraction analysis. The 222 diffraction-line profiles are shown for various annealing times at 628 K in Fig. 4.2. At $t = 0$ only one diffraction peak is observable, indicative of the homogeneous, supersaturated solid solution. Upon annealing a splitting of the diffraction peak occurs, corresponding to the development of the boron-poor phase and the boron-rich phase.

Fitting of the profiles of the decomposed samples using two conventional, splitted (*i.e.* asymmetric) pseudo-Voigt functions [78] leads to opposite and about equal asymmetries of the fitted profiles (*e.g.* asymmetry parameters of -29 and +28, respectively).

Electron diffraction patterns of the homogeneous solid solution show sharp diffraction spots (Fig. 4.3a). In contrast with this, electron diffraction patterns of the decomposed solid solution

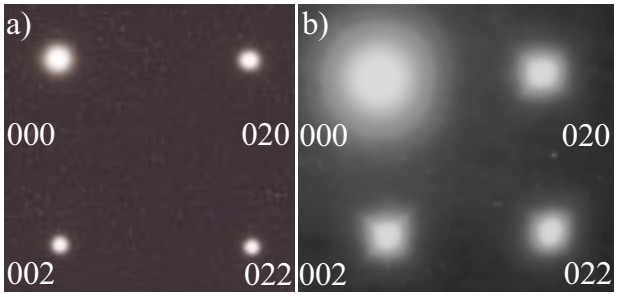

Figure 4.3.: a) Electron diffraction pattern of a homogeneous $Pd_{94}B_6$ solid solution ([100] zone axis). The sample was prepared by annealing the decomposed solid solution (right figure) at 923 K for 1 hour.
b) Electron diffraction pattern of a decomposed $Pd_{94}B_6$ solid solution after annealing at 628 K for 70 days ([100] zone axis).

show broadened spots and (short) diffuse streaks in $<011>$ directions (cf. Fig. 4.3b; [100] zone axis).

The bright field electron microscope image of the homogeneous solid solution (after annealing of the decomposed sample at 923 K for one hour and subsequent quenching into water) shows an overall homogeneous contrast (Fig. 4.4). Further, dislocations are present, apparently due to quenching after the solution annealing. The dislocation density, as measured from the micrographs, is about $2 \cdot 10^{13}$ m^{-2}, which is significantly larger than the dislocation density for well annealed metals [79]. After decomposition annealing the bright field electron microscope image shows a strongly inhomogeneous contrast indicative of precipitation-strain variation on a length scale of the order 10 nm (Fig. 4.5).

4.5. Fitting of X-ray diffraction-line profiles

Line-profile fitting has been carried out for all three cases of line-profile simulation indicated in section 4.2 (Eqs. 4.3 - 4.5). The results as expressed in the unit cell parameters of the (developing) boron-poor and boron-rich phases show that, within the experimental accuracy, (i) same results are obtained at a certain stage of decomposition from all fitted line profiles (111, 002, 022, 113, 222, 004) and (ii) insignificant differences occur for the three cases of line-profile simulation. Thus, the unit cell parameters for the boron-poor and boron-rich phases, as given by the average derived from all reflections considered, is shown in Fig. 4.7. It follows that the unit cell parameter of the boron-poor phase is the same for all stages of decomposition, whereas the unit cell parameter of the boron-rich phase increases upon increasing annealing time.

This leads to the following description of the precipitation process: the boron-poor phase

Figure 4.4.: Bright field TEM image of the homogeneous solid solution of $Pd_{94}B_6$ after annealing of the bulk material at 628 K for 70 days (=demixing, cf. Fig. 4.5) and subsequent annealing at 973 K for 1 hour. Hereby a homogeneous solid solution is established.

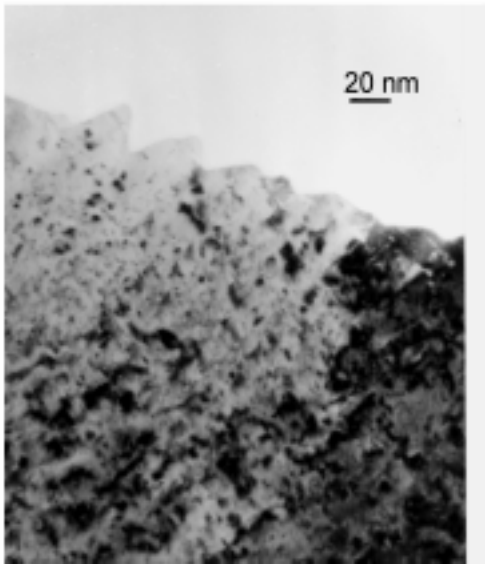

Figure 4.5.: Bright field TEM image of the decomposed state of $Pd_{94}B_6$ after annealing of the bulk material at 628 K for 70 days.

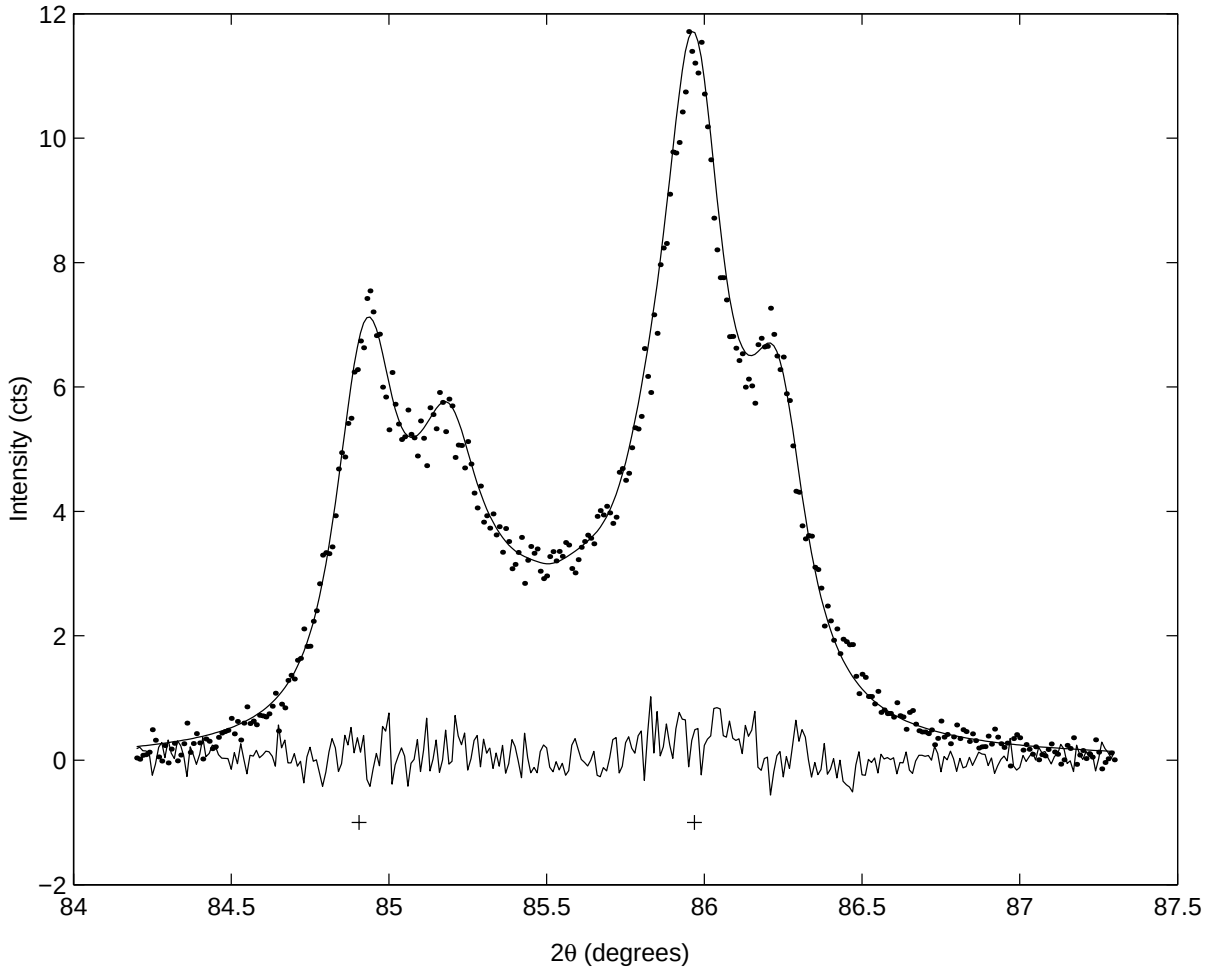

Figure 4.6.: Observed points (•), refined pattern (−) and difference pattern (−) of the 222 diffraction peak of the decomposed Pd(B) solid solution after annealing at 628 K for 40.6 days. The positions of the two main reflections have been marked (+).

precipitates from the start of annealing, leaving a matrix gradually enriching in boron until the equilibrium value; *i.e.* of the boron-rich phase, has been reached. It will be seen that results derived from the fitting support this interpretation (see section 4.6).

Hence the definitive line-profile simulations have been performed according to case 3 (cf. section 4.2; Eq. 4.5). The results are discussed in the following sections.

An example of fitting is shown in Fig. 4.6 for the 222 diffraction peak of $Pd_{94}B_6$ after annealing at 628 K for 40.6 days. The match between the experimental data and the calculated profile is good. Only the line profile determined for an early stage of decomposition (after an annealing time of 3.5 days) could not be fitted very well; the corresponding results have not been considered in the discussion (cf. Fig. 4.7).

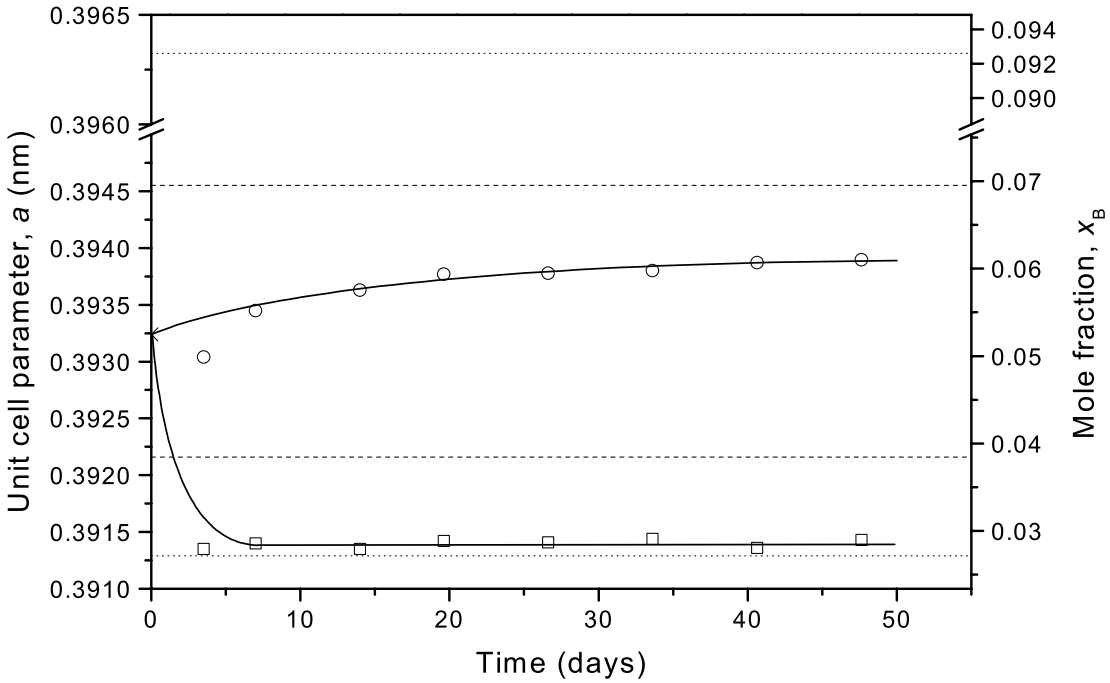

Figure 4.7.: The unit cell parameter, a, determined using all measured diffraction peaks, and the boron content, expressed at the mole fraction x_B, of the decomposed state, as a function of annealing time at 628 K (boron-poor phase = □, boron-rich phase = ◯). The boron content is calculated using the dependence of the unit cell parameter on the boron content [50]. The unit cell parameter of the initial homogeneous solid solution as determined using the diffractometer data is also shown (×). The dotted lines represent the experimental determined boron contents of the miscibility gap as reported by [13]; the dashed lines represent the prediction using the quasi-chemical approximation [13]. For the results at $t = 3.5$ days, see section 4.5.

4.6. Phase composition and amount

The unit cell parameter (linearly related to the boron content [50]) is given in Fig. 4.7 as a function of annealing time for both the precipitating boron-poor phase and the remaining matrix, enriching in boron (because of the compositional variation in the remaining matrix the average unit cell parameter of zones 2 and 3 has been given). After an annealing time of $t \approx 25$ days the boron content of (also) the remaining matrix (boron-rich phase) is practically constant.

The boron content of the boron-poor phase matches well with experimental data reported earlier for the miscibility gap at 628 K (cf. Fig. 4.7; [13]). The boron content of the boron-rich phase differs significantly from the literature data presented in [13] (this work: $x_B = 0.061$, literature data [13]: $x_B \cong 0.093$). On the other hand, a theoretical prediction of the miscibility

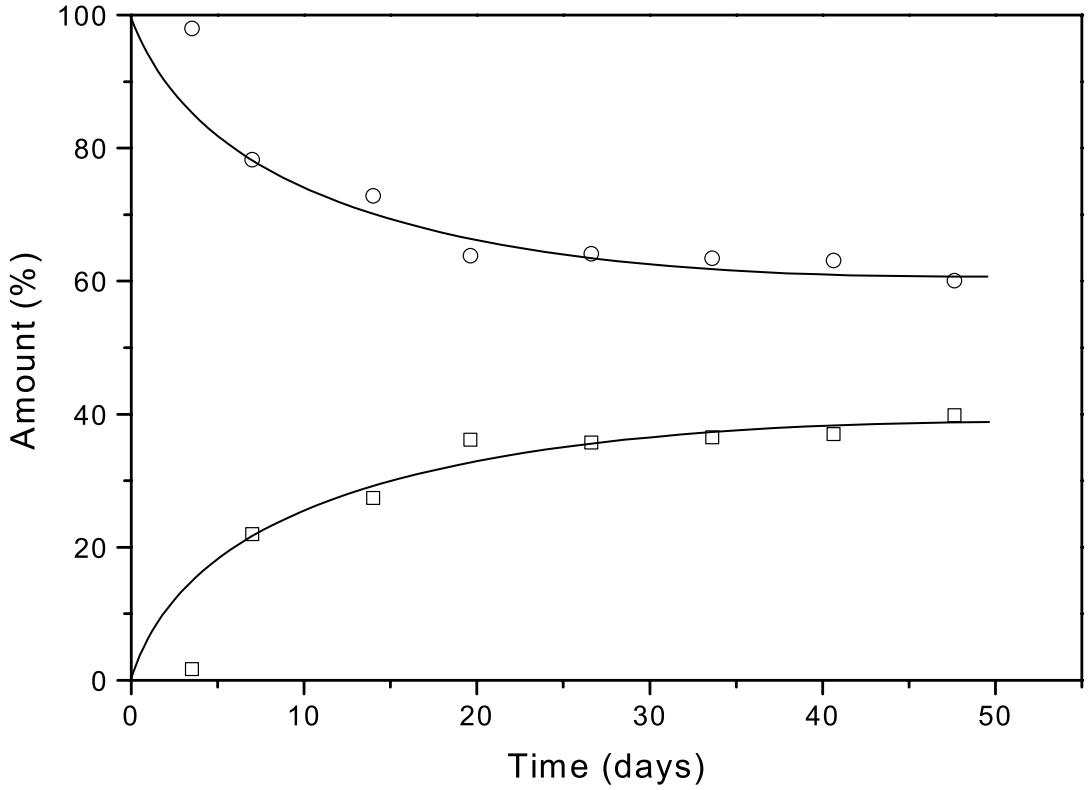

Figure 4.8.: The determined amount of the decomposed phases as a function of time (boron-poor phase = □, boron-rich phase = ◯). For the results at $t = 3.5$ days see section 4.5.

gap has been obtained from an evaluation of activity measurements using the quasi-chemical approximation with as result a composition range of $0.038 < x_B < 0.070$ for the miscibility gap (at T = 628 K) [13]. The width of this theoretical miscibility gap agrees well with the experimental width determined in this work, but the theoretical compositions for the equilibrium phases are somewhat higher than the experimental data (see Fig. 4.7).

The amounts of both phases as determined by the line-profile fitting have been given in Fig. 4.8. Upon decomposition the amount of boron-poor phase (of constant composition; see above) increases, whereas the amount of matrix enriching in boron decreases. Beyond about 25 days of annealing the amounts of both phases do not change further significantly, indicating that the equilibrium situation has been reached.

A way to check the consistency of the phase-composition and phase-amount data, as determined by the line-profile fitting, is as follows. On the basis of the data from the line-profile fitting for phase composition and phase amount, the overall composition of the specimen can

be calculated. Doing this for every stage of the decomposition for which line-profile measurements were performed (cf Fig. 4.8), it followed that i) practically the same overall composition was calculated for every decomposition stage and ii) the calculated overall composition differed only about 0.4 at. % from the initially measured overall value, which difference is considered acceptable in view of the simple structure model used in the fitting. Results i) and ii) indicate that the fit results for phase composition and phase amount are compatible.

4.7. Microstrain

The instrumental profile as defined in this paper (cf. section 4.2) does not necessarily only contain the broadening due to the wavelength distribution and the instrumental aberrations. Because for the line-profile simulation only the compositional variation has been considered as structural line broadening (cf. section 4.2), it follows that possible microstrain broadening and domain size broadening are incorporated in the 'instrumental' profile determined by the line-profile fitting. The real instrumental profile can be determined using a standard specimen (LaB_6, cf. section 4.3; this standard material gives rise to negligible size and microstrain broadening). The contribution to the FWHM values of the "instrumental" profiles due to the true instrumental broadening were eliminated by straightforward subtraction of the corresponding FWHM values determined by interpolation, at 2θ values corresponding to the measured Pd(B) reflections, between measured FWHM data for the LaB_6 standard specimen; this subtraction of FWHM values holds exactly for profiles of Lorentzian shape. Then, values for the integrated breadth, β, were obtained from the thus corrected FWHM values by using the relation between FWHM and β for Lorentzian profiles: $\beta = \mathrm{FWHM} \cdot \pi/2$.

Analysis of line broadening can be performed on the basis of the Williamson-Hall analysis [14]. If it is assumed that the various components of structural line broadening can be approximated with Lorentzian functions, the following relation holds between the integral breadth, β, of an only structurally broadened reflection and the size, D and the microstrain ε (cf. Ref. [14, 80]):

$$\beta\frac{\cos(\theta)}{\lambda} = \frac{1}{D} + 2\varepsilon\frac{2\sin(\theta)}{\lambda} \tag{4.6}$$

with β expressed in radians 2θ. Hence, a straight line behaviour should be observed in a plot of $\beta\cos(\theta)/\lambda$ *vs.* $2\sin(\theta)/\lambda$. Now consider Fig. 4.9 which shows such plots as obtained for the Pd-B alloy considered both as homogeneous solid solution and in the fully decomposed state (after an annealing time of 33.6 days). Indeed, straight lines, as predicted by Eq. 4.6, are observed.

These results can be discussed as follows:

The homogeneous Pd-B alloy exhibits distinct microstrain broadening (the slope in the

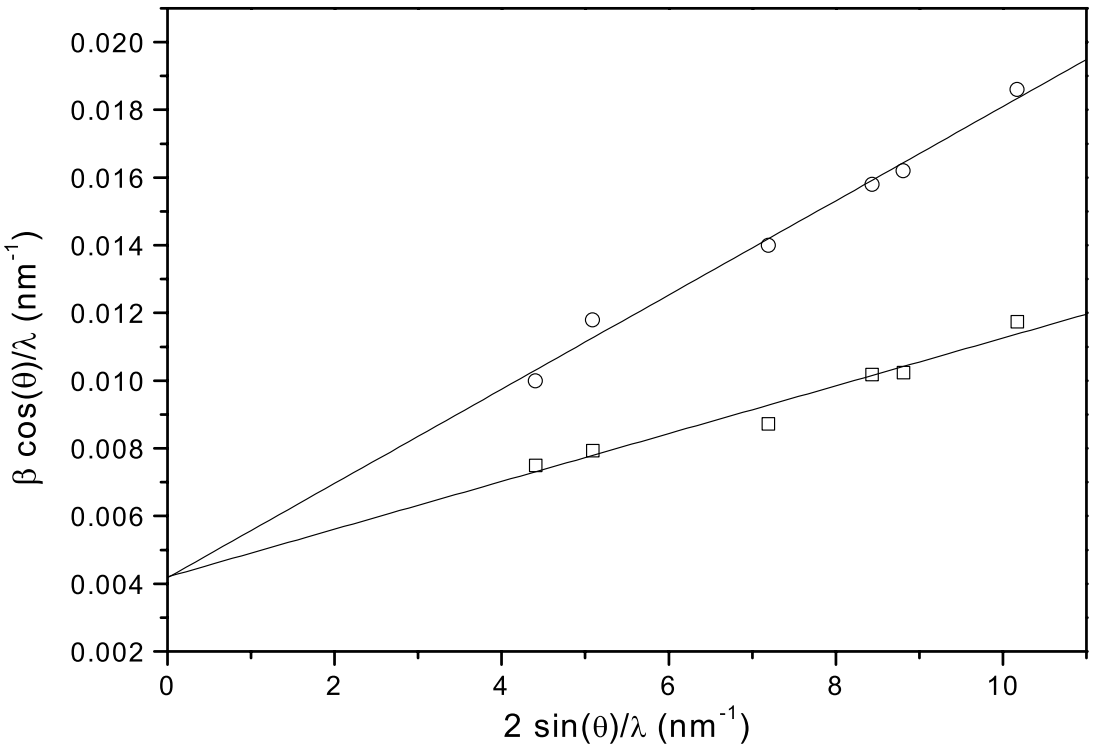

Figure 4.9.: Williamson-Hall plots for decomposed state (after annealing for 33.6 days) = ◯, and for the homogeneous, quenched solid solution = □.

Williamson-Hall plot for this alloy is larger than zero). This is ascribed to the dislocations introduced by quenching after the homogenization (cf. section 4.4 and Fig. 4.4). Adopting the approach in Ref. [81] the following estimate can be obtained for the dislocation density, ρ_d, from the size and microstrain values:

$$\rho_d = \frac{2\sqrt{3} < e^2 >^{1/2}}{Db} = 1.3 \cdot 10^{13}\ \mathrm{m}^{-2}$$

with $b =$ norm of the Burgers vector of the dislocations (taken as $b = a/\sqrt{2}$ for *fcc*-material) and $< e^2 >^{1/2}$ = mean square strain approximated with ε [80]. This result well agrees with the dislocation density value as estimated from a transmission electron micrograph of the homogeneous Pd-B alloy after quenching (cf. section 4.4).

No (additional) size broadening is caused by the decomposition, because the intercepts cut from the ordinate by the lines of the homogenized and decomposed alloys are the same. Furthermore, the size broadening as determined from the intercept is relatively large (size of $\sim$ 240 nm).

The decomposition of the Pd-B alloy introduces additional microstrain (cf. slope of Williamson-Hall plot for the fully decomposed stage with the one of the homogeneous state in Fig. 4.9). Comparing the slopes of the straight lines in Fig. 4.9 it follows that the decomposition about doubles the microstrain in the Pd-B alloy:

$$\varepsilon(\text{homogeneous alloy}) = 3.6 \cdot 10^{-4}; \qquad \varepsilon(\text{decomposed alloy}) = 7.2 \cdot 10^{-4}.$$

Also the diffraction-contrast variations observed in the transmission electron microscope micrographs indicate development of pronounced microstrain upon decomposition (cf. section 4.4).

4.8. Conclusions

- A simple model for the spatial unit cell parameter variation in a decomposing Pd(B) solid solution allows accurate fitting of simulated X-ray diffraction-line profiles to measured ones.
- The *fcc* Pd(B) solid solution decomposed in a boron-poor *fcc* Pd(B) phase and a boron-rich *fcc* Pd(B) phase, such that a boron-poor phase of constant composition precipitates in a matrix enriching in boron and thereby becoming the boron-rich phase.
- The range of the miscibility gap at 628 K was determined as $0.028 < x_B < 0.061$.
- The initial homogeneous alloy exhibited distinct microstrain broadening due to dislocations. The dislocation densities determined from the X-ray diffraction-line broadening and transmission electron microscopy agree well.
- Decomposition of the Pd(B) solid solution leads to development of pronounced microstrain, as evidenced by the occurrence of diffraction line broadening: as compared to the initial homogeneous, quenched alloy, the amount of microstrain was about doubled upon decomposition at 628 K.

Acknowledgments: The authors wish to thank Dr. P. Lamparter for useful discussions on line-profile simulation and Mr. P. Kopold and Dr. W. Sigle for assistance with the TEM investigations.

Chapter 5

Simultaneous determination of specimen temperature and specimen displacement in high temperature X-ray diffractometry applying Bragg-Brentano geometry

M. Beck and E.J. Mittemeijer

Abstract: Temperature uncertainty and unknown specimen displacement are the most severe errors in high temperature X-ray diffractometry, in particular when using a strip heater mounted on a Bragg-Brentano goniometer. A method is presented which enables the simultaneous determination of the specimen displacement and the temperature of the sample. The method splits the determination of the aberrations in two steps: at room temperature and at elevated temperature. It is based on the use of a reference material as internal standard. An experimental example applying the method to a specific material is given, which shows that the method provides correct data.

5.1. Introduction

In situ high temperature X-ray powder diffraction is a very useful tool for investigation of the behaviour of (crystalline) materials at non-ambient temperatures. To arrive at correct values of the unit cell parameters, the positions of the Bragg reflections, characterized by the corresponding diffraction angles 2θ, have to be determined accurately. For an overview on aberrations affecting the diffraction peak positions, see [82–84].

The largest errors in 2θ are the zero shift and the specimen displacement. The zero shift involves a (constant) shift of the peak positions over the whole 2θ range. The specimen displacement affects the peak position proportional with $\cos\theta$ [82] (cf. Eq. 5.1, below).

For small values of 2θ *the change of* the specimen displacement induced peak shift as function of 2θ is small (for $0 < 2\theta < 90^\circ$ a variation of about 30 % occurs). Therefore it is evident that the peak shift induced by the specimen displacement can hardly be distinguished from the zero shift for low diffraction angles [85]. In this case, these two errors have been considered as one combined error causing a constant shift of the peak positions like a 'new' zero shift (approximation for the specimen displacement: $\cos\theta \simeq 1$, cf. Eq. 5.1).

If the zero shift is the only aberration, it can be determined and corrected without internal standard using the reflection-pair method [86–88]. If both zero shift and specimen displacement occur, they can be measured at constant temperature applying standard materials of which the true peak positions are known [89]. It can be assumed safely that the zero shift does not change when the specimen on the heating stage in the diffractometer is exposed to various temperatures. This does not hold for the specimen displacement: for example, many heating stages consist of a heating chamber equipped with a strip heater [90]. Upon heating, the strip will expand. The elongation in the direction of the filament can be more or less compensated by means of applying prestressing of the heating filament. However, the surface of the filament, which may be in the ideal position at room temperature (*i.e.* specimen displacement then is nil), will in general not stay in this ideal position upon heating; heating leads to thermal expansion possibly in association with stress development and the specimen surface can move upward or downward. Specimen displacement is regarded as one of the most serious sources of error in the 2θ values [82].

Furthermore, the assignment of the correct temperature value to the data recorded at elevated temperature can be problematic; the temperature of the filament is traced by a thermocouple positioned normally on the bottom side of the strip heater. The temperature at this location can differ significantly from the temperature of the specimen [91]. Further, this difference is temperature dependent.

Hence, generally it is impossible to interpret shift of peak positions upon heating straightforwardly in terms of the temperature change imposed, not only because the true temperature

of the specimen is unknown, but also because at the same time an also unknown specimen displacement occurs.

A widely used method for calibration of the sample temperature in heating chambers is the use of external standards by observing polymorphic phase transformations [92]. Then, during the measurement, the specimen displacement is determined by the reflections of the heating strip. A large problem of this determination of temperature and specimen displacement is that the sample has to be mounted exactly in the same way as the external standard specimen. Small changes in thickness or in package density of the sample lead to a not negligible temperature error [93].

This paper presents a method which enables a *simultaneous* determination of both the specimen displacement and the temperature of the sample. It is demonstrated experimentally, by application to specific reference materials upon heating, that the method provides correct data.

5.2. The principle of the method

The method utilizes peaks recorded from a reference material that serves as an internal standard. Requirements for the reference material used as internal standard are: it should be inert in the atmosphere used and not react with sample material and the heating strip. Further its thermal expansion coefficient has to be known very well. It is of advantage if the thermal expansion coefficient is large, because this leads to a stronger temperature dependence of the peak positions.

The method is subdivided in two steps:

(i) In the first step, the zero shift and the specimen displacement at room temperature are determined from peak position measurements performed on the internal standard material, as follows:

The specimen displacement, s, leads to a peak shift $\Delta(2\theta)_{sd}$ (rad) depending on 2θ given by

$$\Delta(2\theta)_{sd} = -\frac{2s}{R}\cos\theta, \tag{5.1}$$

where R is the goniometer radius and s is positive for upward displacement of the specimen surface [82].

Then the difference between the true peak position, $2\theta_t$, and the observed one, $2\theta_o$, can be expressed as

$$\Delta(2\theta) = 2\theta_t - 2\theta_o = -\frac{2s}{R}\cos(\theta_t) + \Delta(2\theta)_{zs}, \tag{5.2}$$

where $\Delta(2\theta)_{zs}$ is the zero shift. A plot of $\Delta(2\theta)$ *vs.* $\cos(\theta_t)$ leads to a straight line and thus the specimen displacement and the zero shift are determined separately and independently from

each other from the slope and intercept of the straight line.
(ii) In the second step, the specimen displacement and the temperature of the sample are determined form the peak position measurements performed on the internal standard at elevated temperature, as follows:

At elevated temperature, the theoretical, true positions of the peaks recorded from the internal standard (here taken as a cubic substance; this is not a limitation) can be calculated using Bragg's law and the unit cell parameter, a, at room temperature, if the thermal expansion coefficient is known. Then the relation between the true peak position, $2\theta_t$, and the expected peak position (*e.g.* the peak position affected by specimen displacement and zero shift), $2\theta_{ex}$, is given by

$$\begin{aligned} 2\theta_{ex}(T) &= 2\theta_t(T) - \Delta(2\theta)_{sd}(T) - \Delta(2\theta)_{zs} \\ &= 2\arcsin\left(\tfrac{\lambda}{2}\tfrac{\sqrt{h^2+k^2+l^2}}{a(T)}\right) + \tfrac{2s}{R}\left[1 - \left(\tfrac{\lambda}{2}\tfrac{\sqrt{h^2+k^2+l^2}}{a(T)}\right)^2\right]^{1/2} - \Delta(2\theta)_{zs}. \end{aligned} \tag{5.3}$$

The dependence of the unit cell parameter a on temperature for pure elements can be described as

$$a(T) = a_0 + \Delta a(T);\ \Delta a(T) = a_0 \sum_{i=1}^{3} \alpha_i (T - T_0)^i \tag{5.4}$$

where a_0 = unit cell parameter of the internal standard at the reference temperature T_0 and α_i = the thermal expansion coefficient (see data pool [94, 95]).

The zero shift in Eq. 5.3 is known from the measurement at room temperature (step (i)). The values of s and T now can be determine from the observed values for the peak positions by minimalization of $\sum_i (2\theta_{ex,i} - 2\theta_{o,i})^2$, where $2\theta_{ex,i}$ is given by Eq. 5.3 (the subscript i has been added to distinguish the i^{th} component in the series of peak positions considered).

5.3. Application of the method

5.3.1. Experimental

As internal standard material germanium was used (99.9999 wt. %; Johnson Matthey; unit cell parameter a = 0.56574 nm at 298 K [23]; for thermal expansion coefficients see Table 5.1). As a model material tungsten was used (99.9 wt. %; Johnson Matthey; a = 0.31648 nm at 298 K [96]; for thermal expansion coefficients; see Table 5.1). The high-temperature X-ray diffraction patterns were recorded from 26 to 135 °2θ with a step size of 0.02 °2θ using Cu$K\alpha$ radiation and a Philips X'Pert $\theta - \theta$ diffractometer with Bragg-Brentano geometry (goniometer

Table 5.1.: Thermal expansion coefficients of the internal standard (Ge) and the material investigated (W) [94]. For definition of α_1, α_2 and α_3, see Eq. 5.4.

	α_1	α_2	α_3	
Ge	5.790×10^{-4}	1.768×10^{-7}	-4.562×10^{-11}	$293\ \mathrm{K} < T < 1200\ \mathrm{K}$
W	4.266×10^{-4}	8.479×10^{-8}	-1.974×10^{-11}	$293\ \mathrm{K} < T < 1395\ \mathrm{K}$

radius $R = 230$ mm). The time per step was between 8 and 20 sec. An automatic divergence slit was used with a radiated sample-length of 4 mm; the incident beam mask was 5 mm. A heating stage Anton Paar HTK 2000 was installed on the diffractometer. The heating filament consisted of tantalum. The temperature was controlled using a Pt-10%RhPt thermocouple, which was welded on the rear side of the Ta strip. For the high-temperature measurements, the heating chamber was evacuated ($\approx 10^{-2}$ Pa). Before and during the measurements the heating chamber was flushed with helium (99.999 vol. %, Messer-Griesheim). Then, the pressure in the chamber was approximately 10 hPa higher that the ambient pressure. The standard as well as the model material was pulverized, mixed and put directly on the heating strip. The measured peak profiles were fitted with Peason VII profiles, using Philips Profit 1.0 software. This program fits a linear background and peaks consisting of $K\alpha_1$ and $K\alpha_2$ peaks with a fixed ratio (0.5) and wavelength difference.

5.3.2. Results and discussion

The purpose is to determine the unit cell parameter of tungsten to a high degree of accuracy from the peak-position measurements at elevated temperature, after determination of the specimen displacement and the temperature using peak positions recorded from the internal standard germanium. Because for tungsten the unit cell parameter and the thermal expansion coefficients are known very well (cf. Tables 5.1 and 5.2; [94, 96]), the experimental results can be well compared with theoretical, expected values.

The determination of the zero shift and the specimen displacement at room temperature using the peak positions of germanium is presented in Fig. 5.1 (step (i), see above). The resulting zero shift in this case is $\Delta(2\theta)_{zs} = 0.018^\circ$ (part cut from the ordinate by the straight line in Fig. 5.1); the specimen displacement is $s = -14$ μm (from the slope of the straight line in Fig. 5.1). Because of the low intensity of the germanium 440 diffraction peak at room temperature and its further decrease for increasing temperature, this diffraction peak is not considered in the analysis.

In the second step the measured peak positions of germanium at elevated temperature were used to determine both the specimen displacement at the specimen temperature concerned and

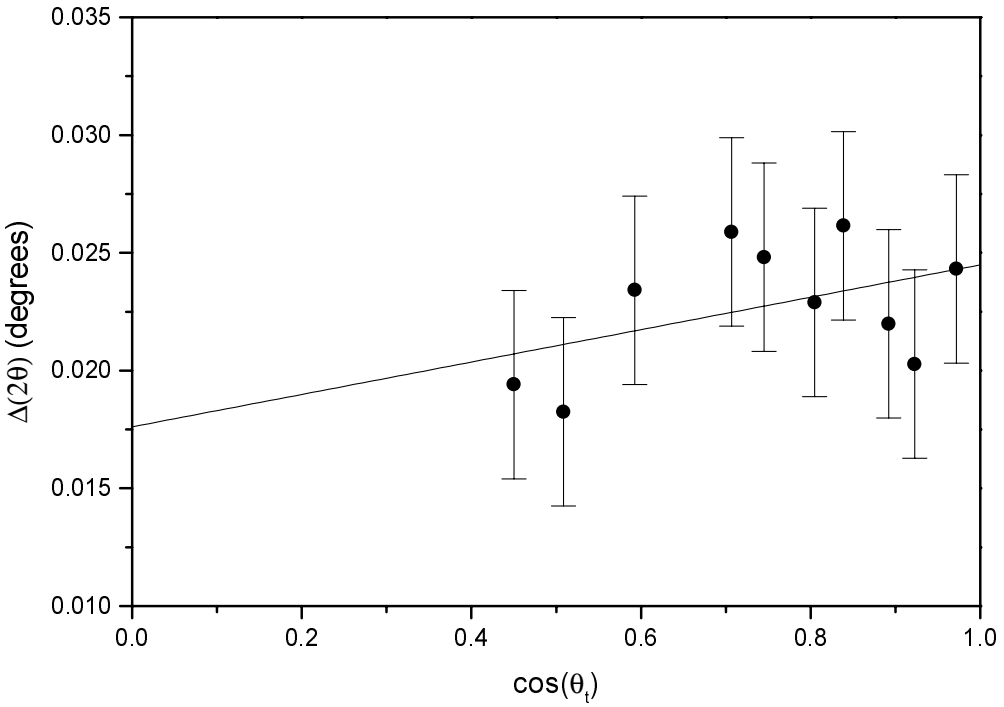

Figure 5.1.: The difference $\Delta(2\theta) = 2\theta_t - 2\theta_o$ of the theoretical, true peak position, $2\theta_t$, and the observed one, $2\theta_o$, of germanium as a function of $\cos(\theta_t)$ at room temperature (299 K; cf. Eq. 5.2). The intercept corresponds to the zero shift, $\Delta(2\theta)_{zs}$, and the specimen displacement, s is represented by the slope of the straight line (results of this example: $\Delta(2\theta)_{zs} = 0.018°$, $s = -12$ μm).

the specimen temperature itself, as described above. The results are shown in Figs. 5.2 and 5.3.

The determined, resulting differences of the actual temperature of the specimen, T_s, and the temperature as indicated by the thermocouple, T_{tc}, are shown as a function of T_{tc} for two different measurement series* in Fig. 5.2. An appreciable difference between the true specimen temperature and the thermocouple indication is observed, that in particular increases for temperatures higher than about 550 K.

The temperature discrepancy is due to a few errors which superimpose. Firstly, the thermocouple is welded in an area of length approximately 3 mm in the direction of the goniometer axes and a width of approximately 1 mm in the direction perpendicular to the goniometer axis. Hence the temperature measured by the thermocouple is an average temperature of (only) this area, whereas the area observed in the diffraction experiment has a length in the direction of the

*A new mixture of the same internal standard and the sample were made for each measurement series. The measurements of both series were performed under the same conditions.

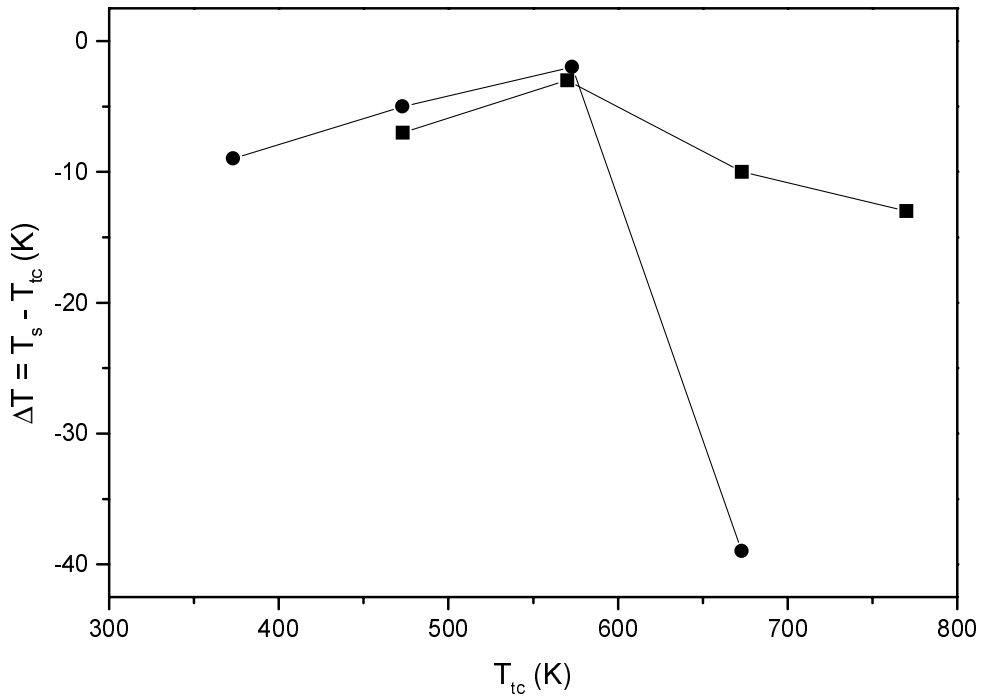

Figure 5.2.: The difference of the actual temperature of specimen, T_s, an the temperature as indicated by the thermocouple, T_{tc}, as determined for two different measurement series.

goniometer axis of 5 mm and a width of 4 mm perpendicular to the goniometer axis (a variable (2θ dependent) slit width was applied). Additionally the negative temperature gradient increases near the edge of the heating strip [97]. A larger temperature gradient is expected in that part of the area observed in the diffraction experiment that is not 'seen' by the thermocouple. Also, the temperature profile in the length of the heating strip narrows with increasing temperature.

Secondly, a pulverized sample powder was put on the heating strip. For a powder specimen the thermal contact between the heating strip and the sample can obviously be far from ideal [91]. Thus, the temperature difference between the heating strip and the sample depends on the way of preparation of the powder sample and the surrounding atmosphere [93]: a loosely packed powder on the heating strip could give rise to a relatively large temperature discrepancy, whereas for a closely packed powder sample the temperature difference can be small. These effects can be in particular pronounced if temperature calibration is performed using external standards by observing polymorphic phase transformations, as in Ref. [92].

The (change of the) specimen displacement determined from the peak positions of germanium is shown as function of the temperature indicated by the thermocouple, T_{tc}, for the

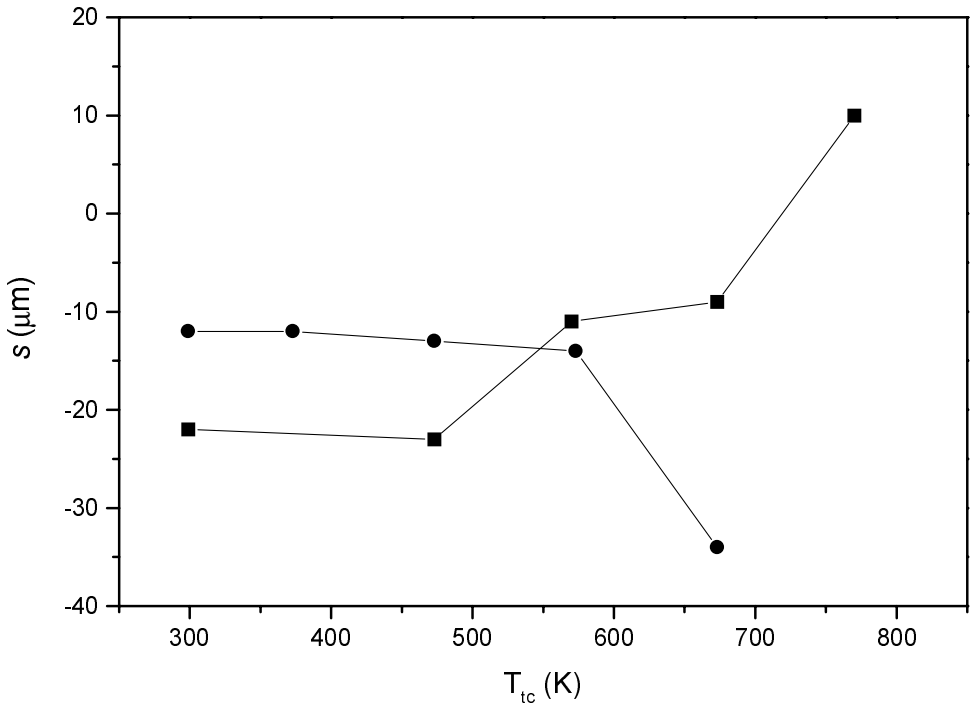

Figure 5.3.: The specimen displacement, *s*, as function of the temperature indicated by the thermocouple, T_{tc}, as determined applying the method described, for two different measurement series.

two measurement series in Fig. 5.3. Clearly, the specimen displacement depends strongly on temperature; in particular for temperatures higher than about 550 K. Further, the specimen displacement behaviour is not reproducible: see the results for both measurement series.

The thermal expansion of the fastened heating strip leads to an arch-type deformation of the heating strip in the length direction of the heating strip. Further, the temperature gradient in the width direction of the heating strip causes a strong arch-type deformation in the direction of the goniometer axis as well [98]. Thickness and packing differences of specimens will cause temperature fields in the heating strip and the sample that can vary from specimen to specimen. Thus the even opposite behaviours of specimen displacement versus temperature for different measurements series (see Fig. 5.3) maybe understood. This observation enhances the conclusion that the specimen displacement and the temperature have to be determined for each measurement series separately. Further, a relatively small thermal conductivity of the sample material can enhance heterogeneity of the temperature field of the heating strip leading to a further inhomogeneity of the resulting deformation of the heating strip [93].

Using the zero shift determined at room temperature and the specimen displacement for the

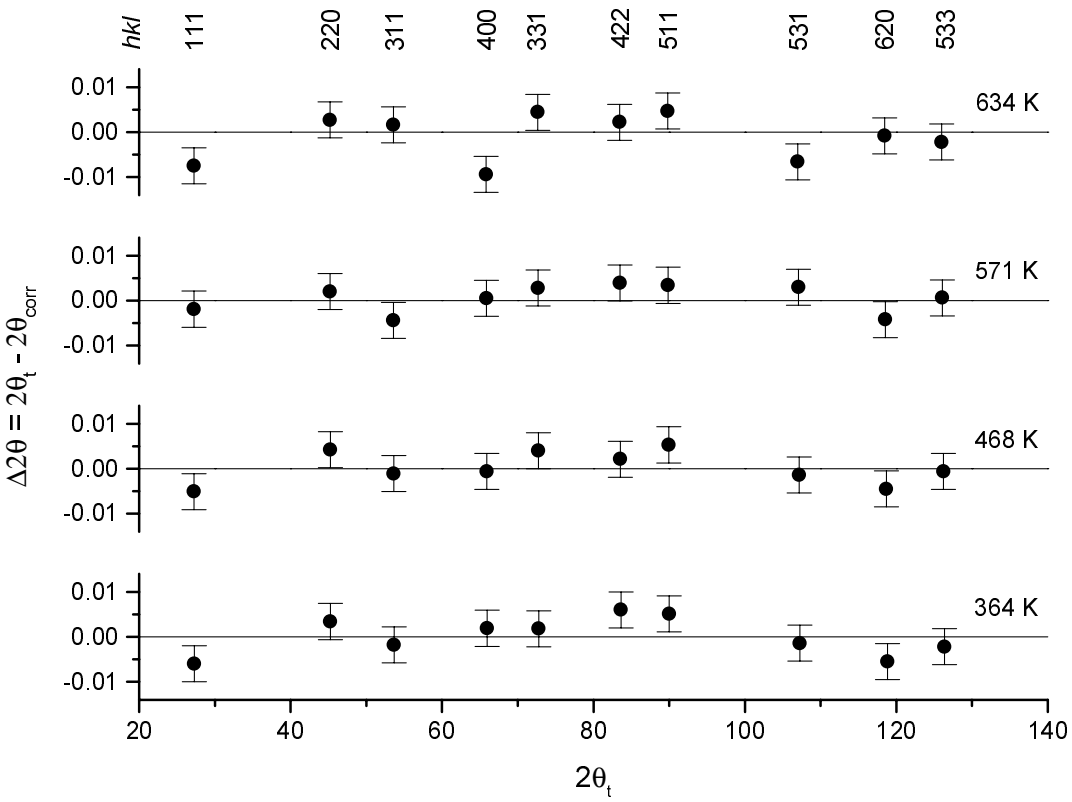

Figure 5.4.: The differences between the theoretical *hkl* peak position calculated using the unit cell parameter at room temperature and the thermal expansion coefficients, $2\theta_t$, and the measured *hkl* peak positions of tungsten after correction for zero shift and specimen displacement, $2\theta_{corr}$, for different temperatures.

specimen concerned as function of temperature, the corrected, true peak position of the sample, ($2\theta_{corr}$), can be determined for each temperature. These corrected values for the peak positions can be compared with the theoretical values for the peak positions, $2\theta_t$, as calculated using the well known unit cell parameter at room temperature and the thermal expansion coefficients as a function of temperature (cf. Tab. 5.1). The differences between the theoretical and thus corrected, experimental values for the peak positions of tungsten, $2\theta_t$ and $2\theta_{corr}$, respectively, are shown in Fig. 5.4 for some temperatures. Clearly, the differences remaining between $2\theta_t$ and $2\theta_{corr}$ are in the range of the experimental error of peak position determination (*i.e.* about one fifth of the step size employed in recording the line profiles; cf. section 5.3.1).

The unit cell parameter was refined by least squares fitting of Bragg's equation to the corrected positions of the diffraction peaks. The results have been gathered in Tab. 5.2 for various temperatures. The differences between the unit cell parameter values determined by applying the described method, a_{det}, and the theoretical values, a_t, calculated using literature values for the unit cell parameter at room temperature and the thermal expansion coefficient are negligible.

Table 5.2.: Unit cell parameter of tungsten at different temperatures: $a_t(T_s)$ calculated from literature data (cf. Tab. 5.1, [94, 96]) for the temperature of the specimen, T_s, and a_{det} determined from measured peak positions after correction by the method proposed and fitting of Bragg's law to these corrected peak positions; also the figure of merit according to [53] has been given. $\Delta T = T_s - T_{tc}$ and s is the specimen displacement determined by the method proposed in this paper.

T_{tc} (K)	T_s (K)	ΔT (K)	s (μm)	$a_t(T_s)$ (nm)	a_{det} (nm)	F_7
299			-12	0.31648	0.31648(1)	107(0.009, 7)
373	364	-9	-12	0.31657	0.31658(1)	102(0.010, 7)
473	468	-5	-13	0.31671	0.31671(1)	130(0.008, 7)
573	571	-2	-14	0.31687	0.31688(1)	166(0.006, 7)
673	634	-39	-34	0.31696	0.31695(1)	85(0.012, 7)

The very good agreement between theoretical and corrected experimental values for the individual peak positions (Fig. 5.4) and the unit cell parameter (in nm up to the fifth decimal, Table 5.2) demonstrates that the correction method proposed (section 5.2) is very satisfactory. Further, it follows that it is not necessary to take into account other diffractometer aberrations. In this context it is noted that the effect of specimen transparency, which maybe non neglectable if relatively thin specimens are investigated, is effectively incorporated in the specimen displacement parameter determination, because the diffraction angle dependence of the specimen transparency effect on peak shift obeys; $\Delta(2\theta)_{trans} = t/R\cos\theta$, where t is the specimen thickness; cf. Eq. 5.1 [82].

If an invariant (*i.e.* temperature independent) specimen displacement would have been assumed large errors result in assigning a value for the temperature of the specimen; see results shown in Fig. 5.5, where $\Delta T = T_s - T_s'$ is shown as a function of T_s; T_s' is the temperature for the case that the specimen displacement is taken independent of temperature. Note the large differences, increasing with temperature were resulting from the actual, strong temperature dependence of the specimen displacement.

An additional advantage of the method proposed is that it is unnecessary to adjust the position of the heating strip exactly before a measurement run is performed.

5.4. Conclusions

- Applying a heating chamber in X-ray diffractometry, interpretation of diffraction-peak positions in terms of lattice spacings is only possible if appropriate determination of (zero shift and) specimen displacement (other aberrations are usually of subordinate impor-

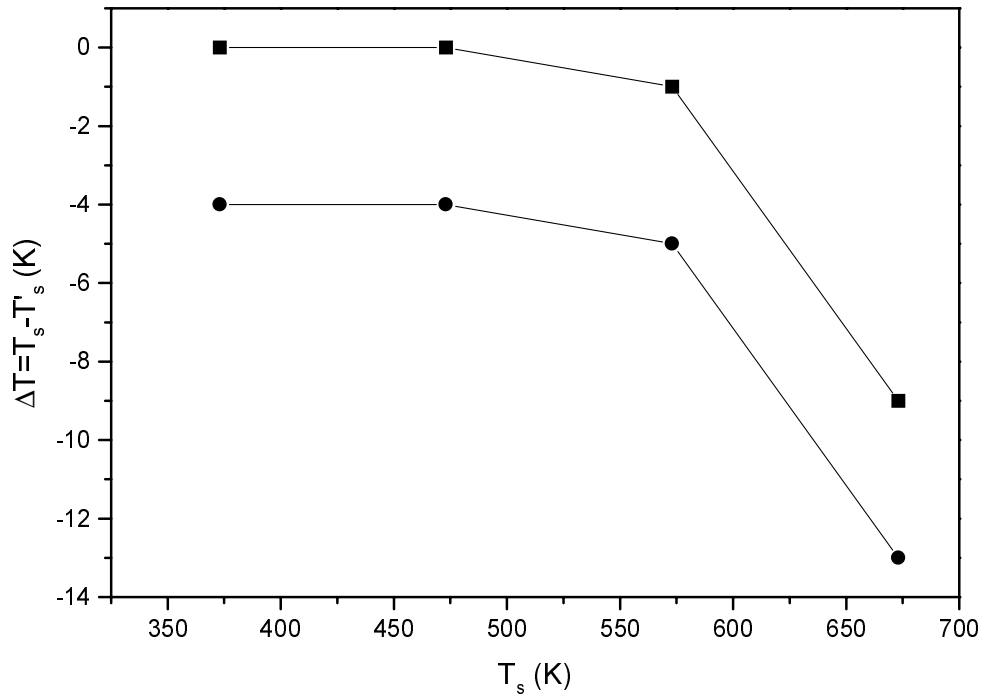

Figure 5.5.: The differences of the true temperature of the specimen determined by use of the method proposed, T_s, and the temperature of the specimen determined assuming a temperature independent sample displacement, T_s', as a function of T_s for one measurement series of Fig. 5.2 (marked as • in Figs. 5.2 and 5.3). (■): using results for T_s' assuming a constant specimen displacement as determined at room temperature; (•): using results for T_s' ignoring the specimen displacement ($s = 0$).

tance) and temperature have been performed for *each* measurement run.

- A method has been proposed that allows the simultaneous determination of (zero shift and) specimen displacement and temperature of the sample to be investigated by use of an internal standard for which the unit cell parameter and the thermal expansion coefficient are known.

- The method proposed leads to (i) corrected values for the individual peak positions that, within experimental accuracy, are equal to the theoretical values, and (ii) unit cell parameter values for the specimen investigated that are equal to the true values (in nm up to the fifth decimal).

Kapitel 6

Kurzfassung der Dissertation in deutscher Sprache

6.1. Einleitung

Interstitielle Mischkristalle auf Basis von Übergangsmetallen mit leichten Elementen wie Bor, Kohlenstoff und Stickstoff sind ein unabdingbarer Bestandteil der technisch wichtigen Materialien mit attraktiven mechanischen Eigenschaften. Die Kenntnisse über die Kristallographie der interstitiellen Phasen und über die Phasenübergänge sind eine Voraussetzung um optimale Materialeigenschaften bei niedrigen und hohen Temperaturen zu erreichen.

Die ersten Arbeiten, die sich mit der Bildung von interstitiellen Mischkristallen beschäftigten, sind die Studien von Hägg [1, 2]. Aus diesen Untersuchungen resultiert eine Regel (s.g. Häggsche Regel) nach der Übergangsmetalle (m) und leichte Elemente (i) nur dann interstitielle Mischkristalle bilden, wenn das Atomradienverhältnis r_i/r_m kleiner als 0.59 ist. Ein weiteres Kriterium zur Bildung von interstitiellen Mischkristallen ist in [3] gegeben: es sagt aus, daß ausgedehnte interstitielle Mischkristalle nur dann gebildet werden, wenn der s.g. *Volume Size Factor**, Ωsf, für den Mischkristall kleiner wie 30×10^6 ist. Eine kleine Löslichkeit von Bor in den Übergangsmetallen wurde ferner von Speiser *et al.* angenommen [4]. Diese begrenzte Löslichkeit wurde mit der hohen Stabilität des p-Orbitales und mit dem großen Atomradius des Bors begründet. Bor ist das größte der interstitiellen Elemente [17].

Alle diese Kriterien setzen geometrische Faktoren ein, die die Stabilität der interstitielle Mischkristalle begrenzen. Unter Berücksichtigung dieser Regeln erwartet man keine interstitielle Löslichkeit von Bor in den $3d^{7..10}$ Übergangsmetallen.

Das System Pd-B spielt eine außergewöhnliche Rolle, das im Hinblick auf diese Prinzipien keinen interstitiellen Mischkristall bilden sollte (z.B. $r_i/r_m = 0.663 \gg 0.59$): es weist trotzdem die größte Löslichkeit aller Übergangsmetalle von Bor auf. Der Pd(B)-Mischkristall ist eine Hochtemperaturphase, die durch rasche Abkühlung bei Raumtemperatur erhalten bleibt. Der palladiumreiche Teil des Systems wird zudem in der Literatur kontrovers diskutiert [5–9]: das Phasendiagramm nach Rogl [9] zeigt einen kfz Mischkristall Pd(B) mit einem Homogenitätsbereich bis $x_B = 0.18$ [10], die Tieftemperaturphasen $Pd_{\sim 6}B$, $Pd_{\sim 5}B$ und die Hochtemperaturphase $Pd_{\sim 4}B$. Die Strukturen dieser Boride sind unbekannt, dagegen wurden die Strukturen der Boride Pd_3B (*oP*16, *Pnma*, Fe_3C type [11]), Pd_5B_2 (*C*2/*c*, Mn_5C_2 type [11]) und Pd_2B (*oP*6, *Pnnm*, anti-FeS_2 type [12]) mittels Einkristalluntersuchungen aufgeklärt. Im Gegensatz dazu weist der palladiumreiche Teil des Phasendiagramms Pd-B ($0 < x_B < 0.18$) nach Alqasmi *et al.* [7] nur das Borid $Pd_{16}B_3$ (= γ-Phase) auf, dessen Struktur als Überstruktur des Mischkristalls röntgenographisch bestimmt wurde.

Ferner wurde eine Entmischungslücke im palladiumreichen Teil des binären Systems Pd-B

*Der *Volume Size Factor* ist definiert durch $\Omega sf = 1/V_a(\partial V/\partial x_i)$, wobei V_a das Atomvolumen des Lösungsmittels und $\partial V/\partial x_i$ die Anfangssteigung der Abhängigkeit des Elementarzellenvolumens, V, zum Molenbruch, x_i, des gelösten Elementes, i, ist.

im Bereich von $0.02 < x_B < 0.10$ in einem Temperaturbereich von 585 K bis 683 K berichtet [7, 13, 69]. Bei Temperaturen kleiner als 585 K wird von einem Zweiphasengebiet bei einem Borgehalt von $0.02 < x_B < 0.15$, in dem der kfz Pd(B)-Mischkristall sich in einen borarmen kfz Mischkristall und in $Pd_{16}B_3$ zersetzt [7].

6.2. Experimentelles

Die untersuchten Proben wurden durch Aufschmelzen aus den reinen Elementen im Lichtbogenofen hergestellt. Auf Angaben über Reinheit und Hersteller der verwendeten Materialien wird auf die einzelnen Kapitel des englischsprachigen Teils der Dissertation verwiesen. Es wurde kein signifikanter Gewichtsverlust bei der Probenherstellung beobachtet. Die Homogenität der Gußproben wurde mit metallographischen (Lichtmikroskopie, teilweise ESMA) und röntgenographischen Methoden überprüft. Die amorphen Legierungen wurden durch Aufschmelzen und Abschrecken aus der Schmelze in einer Drehflügelanlage hergestellt [61].

Für die weiteren Untersuchungen wurden die Proben pulverisiert (gefeilt bzw. gemörsert). Um die dadurch eingebrachten mechanischen Spannungen abzubauen wurden die Pulver unter Vakuum bzw. unter Schutzgasatmosphäre in Quarzkapillare eingeschweißt und warmbehandelt (Auslagerungszeiten und Temperaturen sind im englischsprachigen Teil spezifiziert). Alle Proben wurden nach der Warmbehandlung in Wasser abgeschreckt.

Die Hauptuntersuchungsmethode dieser Arbeit ist die Röntgenbeugung, die bei Raumtemperatur verwendet wurde. Dabei wurde sowohl die Guiniertechnik (Enraf Nonius FR552, Mo$K\alpha_1$-, Cu$K\alpha_1$- und Fe$K\alpha_1$-Strahlung; Filmtechnik) als auch die Diffraktometertechnik mit Bragg-Brentano-Geometrie (Philips X'Pert, Cu$K\alpha_1$- und Cu$K\alpha$-Strahlung) verwendet. Die Guinierfilme wurden densitometrisch mit einem Linescanner ausgewertet (LS 20, KEJ Instrument). Für die Auswertung der Diffraktometermessungen wurde sowohl die Philips Software ProFit, als auch das Rietveldprogrammpaket GSAS [62] verwendet. Die Berechnung der Beugungsprofile in Abschnitt 6.6 wurde ein Auswerteprogramm selbst entwickelt. Für die Diffraktometermessungen bei hohen Temperaturen (vgl. Kap. 6.7) wurde eine Heizkammer (Anton Paar HTK 2000) auf ein Philips X'Pert Diffraktometer (s.o., Cu$K\alpha$-Strahlung) aufgebaut. Die Gitterparameter wurden durch die Methode der kleinsten Fehlerquadrate der Braggschen Gleichung zu den gemessenen Reflexpositionen bestimmt.

Die Dichten (vgl. Kap. 6.3) der Gußproben wurden unter Verwendung der Auftriebsmethode mit CCl_4 als Referenzflüssigkeit bei 289 K bestimmt. Die kalorimetrischen Messungen wurden mit einem DSC (Pyris 1, Pekin Elmer) mit unterschiedlichen Heizraten durchgeführt.

Die transmissionselektronenmikroskopischen Untersuchungen (TEM) wurde an einem Schnitt der Gußprobe druchgeführt, der unter Verwendung von konventionellen Techniken (Ionendünnen) präpariert wurde. Um eine Erwärmung der Probe bei der Präparation zu vermeiden,

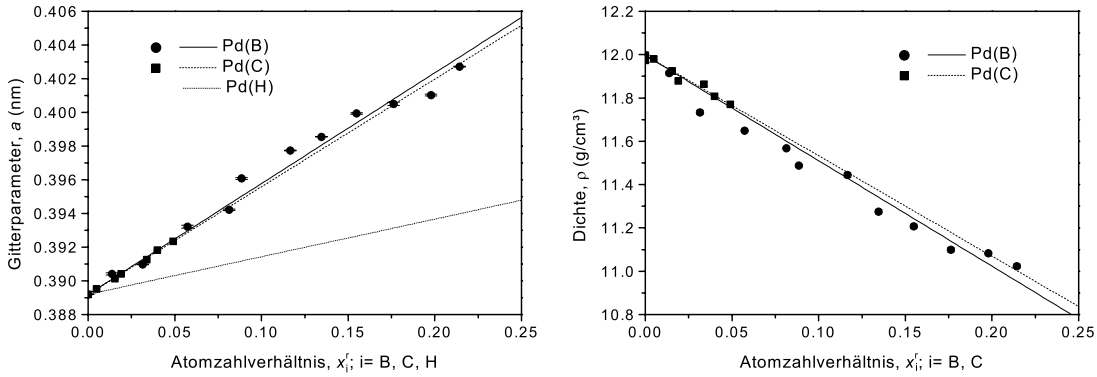

Abb. 6.1.: Links: Gitterparameter, *a*, der Mischkristalle Pd(B), Pd(C) und Pd(H) als Funktion des Atomzahlverhältnisses, x_i^r; Fehlerbalken sind mit angegeben. Rechts: Dichte, ρ, der Mischkristalle Pd(B) und Pd(C) als Funktion des Atomzahlverhältnisses, x_i^r; Fehlerbalken sind mit angegeben.

wurde sie mit flüssigem Stickstoff gekühlt. Die TEM-Untersuchungen fanden an einem JEM 2000 FX Elektronenmikroskop statt (Beschleunigungspannung = 200 kV).

Der Borgehalt der Proben wurde mit Hilfe von induktiv gekoppelter optischer Plasmaemissionspektroskopie bestimmt; der Kohlenstoffgehalt durch Verbrennung der Proben mit zusätzlichem Fe und W im Sauerstoffstrom und anschließender Infrarotabsorbtionsmessung von CO_2 als Verbrennungsprodukt des Kohlensoffes.

6.3. Bildung von intersititellen Mischkristallen auf Basis von kfz Übergangsmetallen; elastische und chemische Wechselwirkung

Gitterparameter- und Dichtemessungen wurden an Randmischkristallen der Übergangsmetallen (α-Co, Rh, Ir, Ni, Pd, Pt), die eine Kristallstruktur isotyp mit Cu aufweisen (kfz, Pearsonsymbol $cF4$, Raumgruppe $Fm\bar{3}m$), mit Bor und teilweise mit Kohlenstoff durchgeführt. Ein besonderer Augenmerk wurde dabei auf die binären Systeme Pd(B) und Pd(C) gerichtet, da diese eine besonders große Löslichkeit aufweisen (bis zu einem Molenbruch von $x_B = 0.186$ [10] bzw. $x_C \simeq 0.05$ [50]).

Bei allen untersuchten Systemen wurde eine Vergrößerung des Gitterparameters des Mischkristalles im Vergleich zum reinen Metall beobachtet. Diese Gitteraufweitung ist ein Indiz für die intersititielle Natur dieser Mischkristalle. Im Falle von Pt(B) steht dies im Widerspruch zur Literatur, wo ein entgegengesetztes Verhalten berichtet wurde [22].

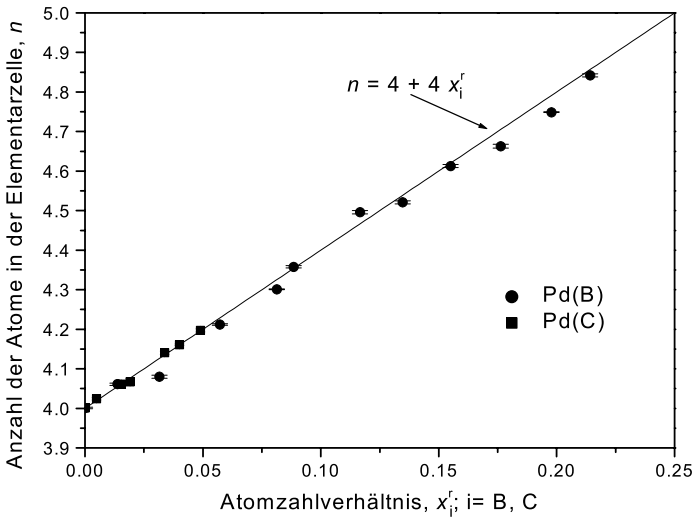

Abb. 6.2.: Anzahl der Atome in der Elementarzelle, n, als Funktion des Atomzahlverhältnisse, x_i^r (i = B (•), C (■)). Die Fehlerbereiche der experimetellen Daten sind ebenfalls angezeigt. Die durchgezogene Linie stellt die theoretische Abhängigkeit $n = 4 + 4x_i^r$ dar.

Bei den binären Systemen Pd(B) und Pd(C) konnte ein linearer Zusammenhang mit positiver Steigung zwischen dem Gitterparameter, a, und dem Atomzahlverhältnis, $x_i^r = x_i/(1-x_i)$, des Mischkristalles beobachtet werden (vgl. Abb. 6.1), wobei die Steigung im Falle von Pd(B) größer als bei Pd(C) ist. Dagegen nehmen die Dichten, ρ, linear mit dem Atomzahlverhältnis ab (vgl. Abb. 6.1); dabei ist die Abnahme im Falle von Pd(B) stärker ausgeprägt im Vergleich zum Pd(C) Mischkristall. Unter Verwendung dieser experimentell bestimmten Größen (a, ρ) läßt sich die Anzahl der Atome in der Elementarzelle, n, mit Hilfe der Beziehung $n = V_c \rho N_{Av}/A$ für die jeweilige Zusammensetzung bestimmen, wobei $V_c = a^3$ das Volumen der Elementarzelle, N_{Av} die Avogadrozahl und A die mittlere Atommasse ist. Vergleicht man diese aus den Experimenten bestimmte Anzahl der Atome in der Elementarzelle mit der theoretischen Anzahl für interstitielle Mischkristalle (für kfz Elementarzelle: $n = 4/(1-x_i) = 4 + 4x_i^r$, [50]) so wird durch die sehr gute Übereinstimmung eindeutig nachgewiesen (vgl. Abb. 6.2), daß Palladium und Bor bzw. Kohlenstoff einen interstitiellen Mischkristall bilden, obwohl dies, den geometrischen Kriterien folgend (s.o.), nicht zu erwarten ist.

EXAFS-Untersuchungen und Diffusionsmessungen von Wasserstoff im Pd(B) Mischkristall weisen auf eine teilweise (statistische) Besetzung der oktaedrischen Lücke der kfz Elementarzelle hin [34, 35]. Damit kann für eine Zusammensetzung von z.B. $x_B = 0.176$, die nahe an der Löslichkeitgrenze liegt, folgender Strukturvorschlag gemacht werden: 4 Pd (a), 0.21×4 B (b). Dies stellt eine defekte (partiell gefüllte) NaCl Struktur dar (Pearson-Parté Symbol [38]: $cF(8-x)$). Der mittlere Abstand der nächsten Nachbarn Pd (Atomposition (a)) und der Atomposition (b), die partiell mit Bor gefüllt ist, $d_{\mathrm{Pd}-(b)} = d_{002} = a/2$, kann dann aus dem Gitterparameter als Funktion des Borgehaltes bestimmt werden. Diese Abhängigkeit kann auf eine hypothetische NaCl Struktur im Pd-B System extrapoliert werden, d.h. volle Besetzung der Atomposition (b) mit Bor. Der so bestimmte Abstand der nächsten Nachbarn ($d_{\mathrm{Pd}-\mathrm{B}} = 0.2287$

nm) ist deutlich kleiner wie die Summe der Atomradien ($r_{\mathrm{Pd}} + r_{\mathrm{B}} = 0.2296$ nm), die aus der Additivität der Atomradien nach dem harten Kugelmodell folgen würde. Dies entspricht einer Volumendifferenz zwischen dem harten Kugelmodell und den experimentellen Daten von 6.2 %.

Negative Abweichungen von der Additivität des 'harten Kugelmodells' bei der Bildung von substitutionellen Mischkristallen sind bekannt [39,40]. Unter den palladiumreichen substitutionellen Mischkristallen der quasihomologen B^{11}-B^{14}-Elemente wird die Additivität nur von dem Pd(Cu) Mischkristall erhalten. Die restlichen substitutionellen Mischkristalle weisen dagegen eine atomare Volumenabnahme bis zu 30.6 % (Pd(Ga)) auf [41–43]. Die größten Volumenkontraktionen in Verbindung mit einem palladiumreichen Mischkristall treten interessanterweise bei den Elementen auf, die die Elektronenkonfiguration ns^2np^1 besitzen (Al, Ga, In, Tl); diese Elektronenkonfiguration hat auch Bor. Dies legt nahe, daß die beobachtete Volumenkontraktion durch einen Ladungsübergang vom gelösten (interstitiellen) Element auf das Palladium beim Legieren verursacht wird.

Die maximale Löslichkeit von vielen substitutionellen lösenden Elementen wird durch die Valenzelektronenkonzentration (c_{ve}) kontrolliert. Für Lösungsmittel isotyp mit Cu ist die Valenzelektronenkonzentration begrenzt durch den Kontakt der Fermifläche mit der $\{111\}$ Brillouinzonenfläche ($c_{\mathrm{ve}} = 1.36$) [44]. Die experimentell beobachteten Löslichkeitsbereiche von Substitutionsmischkristallen, die auf Palladium basieren, sind in Abb. 6.3 dargestellt. Für diese $3d$ Elemente ist die Löslichkeit qualitativ umgekehrt proportional zu ihrer potentiellen Valenz (bestimmt aus der Summe der *s* und *p* Elektronen). Während Cu komplett lösbar ist (Elektronenkonfiguration: $3d^{10}4s^1$) ist die Löslichkeit von As ($3d^{10}4s^24p^3$) vernachläßigbar [31].

Die selben Betrachtungen können auch für interstitielle Mischkristalle auf der Basis von Palladium durchgeführt werden: die maximale Löslichkeit der interstitiellen Elemente H, B, C und N sind in Abb. 6.3 dargestellt. B, C und N sind quasihomolog und haben entsprechend ähnliche Abfolge der Valenzelektronen wie Ga, Ge und As (vgl. Elektronenkonfigurationen in Abb. 6.3). Die maximale Löslichkeit dieser interstitiellen Elemente ist ebenfalls umgekehrt proportional zu ihrer potentiellen Valenz. Offensichtlich ist die Annahme über die hohe Stabilität des *p*-Orbitals von Bor (vgl. Abschnitt 6.1, [4]) nicht gültig. Die hohe Stabilität des *p*-Orbitals wäre für die Einbringung von großen Spannungsenergien bei der Aufnahme des Bors in das Palladiumgitter verantwortlich, wovon die maximale Löslichkeit sicherlich stark beeinflußt wird.

Dagegen kann die Nichtlösbarkeit von N in Pd erklärt werden, wenn man die Valenzelektronenkonzentration als begrenzenden Faktor der maximalen Löslichkeit betrachtet.

Dies zeigt, daß die chemische (elektronische) Wechselwirkung zwischen dem gelösten, interstitiellen Element und der Matrix die Bildung der untersuchten Einlagerungsmischkristallen stärker beeinflußt, wie die elastischen Wechselwirkungen, die durch die Hägg'sche Regel oder das s.g. *Volume Size Factor*-Kriterium betrachtet werden.

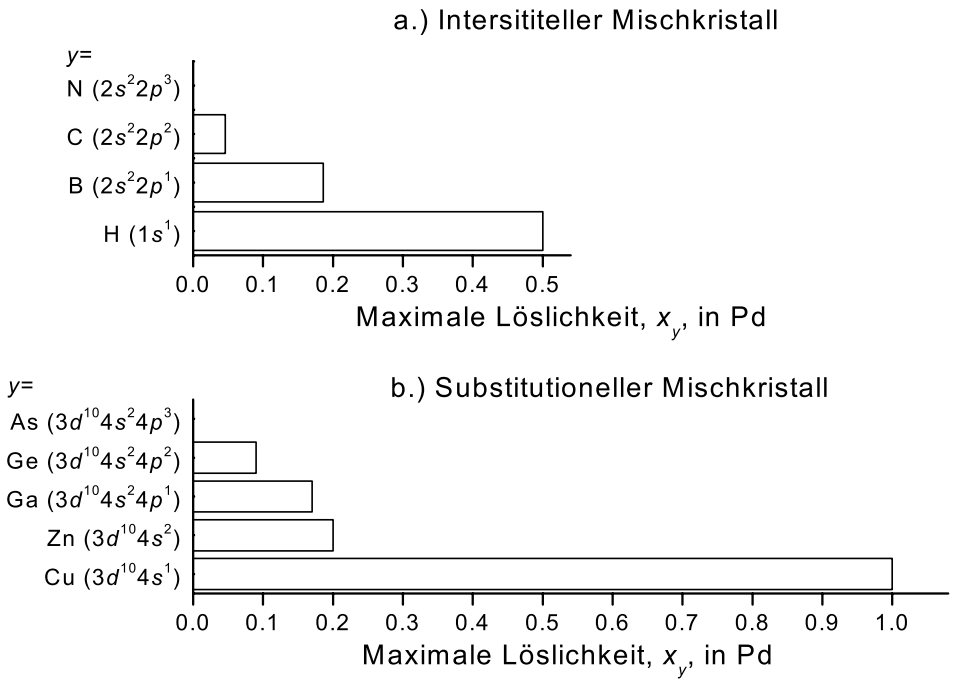

Abb. 6.3.: a.) Maximaler Löslichkeitsbereich und Elektronenkonfiguration der interstitiell lösenden Elemente in Palladium (B, C und N sind Quasihomologe). Die Daten der interstitiellen Mischkristalle Pd(H) und des Systems Pd-N entstammen [31]; Daten von Pd(B) und Pd(C) entstammen [7] bzw. [50]. b.) Maximaler Löslichkeitsbereich und Elektronenkonfiguration einiger substitutionell lösenden Elemente (Quasihomologe) in Palladium. Daten der substitutionellen Mischkristalle Pd(Cu), Pd(Zn) und des Systems Pd-As entstammen [31]; Daten von Pd(Ga) und Pd(Ge) entstammen [42] bzw. [43].

6.4. Die Struktur des palladiumreichen Borids Pd_5B ($Pd_{16}B_3$)

Der palladiumreichen Teil des Phasendiagram des binären Systems Pd-B wird in der Literatur unterschiedlich dargestellt [5–9] (vgl. Kap. 6.1). Alqasmi *et al.* berichtet von einer Tieftemperaturphase $Pd_{16}B_3$ (= γ-Phase), die sich kongruent aus dem Pd(B) Mischkristall bei 670 K bildet und einen Homogenitätsbereich $0.151 < x_B < 0.168$ bei 638 K aufweist. Ihre Kristallstruktur wurde als Überstruktur des interstitiellen Mischkristalles beschrieben (*cF*38, $a = 0.801$ nm = $2a_{Pd(B)}$ [7]. Obwohl mehrere perowskitähnliche Boride und Karbide bekannt sind [45,46], wurde bisher weder über eine interstitielle Überstruktur auf der Basis des Cu Strukturtypes noch andere Strukturen der Pearsonklasse *cF*38 berichtet [38,47–49].

Röntgenographische Untersuchungen von pulverisierten Pd-B Proben in einem Zusammen-

setzungsbereich von $0.15 < x_B < 0.17$ weisen nach einer Warmbehandlung bei 635 K über sieben Wochen auf eine tetragonale Verzerrung der kfz Elementarzelle des Mischkristalles hin. Dies deutet auf die Bildung der Tieftemperaturphase Pd_5B hin. Im Gegensatz zur Literatur (s.o., [7]) konnten keine Beugungsreflexe beobachtet werden, die auf eine Überstruktur des Mischkristalles hinweisen. Eine erneute Warmbehandlung der tetragonal verzerrten Tieftemperaturphase bei 873 K für 30 Minuten führte wieder zum kfz Pd(B) Mischkristall; d.h. die Phasenumwandlung Pd(B)→Pd_5B ist reversibel. Die Umwandlungstemperatur konnte unter Verwendung von DSC-Messungen auf 653(1) K bestimmt werden.

Die Phasenumwandlung folgt der fundamentalen Raumgruppenbeziehung: zu $Fm\bar{3}m$ (Pd(B)-Mischkristall) ist die maximal nichtisomorphe Raumgruppe $I4/mmm$. Unter Berücksichtigung der beobachteten Intensitäten der röntengenographischen Untersuchungen der aufgespaltenen $00l$ Beugungsreflexe des Mischkristalles und der Häufigkeitsgfaktoren der tetragonalen $\{h00\}$ und $\{00l\}$ Ebenen wird deutlich, daß das Achsverhältnis $c/a < \sqrt{2}$ ist. Die Beugungslinien des palladiumreichen Borides Pd_5B wurden in Anlehnung an einer $tI(4-x)$ - Elementarzelle indiziert; die resultierenden Gitterparameter sind: a = 0.28490(4) nm und c = 0.40038(9) nm. Die experimentell bestimmte Anzahl der Atome in der Elementarzelle des Pd(B) Mischkristalles mit der Zusammensetzung $Pd_{83.5}B_{16.5}$ beträgt 4.75 (vgl. Abschnitt 6.3, [50]). Damit kann folgender Strukturvorschlag der tetragonalen Tieftemperaturphase Pd_5B in der Raumgruppe $I4/mmm$ gemacht werden: 2 Pd (a); 0.19×2 B (b).

Palladium weist bei höheren Temperaturen große interstitielle Löslichkeit von Bor [7, 9, 10] und eine ausgedehnte substitutionelle Löslichkeit der homologen Elemente Al und Ga [42] auf. Durch die Substitution von Palladium durch Al und Ga steigt die Valenzelektronenkonzentration und die Konfigurationsentropie an und eine hohe negative Bildungsenthalpie wurde beobachtet [42]. Bei tiefen Temperaturen kann die kfz Struktur dieser Substitutionsmischkristalle nicht mehr aufrecht gehalten werden und es werden deshalb unterschiedlich Tieftemperaturphasen beobachtet: Pd_5Al ($oP24$, *Pnma*; [54]) und $Pd_{13}Ga_5$ ($mC36$, $C2/m$; [55]). Das selbe Verhalten kann im System Pd-B beobachtet werden: der interstitiellen Einbau des valenzelektronenreichen Bors führt zu einer Erhöhung der Valenzelektronenkonzentration und damit zu einer Destabilisierung des kfz Pd(B)-Mischkristalles. Der Mischkristall verzerrt bei tiefen Temperaturen tetragonal. Diese Phasenumwandlung Pd(B)→Pd_5B ist erster Ordnung und folgt der charakteristischen Raumgruppenbeziehung $Fm\bar{3}m \xrightarrow{t3} I4/mmm$ [56].

Ähnliches Verhalten ist im palladiumreichen Teil des System Pd-H beobachtbar. Wasserstoff löst sich bei hohen Temperaturen in Palladium und die kfz Struktur des interstitiellen Mischkristalles Pd(H) bleibt erhalten. Bei niedrigeren Temperaturen und hohen H-Konzentrationen bildet sich das Hydrid $PdH_{1.33}$ (=γ-Phase; $T < 873$ K; $tI(4-x)$; $a = 0.2896$ nm, $c = 0.333$ nm; $c/a = 1.151 < \sqrt{2}$, [58]). Das Palladiumuntergitter dieser Struktur weist Leerstellen auf; so ist die Anzahl der Palladiumatome ≈ 1.5, dagegen ist die Anzahl der Palla-

diumpositionen 2. Dies führt zu einer deutlich kleineren Elementarzelle und zu einem kleineren Achsverhältnis c/a im Vergleich zu Pd_5B.

Das palladiumreiche Borid Pd_5B ($0.15 < x_B < 0.17$) besitzt fast die selbe Valenzelektronenkonzentration wie $PdH_{1.33}$ ($c_{ve}(Pd_5B) \approx 0.5$; $c_{ve}(PdH_{1.33}) = 0.57$; Valenz von Pd = 0; von B = 3; von H = 1).

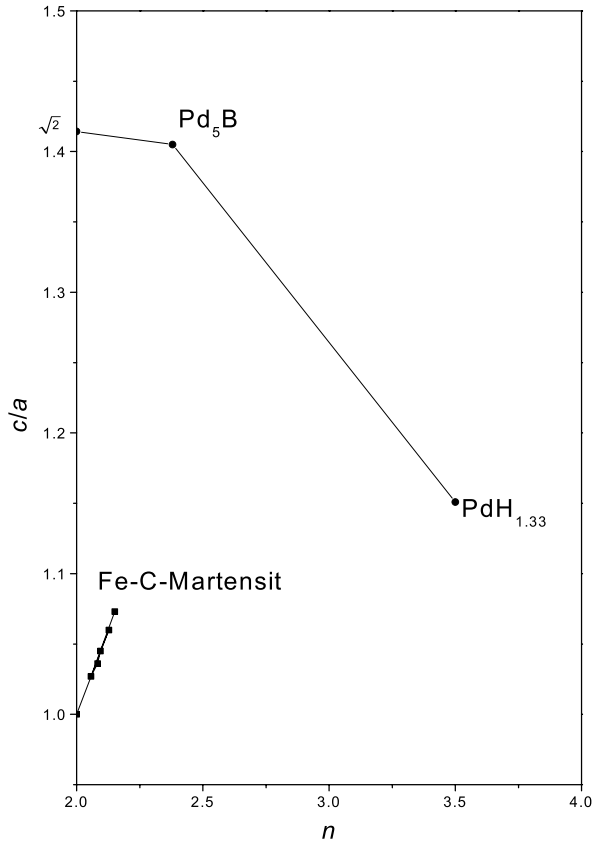

Abb. 6.4.: Achsverhältnisse der $tI(4-x)$ Elementarzelle als Funktion von n für Phase von Übergangsmetallen mit interstitiellen Elementen.

Bei der Betrachtung der Abhängigkeit der Anzahl der Atome in der Elementarzelle, n, von dem Achsenverhältnis c/a für die übergangsmetallhaltigen Phasen mit den intersititiellen Elementen H, B und C wird deutlich, daß die Veränderung von $\Delta(c/a)/\Delta n$ zwischen Pd ('$tI2$'-Elementarzelle, $n = 2$) und Pd_5B ($n = 2.38$) trotz großer Veränderung von c_{ve} klein ist ($0 < c_{ve} < 0.5$) (vgl. Abb. 6.4). Dagegen führt die Leerstellenbildung in Palladiumteilstruktur des Hydrides $PdH_{1.33}$ zu einer besonders starken Verzerrung der tetragonalen Elementarzelle, obwohl sich c_{ve} ähnlich stark zum Pd ändert. Diese beiden homöotypen Phasen sind von dem Cu-Strukturtyp abgeleitet.

Im Unterschied dazu nimmt die Verzerrung der Fe-C-martensitischen Elementarzelle mit zunehmendem Kohlenstoffgehalt zu (vgl. Abb. 6.4). Die Struktur des Martensits ist, im Gegensatz zu den palladiumhaltigen interstitiellen Verbindungen, ein Homöotyp der W-Struktur [49].

6.5. Röntgenbeugungsdaten der Boride Pd_3B und Pd_5B_2 und die Bildung des amorphen Borids Pd_2B

Durch die Komplexität des palladiumreichen Teiles des binären Systems Pd-B lagen keine Pulverbeugungsdaten der Boride Pd_3B und Pd_5B_2 vor, um eine leichte Phasenidentifikation in diesem System zu ermöglichen. Die Struktur der Phasen Pd_3B (*oP*16, *Pnma*, Fe_3C-Strukturtyp) und Pd_5B_2 (*mC*28, $C/2c$, Mn_5C_2-Strukturtyp) wurde durch Einkristalluntersuchungen bestimmt [11]. Die Boride schmelzen kongruent bei 1398 K bzw. bei 1350 K [9]. Dagegen wurde auch von einer peritektoiden Bildung von Pd_3B aus dem Pd(B) Mischkristall und Pd_5B_2 bei 1163 K berichtet [7].

Es ist allgemein bekannt, daß im Bereich tief einschneidender Eutektikas die Bildung von amorphen Legierungen durch rasches Abkühlen aus der Schmelze häufig gebildet werden [59]. Dies wurde auch im Pd-B-System in einem Zusammensetzungsbereich $0.24 < x_B < 0.30$ nachgewiesen [60].

Röntgenographische Untersuchungen der Boride Pd_3B und Pd_5B_2 konnten die Strukturtypen nach [11] bestätigen (Fe_3C bzw. Mn_5C_2). Die Rietveld-Verfeinerung (GSAS, [62]) der Beugungsdaten des Borides Pd_3B bestätigten auch die bekannten Atompositionen (verfeinerte Profilparameter: 3; verfeinerte thermische Parameter: 1; wR_p: 0.32; $R(F^2)(F^2 \geq \sigma(F^2))$: 0.13; Atompositionen *x*, *y*, *z* (diese Arbeit/ [11]): Pd 8(*d*) 0.1800(2)/0.1798, 0.0695(2)/0.0700, 0.3284(3)/0.3276; Pd 4(*c*) 0.0384(3)/0.0372, $\frac{1}{4}$, 0.8456(4)/0.8446; B (nicht verfeinert) 0.884, $\frac{1}{4}$, 0.433).

Die Gitterparameter von Pd_3B sind $a = 0.54602(3)$ nm, $b = 0.75596(4)$ nm, $c = 0.48417(4)$ nm; die der Phase Pd_5B_2 sind $a = 1.27759(12)$ nm, $b = 0.49497(5)$ nm, $c = 0.54704(4)$ nm, $\beta = 97.049(7)^\circ$. Der Vergleich der experimentell bestimmten Intensitäten mit den berechneten [52] zeigen eine sehr gute Übereinstimmung.

Die Zementitstruktur (Fe_3C) ist bei Boriden und Karbiden von Übergangsmetallen eine häufig vorkommende Struktur, dagegen sind keine Oxide und Nidride dieses Strukturtyps der Übergangsmetalle bekannt [47, 48].

Die Achsenverhältnisse b/c und b/a der übergangsmetallhaltiger Boride und Karbide, die Zementitstruktur aufweisen, sind in Abb. 6.5 dargestellt. Es ist deutlich, daß Pd_3B, im Vergleich zu allen anderen mit Fe_3C isotypen Phasen, die größten Achsenverhältnisse b/c und b/a und deshalb die größte Verzerrung der Elementarzelle beim Einbau des interstitiellen Atoms aufweist. Zudem wird sichtbar, daß Pd_3B wie auch die quasihomologen 3*d*-übergangsmetallhaltigen Karbide die kleinsten Achsenverhältnisse a/c aufweisen. Dies kann als eine Tendenz zur Umwandlung in die tetragonale Elementarzelle des U_3Si_2-Strukturtyps, der strukturell verwand mit der Zementitstruktur ist [66].

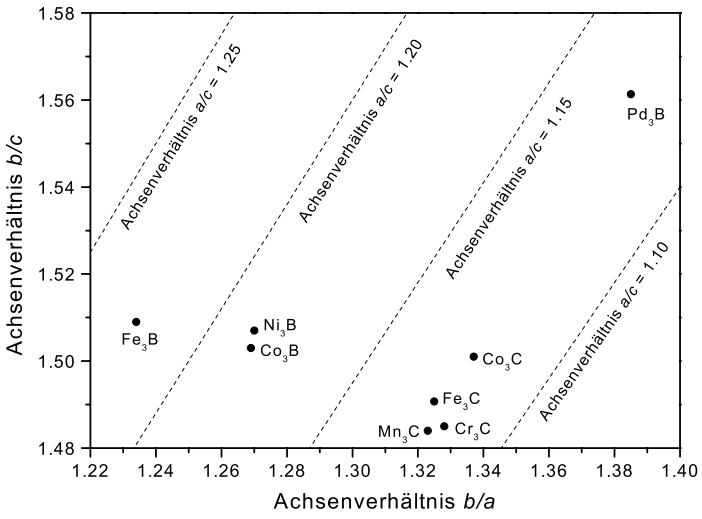

Abb. 6.5.: Die Achsenverhältnisse b/c und b/a der übergangsmetallbasierenden Boride und Karbide des Zementitstrukturtyps ([48, 99], diese Arbeit)

Das Nagel-Tauc-Kriterium beschreibt ein Modell der Bildung von metallischen Gläsern basierend auf der Näherung der quasifreien Elektronen [67]. Das Kriterium fordert, daß ein amorpher Phasenübergang dann möglich ist, wenn $2K_\mathrm{F} \simeq K_\mathrm{p}$ ist ($2K_\mathrm{F}$: Durchmesser der Fermikugel, K_p: Wellenzahl des ersten Streumaximums). Für die amorphen Legierungen $Pd_{67}B_{33}$ und $Pd_{66}B_{34}$ wurde K_p mit Hilfe der Braggschen Gleichung bestimmt: $K_\mathrm{p} = 4\pi \sin\theta/\lambda = 28.0\ \mathrm{nm}^{-1}$. Der Durchmesser der Fermikugel läßt sich durch $K_\mathrm{F} = \sqrt[3]{3\pi c_\mathrm{ve}\rho N_\mathrm{Av}/\sum_i x_i m_i} = 14.4\ \mathrm{nm}^{-1}$ bestimmen [68] (m_i = Atommasse der i-Komponente; Valenz von Palladium = 0; Valenz von Bor = 3 für T = 0 K): $2K_\mathrm{F} = 28.8\ \mathrm{nm}^{-1} \approx K_\mathrm{p}$. Dies zeigt, daß die Bildung der amorphen Legierung Pd_2B durch rasches Abkühlen aus der Schmelze mit den Voraussagen des Nagel-Tauc-Kriteriums sehr gut übereinstimmt.

6.6. Zerfall des interstitiellen Mischkristalles Pd(B)

Entmischungslücken bei interstitiellen kfz Mischkristallen sind eine seltene Erscheinung. Nur bei den 3 binären Systemen Th-C, Pd-H und Pd-B ist diese Erscheinung bekannt. Die Entmischung im System Pd-H wurde ausführlich untersucht (z.B. [71]); dagegen existieren nur ein paar wenige Arbeiten, die sich mit der Entmischungslücke in den Systemen Th-C und Pd-B beschäftigen [7, 13, 69, 72–74]. Alle diese strukturellen Arbeiten untersuchten den Ausgangs- und Endzustand des Zerfalles des Mischkristalles; Untersuchungen über die Kinetik und den Reaktionsweg der Entmischung sind nicht bekannt.

Bei der Entmischung zerfällt der homogene Mischkristall in eine borarme und borreiche Produktphase, die mit dem Ausgangsmischkristall isotyp sind. Nach dem heutigen Kenntnisstand besetzt Bor statistisch die oktaedrischen Lücken des kfz Pd-Gitter. Variationen im Anteil des gelösten interstitiellen Elementes verursachen Variationen des Gitterparameters und lassen sich deshalb sehr gut mit Hilfe von Röntgenbeugungsanalyse beobachten. Im Falle von Pd(B)

ist die lineare Abhängigkeit des Gitterparameters vom Atomzahlverhältnis genau bekannt (vgl. Abschnitt 6.3, [50]).

Die Entmischung führt zu einer räumlichen Fluktuation des Gitterparameters. Im Röntgenbeugungsexperiment werden Variationen der Netzebenenabstände des Gitters in Richtung des Beugungsvektors beobachtet. Dadurch lassen sich bei diesen Experimenten die *hkl* Beugungsreflexe des zerfallenden Mischkristalles durch ein eindimensionales Modell simulieren.

Unter der berechtigten Annahme, daß die Entmischung diffusionsgesteuert ist, läßt sich das Konzentrationsprofil durch $c(x,t) = A + B \cdot \mathrm{erf}(\frac{x}{2\sqrt{Dt}})$ beschreiben [75], wobei x = Position (im Kristall), D = Diffusionskoeffizient, t = Zeit und A und B Konstanten sind. Bei bestimmten Übergangsstadien der Entmischung kann das Profil des Gitterparameters, a, und damit auch des Borgehaltes in 3 Bereiche (borarm, borreich und entmischende Matrix) unterteilt und als Funktion des Ortes in der Struktur in Richtung parallel zum Beugungsvektor beschrieben werden (vgl Abb. 6.6). S_1 und S_2 sind die Positionen der Grenzflächen zwischen borarmen Bereich und Übergangsbereich bzw. Übergangsbereich und borreichem Bereich.

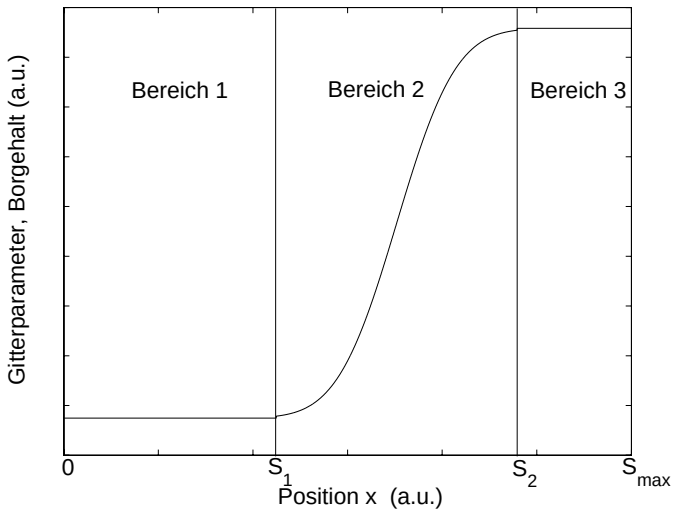

Abb. 6.6.: Verlauf des Gitterparameters und damit des Borgehaltes des zerfallenden Mischkristalles als Funktion des Ortes in der Struktur.

Zur Berechnung der *hkl* Beugungslinienprofile wird der Kristall als eine Reihe von (*hkl*) Gitterebenen senkrecht zum Beugungsvektor angesehen, deren Abstand $d(x) = a(x)/\sqrt{h^2+k^2+l^2}$ beträgt. Das strukturelle Linienprofil, $I(2\theta)$, läßt sich aus dem Verlauf des Gitterparameters (vgl. Abb. 6.6) berechnen [76].

Zur Berechnung der beobachteten Beugungsprofile wird das strukturelle Linienprofil mit der s.g. instrumentellen Verbreiterungsfunktion gefaltet. Das strukturelle Linienprofil beinhaltet die Linienverbreiterung auf Grund von Konzentrationsschwankungen. Andere Effekte, die zur Linienverbreiterung beitragen (z.B. Mikrodehnung), führen zu einer zusätzlichen Verbreiterung. Die freien Parameter der simulierten Beugungsprofile lassen sich durch Anpassung an die experimentellen Linienprofile bestimmen. Randbedingungen und Einzelheiten der Fitprozedur

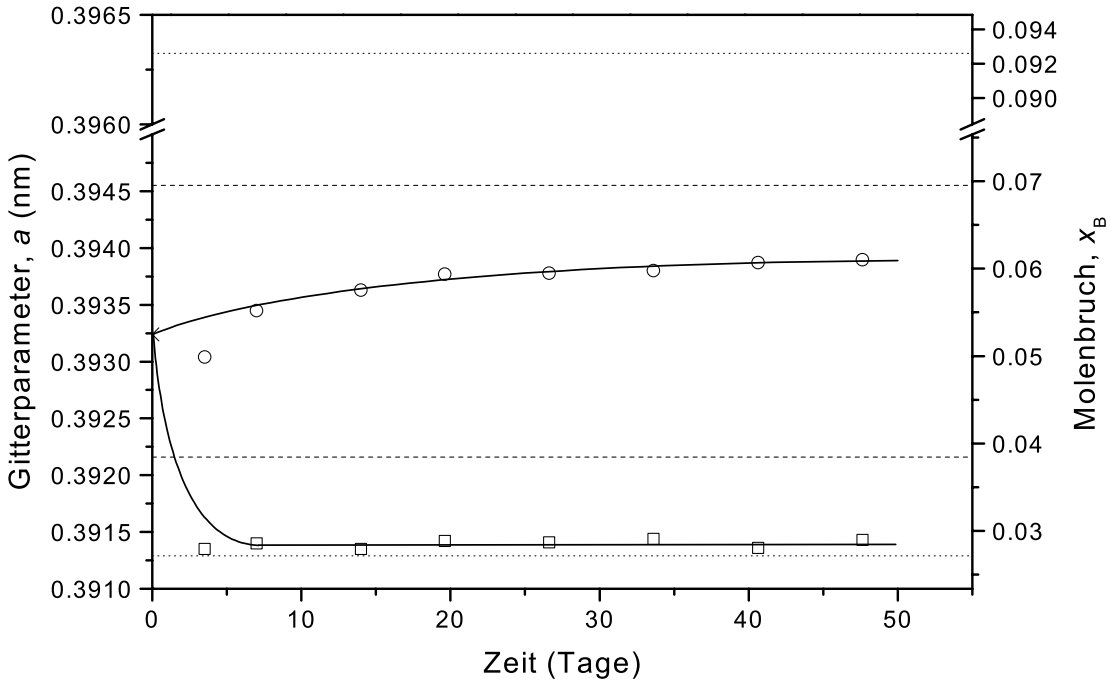

Abb. 6.7.: Gitterparameter, *a*, und Borgehalte der einzelnen Stadien des Zerfalles des Mischkristalles bei einer Warmbehandlung bei $T = 628$ K als Funktion der Zeit (borarme Phase = □, borreiche Phase = ◯, Ausgangsmischkristall bei $t = 0 = \times$). Experimentell bestimmte Borgehalte der entmischten Phasen nach [13] sind eingezeichnet (gepunktete Linien). Die gestrichelten Linien entsprechen den unter Verwendung der quasichemischen Nährung bestimmten Borgehalte der Produktphase [13].

sind im englischsprachigen Teil spezifiziert (vgl. Kapitel 4.2).

Bei Elektronenbeugungsuntersuchungen des homogenen Mischkristalles konnten scharfe Beugungsreflexe beobachtet werden; dagegen wurden bei Unteruchungen des entmischten Zustandes diffuse Beugungsreflexe und Streaks in die <011> Richtung beobachtet. Das Hellfeldbild der TEM-Untersuchungen des homogenen Mischkristalles zeigt eine homogene Probe mit deutlichen Versetzungen, die vermeindlich beim Abschrecken in Wasser nach der Homogenitätsglühung entstanden sind. Die Versetzungsdichte des homogenen Mischkristalles ist mit $2 \cdot 10^{13}$ m^{-2} deutlich höher, als sie für geglühte Metalle zu erwarten ist [79]. Das Hellfeldbild der TEM-Untersuchungen des entmischten Zustandes zeigt deutliche Inhomogenitäten in der Größenordnung von 10 nm.

Aus den Anpassungen der theoretischen Röntgenlinienprofilen an experimentellen Daten der Diffraktometeruntersuchungen lassen sich die Gitterparameter der einzelnen Phasen des zerfallenden Mischkristalles und damit der Borgehalt bestimmen. Aus Abb. 6.7 wird deutlich,

daß der Borgehalt der borarmen Phase für alle Stadien des Zerfalles des Mischkristalles konstant ist; dagegen nimmt der Borgehalt der borreichen Phase mit zunehmender Auslagerungszeit zu. Damit läßt sich der Zerfallsprozess wie folgt beschreiben: die borarme Phase scheidet von Beginn der Warmbehandlung aus und der Ausgangmischkristall reichert sich allmählich mit Bor an. Die bestimmten Borgehalte der borreichen Produktphase sind signifikant kleiner verglichen mit den experimentellen Daten der Literatur (vgl. Abb. 6.7, [13]).

Die Entmischungslücke kann mit Hilfe der quasichemischen Nährung theoretisch beschrieben werden [13]; die so vorhergesagte Breite der Entmischungslücke stimmt mit den in dieser Arbeit experimentell bestimmten Breite sehr gut überein.

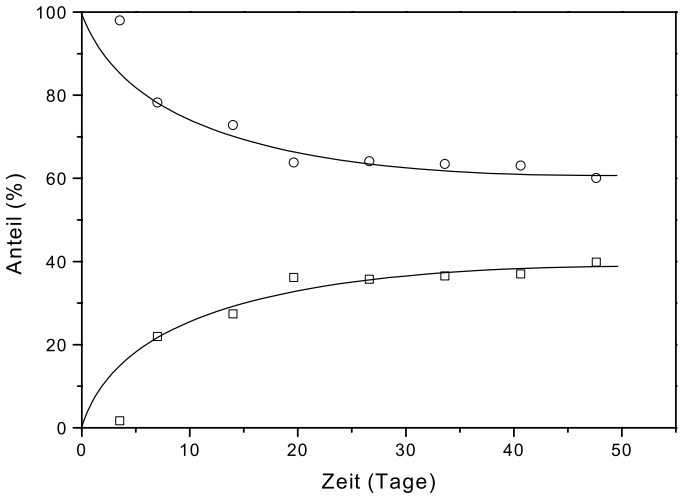

Abb. 6.8.: Aus den Röntgenbeugungsexperimenten bestimmte Anteile der Produktphasen als Funktion der Auslagerungszeit.

Die Anteile der borarmen und borreichen Phase sind als Funktion der Auslagerungszeit in Abb. 6.8 dargestellt. Damit wird deutlich, daß der Zerfall des Mischkristalles nach ca. 25 Tagen abgeschlossen ist. Mit den bestimmten Anteilen und dem dazugehörenden Borgehalt läßt sich Richtigkeit der Linienprofileanpassung überprüfen. Es zeigt sich, daß in jedem Stadium des Zerfalles des Mischkristalles der Borgehalt konstant ist und dieser Borgehalt nur um 0.4 At.-% von dem des Ausgangsmischkristall abweicht.

Bei der Anpassung der Beugungsprofile an die experimentellen Daten kann eine Verbreiterung der Beugungsreflexe beobachtet werden. Die Halbwertsbreiten der beobachteten Beugungreflexe wurden um die instrumentelle Verbreiterung korrigiert, die mit einem Standardmaterial (LaB_6) bestimmt wurde.

Bei der Anwendung der Williamson-Hall-Analyse [14] wird deutlich, daß beim Zerfall des Mischkristalles Mikrodehnungen, ε, entstehen, die selbst bei vollständiger Entmischung um einen Faktor 2 größer sind im Vergleich zum homogenen Mischkristall:

$$\varepsilon(\text{homogener Mischkristall}) = 3.6 \cdot 10^{-4}; \qquad \varepsilon(\text{entmischter Zustand}) = 7.2 \cdot 10^{-4}.$$

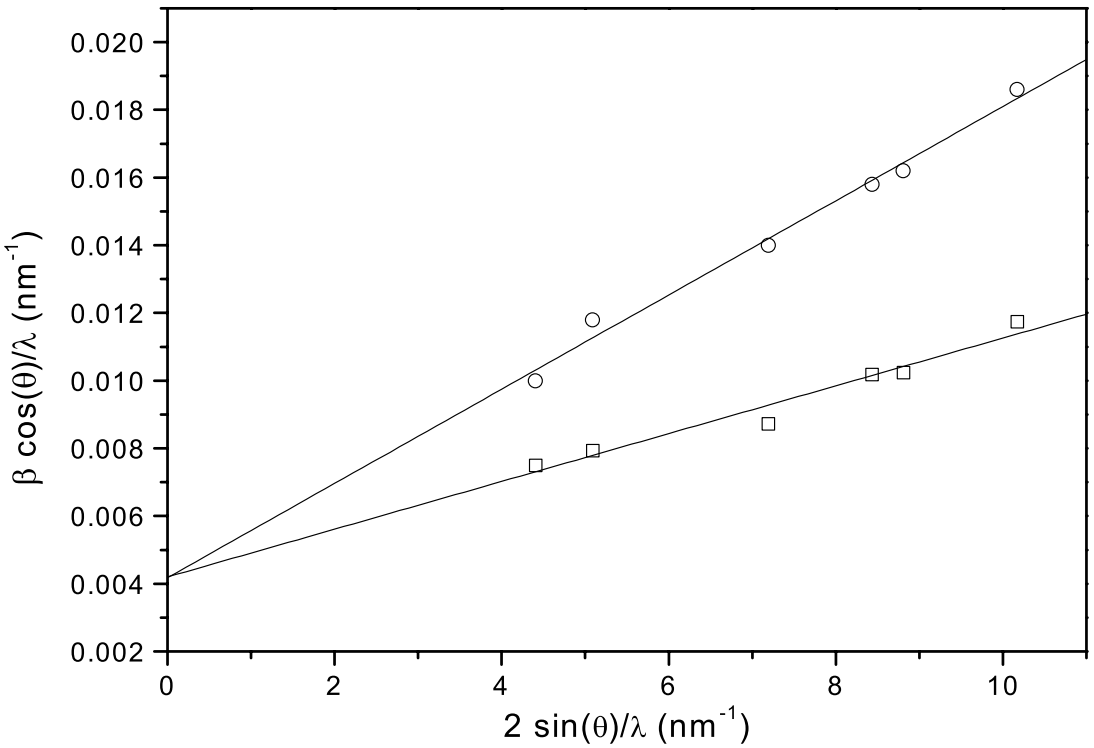

Abb. 6.9.: Williamson-Hall Auftragung für den entmischten Zustand (= ◯, Warmbehandlung bei 628 K für 33.6 Tage) und für den homogenen Mischkristall (= □). β = integrierte Breite der Beugungsreflexe in rad 2θ.

Dies ist in Abb. 6.9 dargestellt. Die Steigung der an die experimentellen Daten angepaßten Geraden des entmischten Zustandes ist deutlich größer wie die des homogenen Mischkristalles. Der homogene Mischkristall weist ebenfalls Mikrodehnungen auf, die durch den Einbau der relativen großen Anzahl von Versetzungen veruracht werden. Die Versetzungdichte des homogenen Mischkristalles kann nach [81] aus der Teilchengöße und der Mikrodehnung bestimmt werden. Diese aus den Röntgenbeugungsprofilen bestimmt Versetzungdichte von $1.3 \cdot 10^{13}\,\mathrm{m}^{-2}$ stimmt sehr gut mit der aus den elektronenmikroskopischen Untersuchungen bestimmten Versetzungsdichte (s.o.) überein. Bei der Williamson-Hall-Analyse kann aus dem Ordinatenabschnitt die Teilchengröße bestimmt werden. Diese beträgt $\sim$ 240 nm und trägt damit einen nicht zu vernachläßigen Beitrag zur Verbreiterung der Beugungslinie bei. Aus Abb. 6.9 wird deutlich, daß der Zerfall des Mischkristalles keine Einfluß auf die Teilchengröße hat.

6.7. Eine neue Methode zur simultanen Bestimmung von Probenhöhenfehler und Probentemperatur bei der Hochtemperaturdiffraktometrie unter Verwendung der Bragg-Brentano-Geometrie

Die größten Diffraktometerfehler bei der Verwendung der Bragg-Brentano-Geometrie im Beugungswinkel 2θ sind die Nullpunktsverschiebung, $\Delta(2\theta)_{zs}$, und der Probenhöhenfehler, $\Delta(2\theta)_{sd}$ [82]. Die Nullpunktsverschiebung verursacht eine über den gesamten Winkelbereich konstante Verschiebung der Beugungsreflexe [82] und kann unter Voraussetzung, daß es die einzigste Fehlerquelle ist, mit Hilfe der s.g. *Reflection-Pair-Methode* ohne Verwendung von Standardmaterialien bestimmt werden [86–88]. Es kann sicher davon ausgegangen werden, daß dieser Fehler im Laufe einer Meßserie konstant bleibt. Kommt noch zusätzlich der Probenhöhenfehler ($\Delta(2\theta)_{sd}$ proportional zu $\cos(\theta)$, [82]) vor, so können die Fehler nur mit Hilfe von Standardmaterialien, dessen Reflexpositionen genau bekannt sind, bestimmt werden [89].

Werden Hochtemperaturdiffraktometeruntersuchungen mit Hilfe einer Heizkammer, bei der das Heizband auch der Präparatträger ist, an einem Bragg-Brentano-Goniometer durchgeführt, so ändert sich die Probenhöhe für unterschiedliche Temperaturen infolge der thermischen Ausdehnung des Heizbandes. Dies entspricht einem variablen, unbekannten Probenhöhenfehler. Zusätzlich ist die Temperatur der Probe nicht hinreichend bekannt. Die Temperatursteuerung bzw. -messung erfolgt meist über ein Thermoelement, das an der Unterseite der Probe angeschweißt ist. Auf Grund von unzureichendem Wärmekontakt zwischen Probe und Heizband kann die wahre Probentemperatur, T_s, von der des Thermoelementes, T_{tc}, stark abweichen. Durch die Überlagerung der Fehler ist es nicht möglich, die Verschiebungen der beobachteten Reflexpositionen während der Hochtemperaturuntersuchungen direkt dem Temperaturfehler oder dem Probenhöhenfehler zuzuordnen.

Im Folgenden wird eine neue Methode vorgestellt, die eine simultane Bestimmung des Probenhöhenfehlers und der Probentemperatur ermöglicht. Sie ist in zwei Schritte unterteilt und basiert auf der Verwendung eines internen Standards, dessen Positionen der Beugungsreflexe bei Raumtemperatur sowie dessen thermische Ausdehnungskoeffizient genau bekannt sind:

i) Im ersten Schritt wird die Nullpunktsverschiebung und der Probenhöhenfehler bei Raumtemperatur bestimmt. Die Abweichung der Reflexpositionen zwischen den theoretischen, $2\theta_t$, (d.h. sowohl die Nullpunktsverschiebung als auch der Probenhöhenfehler sind gleich Null) und der beobachteten Reflexpositionen, $2\theta_o$, des internen Standards kann beschrieben werden als

$$\Delta(2\theta) = 2\theta_t - 2\theta_o = -\frac{2s}{R}\cos(\theta_t) + \Delta(2\theta)_{zs}, \tag{6.1}$$

wobei R der Goniometerradius und s der Probenhöhenfehler ist. Gleichung 6.1 zeigt einen linearen Zusammenhang zwischen $\Delta(2\theta)$ und $\cos(\theta_t)$. Damit lassen sich s und $\Delta(2\theta)_{zs}$ durch die Steigung und den Ordinatenabschnitt einer Ausgleichsgeraden unabhängig voneinander bestimmen. Ist s positiv, so ist die aktuelle Lage der Probe über der Idealposition.
ii) Im zweiten Schritt wird die Probentemperatur und -höhenfehler aus den Positionen der Beugungsreflexe des internen Standardes bei hohen Temperaturen wie folgt bestimmt:

Bei erhöhten Temperaturen können die Lage der Beugungsreflexe des Standards[†] mit Hilfe der Braggschen Gleichung und des Gitterparameters bei Raumtemperatur berechnet werden, wenn der thermische Ausdehnungskoeffizient bekannt ist. Daraus folgt die Beziehung zwischen theoretischen Reflexlage, $2\theta_t$, und der erwarteten Reflexlage (z. B. wenn die Peaklage durch einen Probenhöhenfehler und eine Nullpunktsverschiebung beeinflußt wird), $2\theta_{ex}$:

$$\begin{aligned} 2\theta_{ex}(T) &= 2\theta_t(T) - \Delta(2\theta)_{sd}(T) - \Delta(2\theta)_{zs} \\ &= 2\arcsin\left(\tfrac{\lambda}{2}\tfrac{\sqrt{h^2+k^2+l^2}}{a(T)}\right) + \tfrac{2s}{R}\left[1-\left(\tfrac{\lambda}{2}\tfrac{\sqrt{h^2+k^2+l^2}}{a(T)}\right)^2\right]^{1/2} - \Delta(2\theta)_{zs}. \end{aligned} \tag{6.2}$$

Die Abhängigkeit des Gitterparameters kann beschrieben werden durch

$$a(T) = a_0 + \Delta a(T);\ \Delta a(T) = a_0 \sum_{i=1}^{3} \alpha_i (T - T_0)^i, \tag{6.3}$$

wobei a_0 der Gitterparameter bei der Bezugstemperatur T_0 und α_i der thermische Ausdehnungskoeffizient ist (vgl. Datensammlung [94, 95]).

Die Nullpunktsverschiebung in Gl. 6.2 wurde bei der Raumtemperaturmessung bestimmt (Schritt i)). Die Werte von s und T können mit Hilfe der gemessenen Reflexpositionen des internen Standards durch Minimierung von $\sum_i (2\theta_{ex,i} - 2\theta_{o,i})^2$ bestimmt werden, wobei $2\theta_{ex,i}$ durch Gl. 6.2 gegeben ist (der Index i berücksichtigt die einzelnen Beugungsreflexe bei der selben Temperatur).

Die Methode wurde an Wolfram für eine Reihe von Temperaturen angewandt, wobei Germanium als interner Standard diente. Die bestimmten Gitterparameter sind in Tabelle 6.1 dargestellt und mit Literaturwerten verglichen. Es wird deutlich, daß die mit der hier vorgestellten Methode bestimmten Gitterparameter bei unterschiedlichen Temperaturen mit den Werten aus der Literatur eine sehr gute Übereinstimmung zeigen (bis zur fünften Dezimalen in nm). Ferner wird damit deutlich, daß weitere Diffraktometerfehler nur einen untergeordneten Einfluß auf die Meßergebnisse haben.

[†]Die Methode wird hier an Hand einer kubischen Kristallstruktur des Standards gezeigt, das allerdings keine Einschänkung darstellt.

Tabelle 6.1.: Gitterparameter von Wolfram bei unterschiedlichen Temperaturen: für eine mit der hier vorgestellten Methode bestimmte Probentemperatur, T_s, aus Literaturwerten berechnet: $a_t(T_s)$ [94, 96]; nach Korrektur der gemessenen Reflexpositionen mit der beschriebenen Methode bestimmte Gitterparameter: a_{det}. Das *Figure-of-Merit* nach [53] ist mit angegeben. $\Delta T = T_s - T_{tc}$, T_{tc} = Temperatur des Thermoelements; s ist der Probenhöhenfehler, der mit der beschriebenen Methode bestimmt wurde.

T_{tc} (K)	T_s (K)	ΔT (K)	s (μm)	$a_t(T_s)$ (nm)	a_{det} (nm)	F_7
299			-12	0.31648	0.31648(1)	107(0.009, 7)
373	364	-9	-12	0.31657	0.31658(1)	102(0.010, 7)
473	468	-5	-13	0.31671	0.31671(1)	130(0.008, 7)
573	571	-2	-14	0.31687	0.31688(1)	166(0.006, 7)
673	634	-39	-34	0.31696	0.31695(1)	85(0.012, 7)

Die Temperaturabweichung und der Probenhöhenfehler werden bei steigender Temperatur größer. Mehrere Meßserien haben gezeigt, daß das Verhalten dieser Fehler nicht vorhergesagt werden kann. Die Ursachen hierfür liegen in einer nichtvorhersehbaren Deformation des Heizbandes aufgrund der thermischen Ausdehnung bzw. in kleinen Unterschieden in der Probenpräparation (Probendicke, Packungsdichte, etc.) der einzelnen Meßserien. Dies zeigt die Notwendigkeit, daß die o.g. Fehler bei *jeder* Messung bestimmt werden müssen, um exakte Gitterparameter/Reflexpositionen bei hohen Temperaturen zu bestimmen. Ferner konnte gezeigt werden, daß die Vernachläßigung des Probenhöhenfehlers ($s = 0$ bzw. er wird als unabhängig von T angenommen $s = s(\text{Raumtemperatur}) \neq s(T) = \text{konstant}$) einen Fehler in der Temperatur von 13 K (bzw. 8 K) verursacht, im Vergleich zur wahren Temperatur (634 K), die mit der hier vorgestellten Methode bestimmt wurde.

Appendix A

Phasediagrams of the Pd-B system

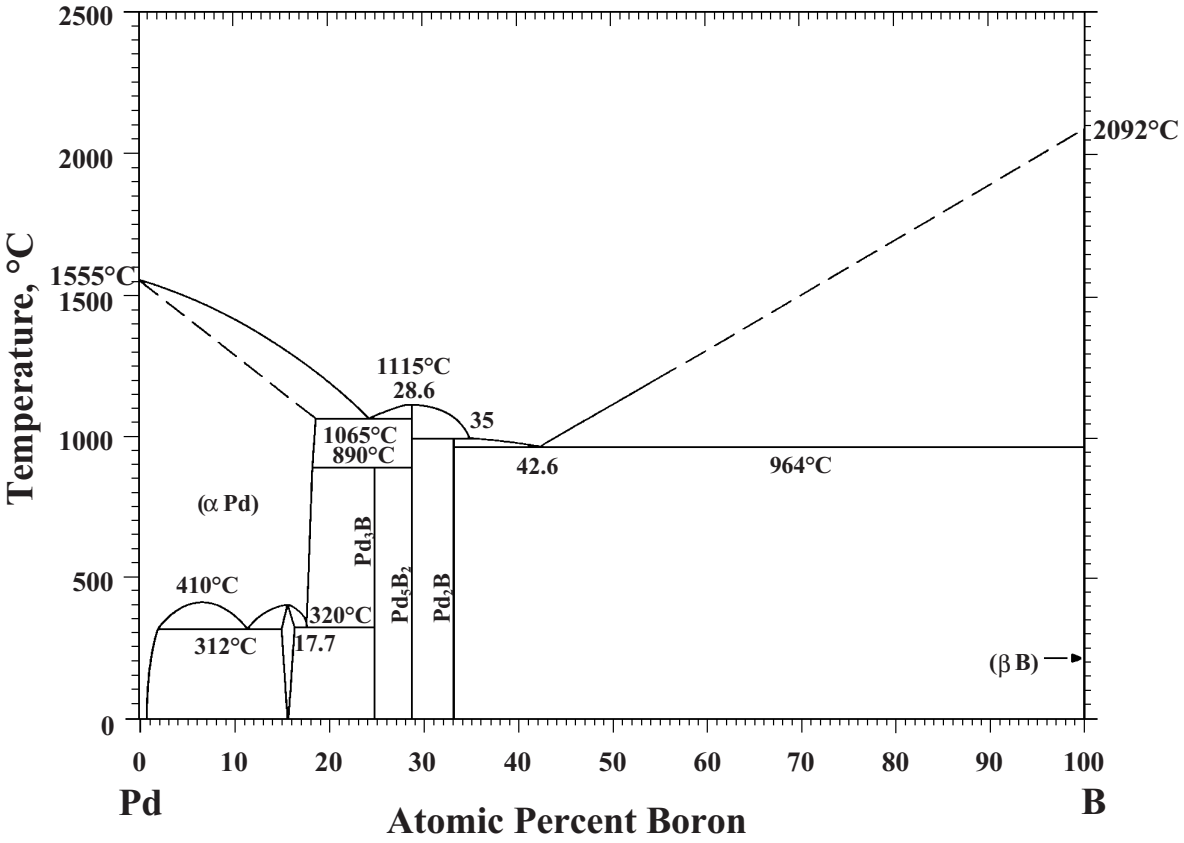

Figure A.1.: The phase diagram according [8].

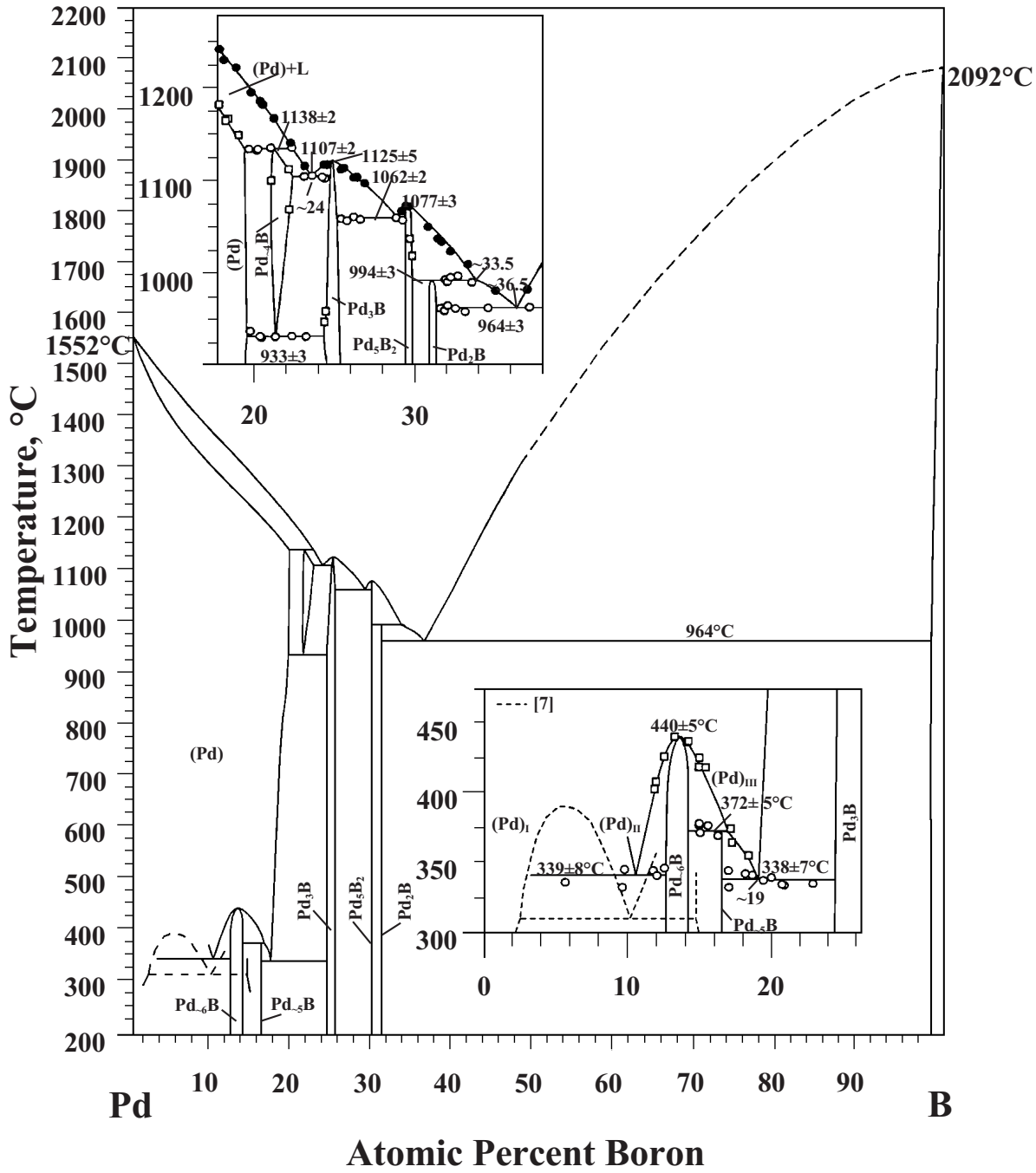

Figure A.2.: The phase diagram according [9].

References

[1] G. Hägg, *Gesetzmässigkeiten im Kristallbau bei Hydriden, Boriden, Carbiden und Nitriden der Übergangselemente*, Z. Phys. Chem. B **12** (1931) 33–56.

[2] G. Hägg, *Eigenschaften der Phasen von Übergangselementen in binären Systemen mit Bor, Kohlenstoff und Stickstoff* , Z. Phys. Chem. B **12** (1931) 221–232.

[3] H. W. King, *Quantitative size-factors for interstitial solid solutions*, J. Mater. Sci. **6** (1971) 1157–1167.

[4] R. Speiser, J. W. Spretnak, and W. J. Taylor, *Effective diameter of solute atoms in interstitial solid solutions*, Trans. Metall. Soc. AIME **46** (1954) 1168–1175.

[5] H. Ipser and P. Rogl, *Constitution diagrams of binary systems: Pd-B and Ir-B*, Proceedings of CHALPHAT X (1981) 73.

[6] H. Ipser and P. Rogl, *Constitution diagrams of the binary Pd-B and Ir-B*, J. Less-Common Met. **82** (1981) 363.

[7] R. A. Alqasmi, H. Brodowsky, and H.-J. Schaller, *Zur Konstitution von Palladium-Bor-Legierungen*, Z. Metallkd. **73** (1982) 331–334.

[8] P. K. Liao, K. E. Spear, and M. E. Schlesinger, *The Pd-B system*, J. Phase Equilib. **17** (1996) 340–346.

[9] P. Rogl, *Pd-B-C*, in: *Phase Diagrams of Ternary Metal-Boron-Carbon Systems* (G. Effenberg, ed.), 234, ASM International, 1998.

[10] M. Beck, M. Ellner, and E. J. Mittemeijer, *Unit cell parameter and densities of the solid solution Pd(B)*, Mater. Sci. Forum **321-324** (2000) 604–609.

[11] E. Stenberg, *The crystal structure of Pd_5B_2 (Mn_5C_2) and Pd_3B,* Acta Chem. Scand. **15** (1961) 861–870.

[12] L. E. Tergenius and T. Lundström, *The crystal structure of Pd_2B,* J. Solid State Chem. **31** (1980) 361–367.

[13] H. Brodowsky and H.-J. Schaller, *Entmischung in Pd-B-Legierungen,* Ber. Bunsenges. **7** (1976) 656–661.

[14] G. K. Williamson and W. H. Hall, *X-ray line braodening from filed aluminium and wolfram,* Acta Metall. **1** (1953) 22–31.

[15] G. Hägg, *Kristallbau der Verbindung Fe_2B,* Z. Phys. Chem. B **11** (1930) 152–161.

[16] V. M. Goldschmidt, *Über Atomabstände in Metallen,* Z. Phys. Chem. **133** (1928) 397–419.

[17] E. Teatum, K. Gschneidner, and J. Waber, *Compilation of calculated data useful in predicting metallurgical behaviour of the elements in binary alloy system,* Tech. Rep. LA-4003, Los Alamos Scientific Laboratory (1968).

[18] L. Pauling, *Atomic radii and interatomic distances in metals,* J. Am. Chem. Soc. **69** (1947) 542–553.

[19] C. Lerner and M. C. Cadeville, *Sur la solubilité du bore dans le cobalt,* Scr. Metall. Mater. **7** (1973) 941–944.

[20] P. Rogl, H. Nowotny, and F. Benesovsky, *Ein Beitrag der Strukturchemie der Iridiumboride,* Monatsh. Chem. **102** (1971) 678–686.

[21] J. D. Schöbel and H. H. Stadelmaier, *Das Zweistoffsystem Nickel-Bor,* Z. Metallkd. **56** (1965) 856–859.

[22] H. Brodowsky and H. Sagunski, *Thermodynamik properties of Pt-B solid solution,* Ber. Bunsenges. **87** (1983) 803–805.

[23] H. W. King, *Crystal structures of the elements at 25°C,* Bull. Alloy Phase Diagrams **2** (1981) 402.

[24] A. Maeland and T. B. Flanagan, *Lattice constants and thermodynamic parameters of the hydrogen-platinum-palladium and deuterium-platinum-palladium systems,* J. Phys. Chem. **68** (1964) 1419–1426.

[25] H. Yokoyama, H. Namakura, and M. Koiwa, *The solubility and diffusion of carbon in palladium,* Acta Mater. **46** (1998) 2823–2830.

[26] L. Cheng, A. Böttger, T. H. de Keijser, and E. J. Mittemeijer, *Lattice parameters of iron-carbon and iron-nitrogen martensites and austenites*, Scr. Metall. Mater. **24** (1990) 509–514.

[27] D. York, *Least-square fitting of a straight line*, Canad. J. Phys. **44** (1966) 1079–1086.

[28] J. D. Eshelby, *The continuum theory of lattice defects*, Solid State Phys. **3** (1956) 79.

[29] G. V. Samsonov, N. N. Zhuravlev, Y. B. Paderno, O. I. Shulishova, and T. I. Serebryakova, *Interaction of gallium,indium, thallium,germanium,tin, and lead with boron*, Zh. Strukt. Khim. **1** (1960) 458–462.

[30] A. Wald and R. W. Stormont, *Investigations on the constitution of certain binary boron-metal systems*, J. Less-Common Met. **9** (1965) 426–433.

[31] T. B. Massalski, H. Okamoto, P. R. Subramanian, and L. Kacprzak, *Binary Alloy Phase Diagrams*, second edn., ASM International, Materials Information Soc., Materials Park, Ohio, 1990.

[32] *Mechanisch-thermische Zustandsgrößen*, in: *Eigenschaften der Materie in ihren Aggregatszuständen* (K. Schäfer and G. Beggerow, eds.), vol. II/1 of *Landolt-Börnstein*, sixth edn., Springer Verlag, Berlin, 1971.

[33] T. Hahn, *International Tables for Crystallography*, vol. A, fourth, revised edn., Kluwer Academic Publishers, Dordrecht, 1996.

[34] B. Lengeler, *EXAFS study of the structure of boron in palladium*, Solid State Commun. **55** (1985) 679–682.

[35] K. D. Allard, T. B. Flanagan, and E. Wicke, *The diffusion of hydrogen in boron-palladium alloys*, J. Phys. Chem. **74** (1970) 298–305.

[36] J. E. Worsham jr., M. K. Wilkinson, and C. G. Shull, *Neutron diffraction observations on the palladium-hydrogen and palladium-deuterium systems*, J. Phys. Chem. Solids **245** (1957) 303–310.

[37] H. L. M. Bakker, M. J. C. de Jong, P. M. Oppeneer, R. Griessen, A. Lodder, R. Vis, and H. Brodowsky, *Interstitial carbon in palladium: Fermi surface and electron scattering*, J. Phys. F **16** (1986) 707–720.

[38] E. Parthé, L. Gelato, B. Chabot, M. Penzo, K. Cenzual, and R. Gladyshevskii, *TYPIX, Standardized Data and Crystal Chemical Characterization of Inorganic Structure Types*, vol. 2, Springer-Verlag, Berlin, 1993.

[39] O. Kubaschewski, C. B. Alcock, and P. J. Spencer, *Material Thermochemistry*, 6th edn., Pergamon Press, Oxford, 1993.

[40] A. Westgren and A. Almin, *Über die Raumerfüllung der Atome in den Legierungen*, Z. Phys. Chem. B **5** (1929) 14–28.

[41] M. Ellner, *Zusammenhang zwischen strukturellen und thermodynamischen Eigenschaften bei Phasen der Cu-Familie in den T^{10}-B^1- und T^{10}-B^2-Systemen*, J. Less-Common Met. **75** (1980) P 5–P 16.

[42] M. Ellner, *Zusammenhang zwischen strukturellen und thermodynamischen Eigenschaften bei Phasen der Cu-Familie in den T^{10}-B^3-Systemen*, J. Less-Common Met. **60** (1978) P 15–P 39.

[43] M. Ellner, *Zusammenhang zwischen strukturellen und thermodynamischen Eigenschaften bei Phasen der Cu-Familie in den T^{10}-B^4-Systemen*, J. Less-Common Met. **78** (1981) P 21–P 32.

[44] N. F. Mott and H. Jones, *The Theory of the Properties of Metals and Alloys*, Oxford University Press, London, 1958.

[45] H. H. Stadelmaier, L. J. Hütter, and N. C. Kothari, *Über ternäre Karbide der T-Metalle Nickel, Kobald, Eisen und Mangan mit Gallium*, Z. Metallkd. **51** (1960) 41–45.

[46] J. D. Schöbel and H. H. Stadelmaier, *Zwei Boride mit Chromkarbid ($Cr_{23}C_6$) und Perowskitstruktur im Dreistoffsystem Nickel-Indium-Bor*, Z. Metallkd. **55** (1964) 378–382.

[47] P. Villars and L. D. Calvert, *Pearson's Handbook of Crystallographic Data for Intermerallic Phases*, vol. 1, second edn., ASM International, 1991.

[48] P. Villars, *Pearson's Handbook. Desk Edition, Crystallographic Data for Intermetallic Phases*, vol. 1, ASM International, Materials Park, 1997.

[49] E. Parthé, L. Gelato, B. Chabot, M. Penzo, K. Cenzual, and R. Gladyshevskii, *TYPIX, Standardized Data and Crystal Chemical Characterization of Inorganic Structure Types*, vol. 3, Springer-Verlag, Berlin, 1994.

[50] M. Beck, M. Ellner, and E. J. Mittemeijer, *The formation of interstital solid solutions based on solvents showing fcc structure; elastic versus chemical interaction*, Acta. Mater. **49** (2001) 985–993; (Chapter 1 of this dissertation).

[51] *Powder Diffraction File, Set 1-50 plus 70-88*, International Centre for Diffraction Data, Newton Square, PA, USA, 2000.

[52] K. Yvon, W. Jeitschko, and E. Parthé, *LAZY PULVERIX, a computer program, for calculating X - ray and neutron diffraction powder patterns*, J. Appl. Cryst. **10** (1977) 73–74.

[53] G. S. Smith and R. L. Snyder, *F_N: A criterion for rating powder diffraction patterns and evaluting the reliability of powder pattern indexing*, J Appl. Cryst. **12** (1979) 60–65.

[54] C. Wannek and B. Harbrecht, *$AlPd_3$ und $AlPd_5$: Neue Phasen im System Al-Pd*, Z. Kristallogr. Suppl. **15** (1998) 62.

[55] C. Wannek and B. Harbrecht, *Die Kristallstruktur von Ga_5Pd_{13} - eine niedersymmetrische Ordnungsvariante der kubischen dichtesten Kugelpackung*, Z. Anorg. Allg. Chem. **626** (2000) 1540–1544.

[56] H. Bärninghausen, *Group-subgroup relations between space groups: A useful tool in crystal chemistry*, Commun. Math. Chem. **9** (1980) 139–175.

[57] F. D. Manchester, A. San-Martin, and J. M. Pitre, *The H-Pd-system*, J. Phase Equilib. **15** (1994) 62–83.

[58] S. A. Semiletov, R. V. Baranova, Y. P. Khodyrev, and R. M. Imanov, *Elektronograficheskoje issledovanije tetragonalgo gidrida $PdH_{1.33}$*, Kristallografija **25** (1980) 1162–1168.

[59] B. Predel, *Metallic glasses*, in: *Thermochemistry of Alloys* (H. Brodowsky and H.-J. Schaller, eds.), vol. 286 of *NATO ASI Series C*, 451–469, Kluwer Academic Publishers Boston, 1989.

[60] G. Cocco, L. Schiffini, M. Sampoli, A. Lucci, and G. Riontino, *Compositional effects in Pd-B glassy alloys from X-ray determinated radial distribution functions*, Phys. Status Solidi A **76** (1983) 753–762.

[61] B. Predel and G. Duddek, *Über ein neues Verfahren zur Erzeugung metastabiler Festkörper durch extrem rasche Abkühlung flüssiger Legierungen*, Z. Metallkd. **69** (1978) 773–776.

[62] A. C. Larson and R. B. von Dreelen, *GSAS: General structure analysis system*, Tech. Rep. LA-UR-86-748, Los Alamos National Labratory (1994).

[63] P. M. de Wolff, *A simplified criterion for reliability of a powder pattern indexing*, J. Appl. Cryst. **1** (1968) 108–113.

[64] B. G. Hyde and S. Andersson, *Inorganic Crystal Structures*, J. Wiley & Sons, New York, 1989.

[65] P. Kripyakevich, *Strukturnyje Tipy Intermetallicheskikh Sojedinenij*, Izdatelstvo Nauka, Moscow, 1977.

[66] K. Schubert, *Kristallstrukturen zweikomponentiger Phasen*, Springer-Verlag, Berlin, 1964.

[67] S. R. Nagel and J. Tauc, *Nearly-free-electron approach to the theory of metallic glass alloys*, Phys. Rev. Letters **35** (1975) 380–383.

[68] U. Mizutani, *Electronic structure of metallic glasses*, Prog. Mater. Sci. **28** (1983) 98–228.

[69] H. Brodowsky and H.-J. Schaller, *Thermodynamics of nonstoichiometric interstitial alloys. 1. boron in palladium*, Trans. Metall. Soc. AIME **245** (1969) 1015.

[70] M. Beck, M. Ellner, and E. J. Mittemeijer, *The structure of the palladium-rich boride Pd_5B ($Pd_{16}B_3$)*, Z. Kristallogr. (2001) in press; (Chapter 2 of this dissertation).

[71] E. Wicke and H. Brodowsky, *Hydrogen in palladium and palladium alloys*, in: *Hydrogen in Metals* (G. Alefeld and J. Völkl, eds.), vol. 2, 73–156, Springer-Verlag, Berlin, 1978.

[72] R. Benz and P. L. Stone, *Thorium-carbon phase equilibria*, High Temp. Sci. **1** (1969) 114–127.

[73] H. Brodowsky and H.-J. Schaller, *Mischungseigenschaften des Systems Pd/B*, Ber. Bunsenges. **71** (1967) 926–927.

[74] H. Brodowsky, *Entmischungserscheinungen in Pd-Legierungen*, Ber. Bunsenges. **76** (1972) 360.

[75] J. Crank, *The Mathematics of Diffusion*, second edn., Clarendon Press, Oxford, 1990.

[76] B. E. Warren, *X-ray diffraction*, Addison-Wesley Publishing Company, Reading, 1969.

[77] W. H. Press, B. P. Flannery, S. A. Teukolsky, and W. T. Vetterling, *Numerical Recipes*, second edn., Cambridge University Press, Cambridge, 1994.

[78] *PROFIT for Windows User's Guide, Philips Analytical X-Ray*, first edn., Almelo, 1996.

[79] D. Hull and D. J. Bacon, *Introduction to Dislocation*, vol. 37 of *International Series on Materials Science and Technology*, third edn., Pergamon Press, Oxford, 1984.

[80] R. Delhez, T. H. de Keijser, and E. J. Mittemeijer, *Determination of crystallite size and lattice-distortions through X-ray-diffraction line-profile analysis - recipes, methods and comments*, Fresenius Z. anal. Chem. **312** (1982) 1–16.

[81] G. K. Williamson and R. E. Smallman, *Dislocation densities in some annealed and cold-worked metals from measurements on the X-ray Debye-Scherrer spectrum*, Phil. Mag. **1** (1956) 34–46.

[82] A. J. C. Wilson, *Mathematical Theory of X-Ray Powder Diffractometry*, Philips, Eindhoven, 1963.

[83] H. P. Klug and L. E. Alexander, *X-Ray Diffraction Procedure*, second edn., Wiley Interscience, New York, 1974.

[84] A. J. C. Wilson, *International Tables for Crystallography*, vol. C, Kluwer Academic Publishers, Dordrecht, 1995.

[85] C. Dong and J. I. Langford, *LAPODS: a computer program for refinement of lattice parameters using optimal regression*, J. Appl. Cryst. **33** (2000) 1177–1179.

[86] S. Popović, *An X-ray diffraction method for lattice parameter measurements from corresponding $K\alpha$ and $K\beta$ reflexions*, J. Appl. Cryst. **4** (1971) 240–241.

[87] S. Popović, *Unit-cell dimension measurements from pairs of X-ray diffraction lines*, J. Appl. Cryst. **6** (1973) 122–128.

[88] C. Dong, F. Wu, and H. Chen, *Correction of zero shift in powder diffraction patterns using the reflection-pair method*, J. Appl. Cryst. **32** (1999) 850–853.

[89] L. B. McCusker, R. B. Von Dreele, D. E. Cox, D. Louër, and P. Scardi, *Rietveld refinement guidlines*, J. Appl. Cryst. **32** (1999) 36–50.

[90] N. E. Brown, S. M. Swapp, C. L. Bennett, and A. Navrotsky, *High-temperature X-ray diffraction: solutions to uncertainties in temperature and sample position*, J. Appl. Cryst. **59** (1993) 77–84.

[91] W. Pitschke and A. Teresiak, *High temperature X-ray diffraction: Uncertainities in temperature measurement and intensity limitations*, Mater. Sci. Forum **278-281** (1998) 248–253.

[92] N. Eisenreich and W. Engel, *Difference thermal analysis of crystalline solids by the use of energy-dispersive X-ray diffraction*, J. Appl. Cryst. **16** (1983) 259–263.

[93] W. Fischer and P. Lersch, *Temperature distribution at the sample surface in high-temperature XRD using infrared thermography*, Mater. Sci. Forum **278-281** (1998) 254–259.

[94] Y. S. Touloukian, R. K. Kirby, R. E. Taylor, and P. D. Desai, *Thermal Expansion, Metallic Elements and Alloys*, vol. 12 of *Thermophysical properties of matter*, IFI/Plenum, New York, 1975.

[95] Y. S. Touloukian, R. K. Kirby, R. E. Taylor, and T. Y. R. Lee, *Thermal Expansion, Nonmetallic Solids*, vol. 13 of *Thermophysical properties of matter*, IFI/Plenum, New York, 1977.

[96] H. Hartmann, F. Ebert, and O. Breitschneider, *Elektrolyse in Phosphatschmelzen. 1. Die elektrolytische Gewinnung von* α *und* β *Wolfram*, Z. Anorg. Allg. Chem. **198** (1931) 116–140.

[97] W. Ostertag and G. R. Fischer, *Temperature measurements with metal ribbon high temperature X-ray furnaces*, Rev. Sci. Instr. **39** (1968) 888–889.

[98] A. Kern, *Hochtemperatur-Rietveldanalysen: Möglichkeiten und Grenzen*, vol. 89 of *Heidelberger Geowissenschaftliche Abhandlungen*, Dissertationsdruck, Heidelberg, 1998.

[99] M. Beck, M. Ellner, and E. J. Mittermeijer, *Powder diffraction data for borides Pd_3B and Pd_5B_2 and the formation of an amorphous borid Pd_2B*, Powder Diffr. **16** (2001) 98–101; (Chapter 3 of this dissertation).

Cirriculum Vitae

Markus Beck
born on 4th of July 1968 in Reutlingen

School

1975–1979	primary school, Reutlingen–Betzingen
1979–1988	secondary school, Reutlingen high school graduation (’Abitur’)

Higher education

10/89–6/96	Eberhardt-Karls-University Tübingen, Physics
7/96–7/97	Eberhardt-Karls-University Tübingen, diploma thesis: *Investigations of semi conductor laser systems with external cavity*
11/97–7/01	PhD at Max Planck Institute for Metals Research, Instiute for Materials Science, Stuttgart

Danke

Die vorliegende Arbeit wurde am Institut für Metallkunde der Universität Stuttgart und am Max-Planck-Institut für Metallforschung, Stuttgart, angefertigt.

Meinen besonderen Dank gilt Herrn Prof. Dr. Ir. E. J. Mittemeijer für die ausgezeichnete Betreuung und das große Interesse am Fortgang der Arbeit. Seine unermütliche Diskussionsbereitschaft trug wesentlich zum Erfolg der Arbeit bei.

Bei Herrn Prof. Dr. M. Rühle möchte ich mich für die Übernahme des Mitberichtes bedanken.

Bei Herrn Dr. M. Ellner bedanke ich mich für die intensive Betreuung und zahlreichen engagierten Diskussionen.

Für die hilfreiche Zusammenarbeit möchte ich mich bei allen Mitarbeitern des Max-Planck-Institutes für Metallforschung bedanken. Einen besonderen Dank möchte ich allen Doktoranden und Postdocs der Abteilung Mittemeijer für die sehr angenehme Atmosphäre aussprechen.

Schließlich möchte ich noch meinen Eltern für die Unterstützung danken.